INVESTIGATIONS OF CROSSED ANDREEV REFLECTION IN HYBRID SUPERCONDUCTOR–FERROMAGNET STRUCTURES

BY

MADALINA COLCI O'HARA

Dipl. de Lic., University of Bucharest, 2000
M.S., University of Illinois at Urbana-Champaign, 2003

DISSERTATION

Submitted in partial fulfillment of the requirements
for the degree of Doctor of Philosophy in Physics
in the Graduate College of the
University of Illinois at Urbana-Champaign, 2009

Urbana, Illinois

Doctoral Committee:

Professor James N. Eckstein, Chair
Professor Dale J. Van Harlingen, Director of Research
Professor Paul G. Kwiat
Professor Anthony J. Leggett

Abstract

Cooper pair splitting is predicted to occur in hybrid devices where a superconductor is coupled to two ferromagnetic wires placed at a distance less than the superconducting coherence length. In this thesis we search for signatures of this process, called crossed Andreev reflection (CAR), in three device geometries. The first devices studied are lateral spin valves. In these structures, when electrons with energies less than the superconducting energy gap are injected from one ferromagnetic wire into the superconductor, nonlocal transport processes involving the second ferromagnetic wire are predicted to take place. We measure a negative nonlocal voltage in the antiparallel magnetization alignment of the ferromagnetic wires, which is the theoretically predicted signature of CAR. The second type of hybrid devices that we measured consist of two superconducting electrodes connected by two ferromagnetic nanowires placed within a superconducting coherence length of each other, forming an S-FF-S junction. We find that below the critical temperature of the superconductor, the resistance versus temperature curves show re-entrant behavior, with the signal corresponding to antiparallel alignment of the magnetization of ferromagnetic wires distinctly larger than that of the parallel case. We discuss one possible explanation of this result in terms of Cooper pair splitting. We also report the first observation of multiple Andreev reflection peaks in the differential resistance of these devices. The third line of investigation briefly examines superconductor–ferromagnet SQUID-type devices to which we apply an external magnetic field to modulate the phase drop across the junctions. We do not observe coherent effects such as supercurrent or resistance oscillations, but suggest improvements for future research.

Pentru mama, cu dragoste, admiraţie şi recunoştinţă

Acknowledgments

I am indebted to my advisor, Dale Van Harlingen, and thank him for his continuous support and patience during my time as a PhD student. I enjoyed working on exciting research projects and it was a privilege to be exposed to his broad knowledge and impressive physical intuition. Dale's support in times of difficulty was crucial for finishing my work, and I am grateful for it. I also thank my thesis committee, Professors Tony Leggett, Paul Kwiat, and Jim Eckstein, for the time and effort put into my defense exam, for their careful reading of the manuscript, and for offering suggestions and making comments that improved the quality of my dissertation.

The successful completion of my PhD work is made possible by the contributions of many people along the way. To start with, Trevis Crane introduced me to the world of fabrication and, despite having this world take over my life, I thank him for his coaching. Lukas Urban trained me in the art of operating dilution fridges. He can always be counted on for solving problems, and together torturing the dilution fridge under the excuse of diagnosing malfunctions was educational and fun; it could have been productive too, were it not for all the chatting about unrelated matters that in the end did not lead to me cooking sauerkraut soup nor to him landing a job.

Special thanks go to Tony Banks who has been an amazing resource of fabrication knowledge. A great deal of my gratitude goes to him for keeping the Microfab show going; in particular, for fixing an instrument right away every time I needed it. Our conversations will be very much missed.

I am grateful to Martin Stehno for shared knowledge on our research projects, and for critical input on parts of my thesis. His skills in assembling cribs and dressers are very much appreciated as well. However, he will probably be remembered most for the delicious Mozart balls he always brought back from Austria. Gratitude is also due to Dan Bahr for cooling down the dilution fridge for me a few times when I was swamped with other tasks. It is a lot of fun being around him, especially when he takes a deep breath of helium gas or when the dialog-laced storytelling turns on. I extend my appreciation to all DVH group contemporary labmates for providing valuable insights into diverse problems, and for their help and support during the last year of my graduate work.

Most of my years in Urbana have involved a lot of work, but there has been some life outside the lab, on a few occasions. My first year was particularly fun owing to Micah, Josh, and Tim. I thank them for giving me a nice introduction to American life, and for their patience in repeatedly explaining menu items at restaurants. It was not their fault when in the end, after their frantic coaching, the question "How do you want your eggs?" left me dumbfounded. In addition to culinary help, Micah deserves thanks for his critical reading of a couple of manuscripts I wrote in the first year, after which they were notably improved. Also in the "Urbana" chapter, Francoise is a special mention: she always had an ear to listen to my frustrations and joys, and provided lots of fun conversations; I hope we stay in touch wherever we may be.

Some of my strongest friendships were separate from my life in Urbana. My closest friends, Bogdan and Ioana, have offered a great deal of support and understanding during my isolation years in graduate school. I thank them deeply. Many thanks also go out to Joy, my mother-in-law, who has helped me tremendously during the last 100 meters of my graduate school marathon by coming to Urbana to take care of Ethan.

I would not have come anywhere close to my achievement if it were not for my parents' sacrifices throughout my life, for which I am eternally grateful. Nu există cuvinte care să mulţumească îndeajuns parinţilor mei Ionel si Ioana pentru sacrificiile făcute ca să-mi ofere acces la educaţia pe care am avut-o. Iubirea, încurajările şi sfaturile lor au fost de nepreţuit de-a lungul anilor, iar recunoştinţa mea pentru tot ce au facut este eternă. Tata ar fi fost foarte mândru să mă vadă atât mămică cât şi doctor în fizică, dar din nefericire mama trebuie să ducă mândria pe umerii ei pentru amândoi. In plus faţă de părinţi, mulţumesc lui tanti Leana şi nenea Mircea pentru gândurile bune şi pentru felicitările trimise prin poştă an de an, cu ocazia fiecărei sărbători. De asemenea, sunt recunoscătoare lui tanti Anişoara şi întregii familii Rufa pentru rugăciunile lor şi susţinerea morală.

Finally, thanks to my husband, Tim, "Mr. Amazing, Mr. Incredibly-Superbly-Fantastic-Ness". His support and help for whatever I needed were crucial in completing my graduate work, while his efforts in making sure my eyes stayed focused on the end result have made this dissertation possible. He has touched many parts of this manuscript with his excellent proofreading skills and suggestions for concise writing. Overall, I am grateful to him for his patience and understanding throughout my graduate school journey.

I gratefully acknowledge the NSF DMR grant no. 06-05813 and the Department of Physics for various sources of funding over the years that enabled my scientific research to progress.

Table of Contents

List of Symbols

Δ	Superconducting energy gap
δ_s	Spin diffusion length in a normal metal
δ_s^f	Spin diffusion length in a ferromagnet
D	Electron diffusion constant in a normal metal
$D_{\uparrow,\downarrow}$	Spin-dependent diffusion constant in a ferromagnetic material
e	Electron charge
E_F	Fermi energy
E_{Th}	Thouless energy
E_k	Energy of quasiparticle excitations in a superconductor
E_{ek}	Energy of electron-like excitations in a superconductor
E_{hk}	Energy of hole-like excitations in a superconductor
H_c	Coercive field
$\hbar$	reduced Planck constant
I_S	Supercurrent in Josephson junctions
I_c	Critical current of a Josephson junction
k_F	Fermi wave vector
k_{B}	Boltzmann constant
λ_{Q^*}	Charge imbalance relaxation length in a superconductor
L_T	Thermal coherence length
L_φ	Electron phase coherence length
L_ϵ	Energy-dependent phase coherence length; $L_\epsilon = \min(L_{\mathrm{T}}, L_\varphi)$
M	Magnetization
μ	Chemical potential
N_S	Quasiparticle density of states of a superconductor
N_n	Normal metal density of states

$N_{\uparrow,\downarrow}$	Spin-dependent density of states of a ferromagnetic material
ξ_S	Superconducting coherence length
ξ_N	Normal metal coherence length
ξ_F	Ferromagnet exchange length
P	Spin polarization of electrical current
R_S	Spin resistance; Nonlocal resistance
σ	Normal metal conductivity
$\sigma_{\uparrow,\downarrow}$	Spin-dependent conductivity of a ferromagnetic material
T	Temperature
T_c	Superconducting critical temperature
T_{Curie}	Curie temperature of a ferromagnet
v_{F}	Fermi velocity

Chapter 1

Introduction

Creation and detection of entangled states had recently become a topic of intense study in solid state devices, both as a goal of fundamental research and for applications in quantum cryptography, quantum teleportation, and quantum computing. Any system with a two-level quantum degree of freedom is a candidate for entanglement, and the electron and its spin is the simplest such system.

Superconductors provide a natural source of entangled electron pairs through the Cooper pairs responsible for superconductivity. The two constituent electrons have entangled spin and orbital degrees of freedom. In the most common superconductors, the two electrons have opposite spins, and are bound in a singlet state.

The research proposed here is motivated by theoretical proposals [1; 2] according to which Cooper pairs can split into the constituent electrons and travel separately in a coherent fashion when a superconductor is coupled to two normal metal or ferromagnetic wires placed at a distance less than the superconducting coherence length from each other. In these structures, when electrons with energies less than the superconducting energy gap are injected from one wire into the superconductor, nonlocal transport processes involving the second wire are predicted to take place. One such process is the crossed Andreev reflection (CAR) by which an electron injected into the superconductor from one of the wires is reflected into the second wire as a hole with opposite spin. This hole propagating away from the interface with the superconductor can be seen as an electron going towards the interface. Therefore, CAR is equivalent to a process in which two electrons with opposite spins are injected in the superconductor, and a Cooper pair is condensed. Furthermore, CAR can be seen as a Cooper pair splitting into the two constituent electrons, which then propagate separately in the two wires as an entangled pair.

CAR is in competition with two other processes: local Andreev reflection at each interface, in which the hole is reflected into the same wire, and elastic co-tunneling (EC), in which the electron incident on the superconductor from one wire is transported without change of spin into the second wire.

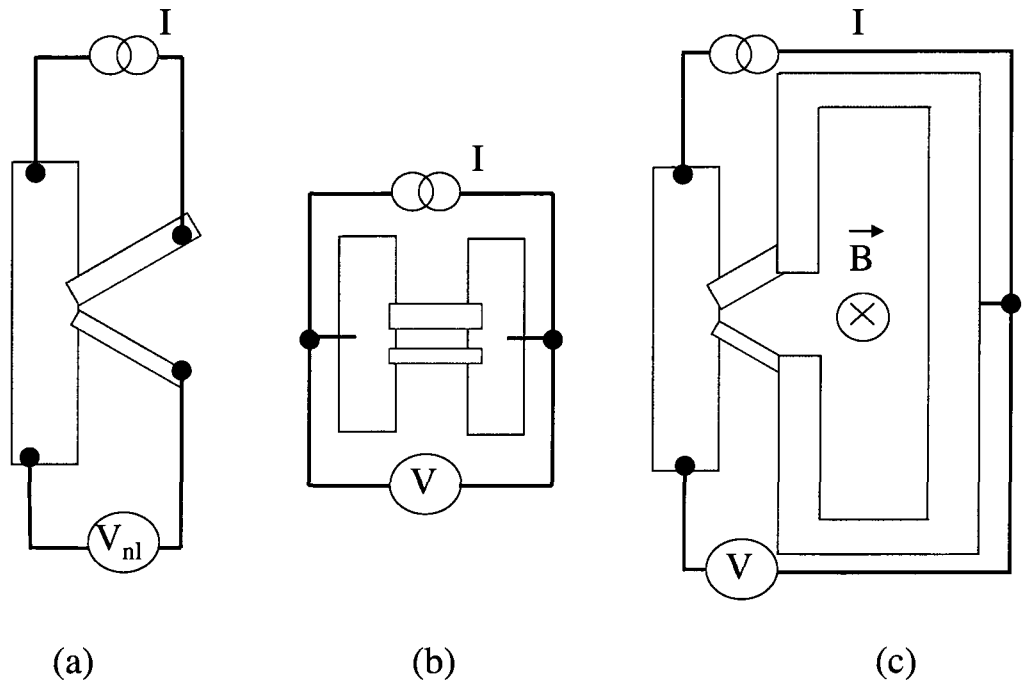

Figure 1.1 Design of samples fabricated to detect EC and CAR processes. (a) Nonlocal geometry. (b) Double junction geometry. (b) Loop geometry. The blue elements represent the superconducting part of the device, while the grey wires are the ferromagnets.

There have been several measurements of nonlocal transport in normal metal–superconductor–normal metal and ferromagnet–superconductor–ferromagnet structures [3–6] that claim evidence for crossed Andreev reflection and elastic co-tunneling. We planned to repeat and extend these measurements. In order to detect EC and CAR processes, we designed and measured samples in the following geometry configurations, schematically illustrated in Figure 1.1:

(a) Nonlocal geometry configuration, in which current is injected through one interface, and voltage is measured across the other interface. The measured voltage is "nonlocal" because there is no net charge current across the path where voltage is measured.

(b) Double junction geometry, in which the two junctions are at a distance less than the superconducting coherence length at both interfaces with the superconducting electrodes. The separation between the two superconducting electrodes is on the order of the electronic phase coherence length in the ferromagnet. In this limit, and for an antiparallel alignment of the magnetization of the two ferromagnetic probes, Josephson supercurrent is predicted to flow between the superconductors [7].

(c) Loop geometry, designed to look for phase coherent oscillations of supercurrent or resistance when a small magnetic field is applied perpendicular to the loop in order to establish a phase shift. We do not fully explore this geometry in this dissertation, but present preliminary results and directions for further investigation of this structure in Chapter 7.

Although an extensive study with both normal metal and ferromagnetic probes in all our geometry designs is desirable, we focus on using ferromagnetic probes on the superconductor because they provide the best way to distinguish EC and CAR effects. There have been several experiments done with normal metal probes in the nonlocal geometry [4–6], and our research plan did not include trying to reproduce them. However, the loop geometry in which the two probes are placed within a coherence length on the superconductor has not been investigated previously using normal metal probes; a study of this type of samples is relevant for both EC and CAR effects, and also for comparison to our results obtained in the same geometry but using ferromagnetic probes. Finally, in the double junction design we only use ferromagnetic probes; if normal metal junctions are employed, the low-temperature transport measurement would give a supercurrent flowing between the electrodes. This signal which cannot be interpreted in terms of EC and CAR contributions if there is no additional measurement. Therefore, our study does not include such junctions in this geometry configuration.

The dissertation is organized as follows. Chapter 2 introduces the concepts of superconductivity necessary to understand the discussion of various effects that we measure in our devices, followed by a fairly detailed presentation of spin injection and detection in normal metals.

Chapter 3 presents the basics of transport phenomena in superconducting hybrid structures, discussing first the case of normal metals in contact with superconductors, then extending the concepts to ferromagnetic structures, and ending with a review of theoretical models and experimental results of nonlocal Andreev reflection.

In Chapter 4 we describe the experimental techniques involved in producing the data reported in the next chapters. Here we illustrate sample fabrication procedures, and present our experimental setup with the various instruments used for taking data.

Chapter 5 starts with a brief overview of prior experimental work in ferromagnet–superconductor–ferromagnet mesoscopic spin valve devices, followed by a presentation and discussion of our experimental results in devices measured in the nonlocal configuration.

In Chapter 6, after reviewing theoretical models and prior experimental work relevant to the devices measured, we show transport measurements in superconductor–double ferromagnet–superconductor (S–FF–S) junctions. These are our most important results.

Chapter 7 briefly presents data from SFS and SNS SQUID-like devices where we looked for signatures of crossed Andreev reflection. Based on the results of our investigation, we suggest future directions for study. The dissertation ends with a summary of our findings.

Chapter 2

Theoretical Background

2.1 Superconductivity Concepts

In this section we outline fundamental concepts of superconductivity that are necessary to understand the mechanism of various effects and processes discussed in this dissertation.

The hallmark of superconducting materials is vanishing resistance at low temperatures. Electrical resistance in a material is due to scattering of electrons off of atoms in the material. When the temperature is lowered below a characteristic temperature called the superconducting critical temperature T_c, the conduction electrons in most metallic elements combine into Cooper pairs. The Cooper pairs are formed of two electrons that are brought together by an attractive effective interaction mediated by phonons. The physical picture is that an electron in a metal polarizes the medium and attracts positive ions; then, the presence of these ions attracts another electron. In this way the two electrons are bound together due to their attractive interaction with lattice ions.

For the majority of superconductors the bound pairs of electrons occupy states with equal and opposite momentum and spin, and have charge $2e$. Having zero net spin, a Cooper pair is a boson; thus, Cooper pairs can condense into a common ground state in a manner similar to that of particles in a Bose-Einstein condensate. This collective ground state is characterized by a single wavefunction, which describes the center-of-mass motion of all Cooper pairs. The collisions with the lattice that lead to ordinary resistivity would change the wavefunction of a Cooper pair. This would require all pairs to change as well, but because of the cooperative interaction between pairs, the pair momentum is not easily reduced. Therefore, the phase coherence of the pairs explains why superconducting materials exhibit zero resistivity.

One of the most remarkable characteristics of superconductors is the existence of an energy gap Δ between the condensed state and the excitations in the system. The superconducting gap represents the minimum energy required to create an excitation from the superconducting ground state. The energy gap is a function of temperature, as shown in figure 2.1(a). The ratio $\Delta(T)$ $\Delta(0)$

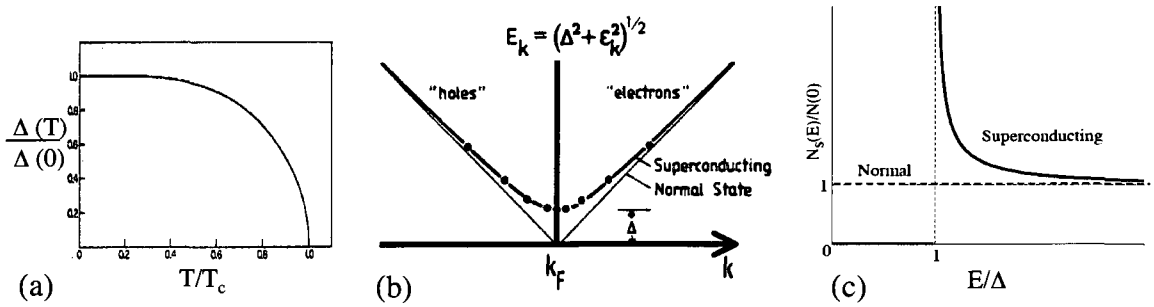

Figure 2.1 (a) Temperature dependence of the energy gap. Adapted from [8]. (b) Dispersion curve of excitation energy in normal and superconducting state. From [9]. (c) Density of states in a superconductor at energies above and below the superconducting gap. The horizontal dashed line represents the density of states of the normal metal. From [10].

decreases monotonically as T is increased, from a value of 1 at $T = 0$ to zero at T_c. While at low temperatures the dependence is slow ($\exp -\Delta/k_{\rm B}T$), near T_c the drop is approximated by $\Delta(T)/\Delta(T=0) \approx 1.74\sqrt{1-T/T_c}$. The value of the gap at zero temperature is $\Delta(0) = 1.764\ k_{\rm B}T_c$. From a physical point of view this is to be expected because only electrons within $k_{\rm B}T_c$ of the Fermi energy should determine a phenomenon that sets in at T_c.

The spatial extent of a Cooper pair is called the superconducting coherence length ξ_S. It can be estimated from the uncertainty principle, considering that the superconducting electrons have an energy range $\sim k_{\rm B}T_c$. Their momentum range is then $\Delta p = k_{\rm B}T_c/v_{\rm F}$ (where $v_{\rm F}$ is the Fermi velocity), and the uncertainty in their position gives $\Delta x \geq \hbar/\Delta p \approx \hbar v_{\rm F}/k_{\rm B}T_c$. The coherence length is then defined as $\xi_S = a\hbar v_{\rm F}/k_{\rm B}T_c$, where a is a numerical constant of order unity.

Breaking a Cooper pair results in two quasiparticle excitations, each with energies $E_k = \sqrt{\Delta^2 + \xi_k^2}$, where ξ_k is the one-electron energy of state k in the normal state, measured with respect to the Fermi energy. The quasiparticle excitation spectrum is illustrated in Figure 2.1(b). Conservation of number of electrons in the system requires that excitations are created or destroyed in pairs. The simplest excitation that satisfies this is represented by an electron and a hole with energies $E_{ek} = E_k + \mu$ and $E_{hk} = E_{k'} - \mu$, where μ is the chemical potential. Since $E_k \geq \Delta$, the excitation energy required to create a number-conserving excitation is given by:

$$(E_k + \mu) + (E_{k'} - \mu) = E_k + E_{k'} \geq 2\Delta\ . \tag{2.1}$$

Therefore, due to number conservation, the spectroscopic gap is 2Δ, not Δ. In order to find the density of states of quasiparticles in a superconductor, we equate the quasiparticle density of states to that of the normal metal: $N_S(E)\ E = N_n(\xi)\ \xi$. (This can be understood from the fact that the

quasiparticles are the "normal" electrons of the superconductor). Using $E^2 = \Delta^2 + \xi^2$, we obtain:

$$\frac{N_S(E)}{N(0)} = \begin{cases} \frac{E}{\sqrt{E^2-\Delta^2}} & , E > \Delta \\ 0 & , E < \Delta \end{cases} , \tag{2.2}$$

with $N(0)$ denoting the density of states in the normal metal at the Fermi level. This superconducting density of states is illustrated in Figure 2.1(c). We observe that no states are available for single electrons at energies below the gap, which is of great consequence when superconductors are brought in proximity to normal metals.

The best way to understand some of the effects in structures combining superconductors and regular metals is to use a physical picture based on a two fluid model. In this model the Cooper pairs form a superconducting fluid while the quasiparticles form a normal fluid. The total density of conduction electrons of the system is then given by the sum of the density of pairs n_p and that of quasiparticles n_q, i.e., $n = n_p + n_q$. The interaction between the two fluids occurs through the phonon "bath". Energy is constantly exchanged between these fluids, and pairs are broken into quasiparticles and, at the same time, quasiparticles combine into Cooper pairs with the processes having equal rates in thermal equilibrium.

2.2 Ferromagnetism and Spin-dependent Transport

Ferromagnetism: Spin Bands

Ferromagnetism manifests itself as a spontaneous magnetization in a material below a characteristic temperature T_{Curie}. Therefore, in a ferromagnetic material, there is a net magnetic moment even in the absence of an external magnetic field. By definition, the carriers with magnetic moment parallel to the magnetization are called spin-up, while the carriers with magnetic moment antiparallel to the magnetization are labelled spin-down.

Ferromagnetism is observed in transition metals (Co, Fe, and Ni) and their alloys (e.g., $Ni_{0.8}Fe_{0.2}$) in which the 3d shell is more than half filled. Due to Hund's rule for orbital filling of atomic shells, unfilled shells have an unequal number of electrons with spin up and with spin down, resulting in a net magnetic moment of the shell. The ordering of atomic moments that occurs in ferromagnets is a consequence of the exchange energy between the unpaired spins of neighboring atoms. This energy is the difference between the energy of the state of two parallel spins, and that of the state of two antiparallel spins.

Spin Polarized Current

In the field of the crystal lattice, electrons belong to bands of allowed energies instead of having quantized energy values. In a ferromagnetic metal there is an overlap in energy between the 3d band and the much wider 4s band. Since bands are filled only up to the Fermi level, each atom contributes to the conduction band electrons from both 4s and 3d bands.

The Stoner model of ferromagnetism further expands the band concept to include spin sub-bands for the d-electrons. Figure 2.2 illustrates a simplified view of the band structure of a normal metal (a), and a ferromagnet (b). The spin sub-bands are equal in the normal metal, while in the ferromagnet the Fermi surface intersects the spin sub-bands unequally; we label the spin-dependent density of states (DOS) with $N_\uparrow$ and $N_\downarrow$, corresponding to spin-up and spin-down conduction electrons, respectively. Also, we note in Figure 2.2(b) that the spin-up and spin-down DOS are shifted relative to each other by the exchange energy in a ferromagnet.

The different DOS in the ferromagnet result in different conductivities for the spin-up and spin-down electrons, given by the Einstein relation:

$$\sigma_{\uparrow,\downarrow} = e^2 N_{\uparrow,\downarrow}(E_F) D_{\uparrow,\downarrow} \quad , \tag{2.3}$$

where e is the electron charge, and $D_{\uparrow,\downarrow}$ is the spin-dependent diffusion constant.

Therefore, in a ferromagnet the electric current is carried unequally by spin-up and spin-down electrons. Mott [11] was the first to express the current in ferromagnetic metals as the sum of two parts, consisting of contributions from electrons with two spin projections. The net spin polarization P of the electrical current leaving a ferromagnetic material is defined as:

$$P = \frac{\uparrow - \downarrow}{\uparrow + \downarrow} = \frac{\sigma_\uparrow - \sigma_\downarrow}{\sigma_\uparrow + \sigma_\downarrow} \tag{2.4}$$

where $\uparrow$, $\downarrow$ are the spin sub-band partial currents.

2.2.1 Spin Polarized Transport into a Nonmagnetic Metal

In this section we explain how spins can be injected from a ferromagnet into a nonmagnetic metal. We then examine the behavior of the injected spins inside the normal metal. Last, we show how this spin population can be detected. We follow the analysis presented in [12].

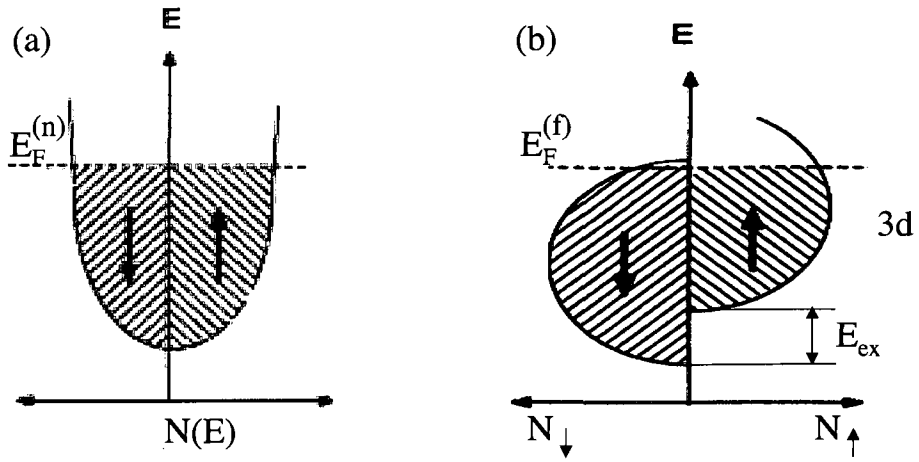

Figure 2.2 (a) The free-electron density of states of a normal metal. The filling of the spin sub-bands is symmetric, and the spin DOS are equal. (b) Simplified 3d-band structure of a ferromagnet. The up-spin band and down-spin band are shifted in energy by the exchange energy E_{ex}. The filing of the spin sub-bands is unequal at the Fermi energy. Adapted from [12].

Spin Injection and Accumulation

The spin injection process refers to the penetration of spin-polarized current from a ferromagnet (F) into a nonmagnetic material (N). The possibility of injecting spin was first shown theoretically by Aronov [13]. He suggested that this would lead to a nonequilibrium magnetization in the normal metal near the F/N interface. This prediction was then tested in the first spin injection experiment, realized by Johnson and Silsbee [14], illustrated schematically in Figure 2.3(a).

The device employed by Johnson and Silsbee consists of two ferromagnetic strips F1 and F2 separated by a nonmagnetic region. The electric current I_e injected in F1 has random spin orientation; when it leaves the ferromagnet at the other end, it will have a net polarization along the axis of magnetization. This spin-polarized current will carry magnetization across the F1/N interface. We can define a current of magnetization

$$I_M = P_1 \, \mu_B I_e/e \ , \tag{2.5}$$

where P_1 is the fractional polarization of current crossing the F1/N interface, μ_B is the Bohr magneton, and I_e/e is the number current of electrons in the bias current.

Figure 2.3(b) illustrates the density of states of F1 and N when no current is injected in the F/N structure; the Fermi levels of the two metals align: $E_F^{(f)} = E_F^{(n)}$. The microscopic transport when current is injected from F1 into N is illustrated in Figure 2.3(c). Now electrons can flow between the spin-up sub-bands of F1 and N, raising the chemical potential of the spin-up sub-band of the normal

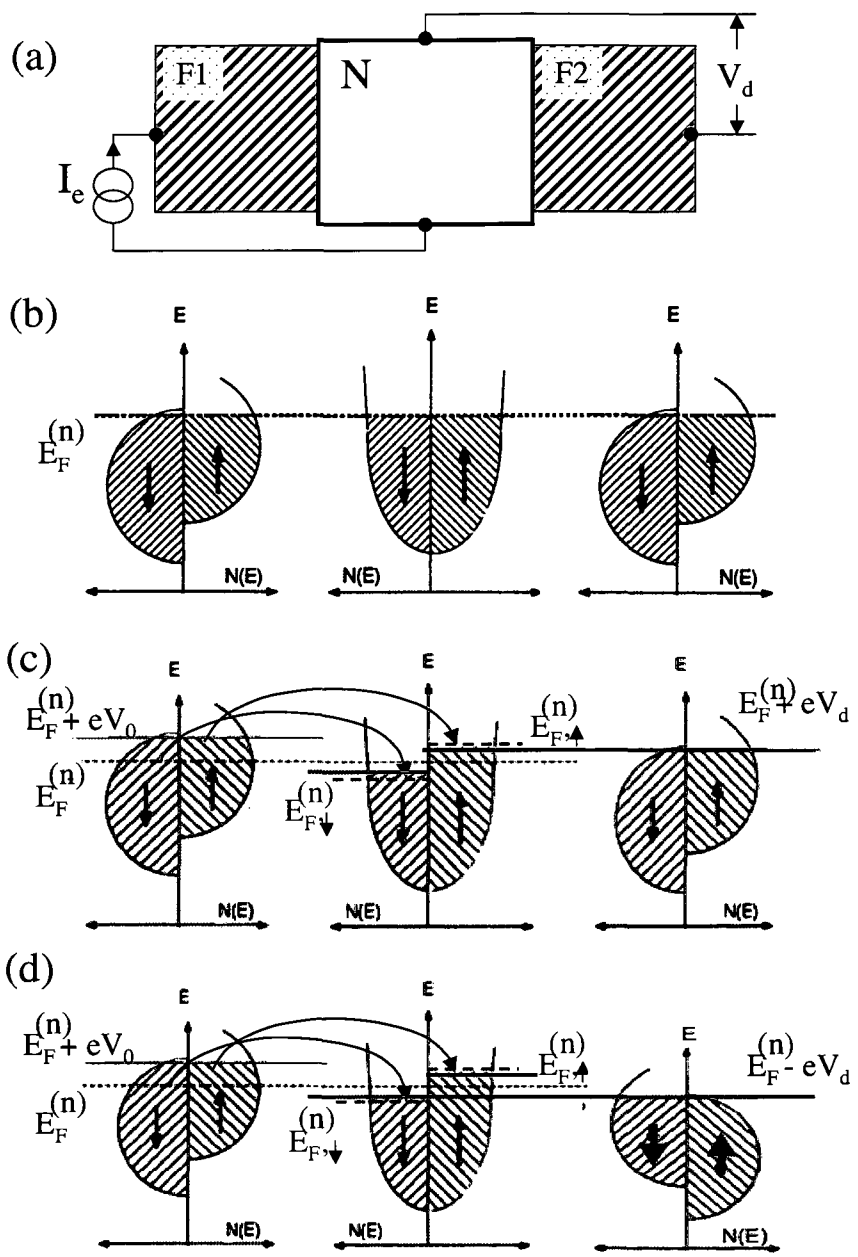

Figure 2.3 (a) Schematic representation of the first spin injection experiment by Johnson and Silsbee. F1 is the spin-injector probe, and F2 is the spin-detector probe. (b) The equilibrium density of states of the ferromagnetic probes and of the normal metal. (c) Density of states of the metals in structure in (a) when a voltage $_0$ is applied across the left interface to drive current into N. The relative magnetization orientation of F1 and F2 is parallel. Current flows between the up (down) spin sub-band of the ferromagnet and the up (down) spin sub-band of the normal metal; an equivalent charge is lost from the down (up) sub-band to fulfill charge neutrality requirements. The Fermi surface of the detector ferromagnet aligns with the nonequilibrium spin imbalance in N. (d) The relative magnetization orientation of F1 and F2 is antiparallel. Adapted from [12].

metal (the dotted blue line above $E_{F,\uparrow}^{(n)}$); charge neutrality in N requires that an equivalent number of spin-down electrons be lost from the spin-down sub-band, which results in a lower chemical potential for this sub-band compared to equilibrium (the blue dotted line below $E_{F,\downarrow}^{(n)}$). Current also flows from the spin-down sub-band of F1 to the spin-down sub-band of N, resulting in the spin-down sub-band chemical potential $E_{F,\downarrow}^{(n)}$ (green line). The equivalent loss from the spin-up sub-band required to maintain charge neutrality results in the spin-up sub-band chemical potential $E_{F,\uparrow}^{(n)}$ (red line.)

The magnetization carried across the F1/N interface causes a different occupation of the normal metal sub-bands, with the resulting electrochemical potential in each sub-band equal to [12]:

$$E_{F,\uparrow}^{(n)} = E_F^{(n)} + \mu_B \frac{\delta M}{\chi}; \quad E_{F,\downarrow}^{(n)} = E_F^{(n)} - \mu_B \frac{\delta M}{\chi} \quad , \tag{2.6}$$

where χ is the magnetic susceptibility of the normal metal, and δM is the nonequilibrium magnetization. The difference between these two chemical potential values represents the nonequilibrium magnetization δM that appears in N. This nonequilibrium magnetization is the result of the interplay between the rate of magnetization injection by current I_M, and rate of relaxation $1/T_2$ due to spin relaxation processes, where T_2 is the relaxation time; spin accumulation occurs when the injection rate is higher than the spin relaxation rate. The nonequilibrium magnetization can be expressed as:

$$\delta M = \frac{I_M T_2}{L} \quad , \tag{2.7}$$

where is the cross-sectional area of the normal metal, and L is the volume that the spins occupy in N. When this volume is diminished, δM will be larger for a constant number of nonequilibrium spins.

Spin Transport: Diffusion and Relaxation

The injected nonequilibrium spins diffuse away from the interface, and relax due to collisions in time T_2, the spin relaxation time. The average distance travelled in the normal metal before the spin is randomized is called the spin diffusion length, $\delta_s = \sqrt{DT_2}$, where D is the electron diffusion constant.

The injected spins can also diffuse backwards into F1, creating a nonequilibrium spin population on the F side of the interface with a spatial extent determined by δ_s^f, the spin diffusion length in the ferromagnet.

The nonequilibrium spin population accumulated at the interface acts as a spin bottleneck for further spin transport across the interface. The flow of charge between F1 and N is also obstructed, since spin and charge belong to the same carrier. Therefore, the resistance of the interface increases. This extra resistance is called the spin-coupled resistance, and is denoted by R_S.

Another way to understand this interfacial resistance is by analyzing the changes in the chemical potential in the two metals: the rise in the chemical potential of the spin-up sub-band of the normal metal has a back effect on the injector, causing its chemical potential to rise also and align with $E_{F,\uparrow}^{(n)}$. If this did not happen, there would be a back-flow of electrons from N into F1. Johnson and Silsbee [15] show that there is a thermodynamic force associated with δM which acts to drive spins back into F1. This force also acts as an electrical impedance, which gives rise to the extra interfacial spin resistance R_S.

Spin relaxation refers to changing the spin orientation from the initial direction. To do this, a magnetic torque is required. One mechanism that can provide this is a weakly relativistic spin-orbit interaction between the spin and the the electric field of the ions in the metal; this mechanism was described separately by Elliott [16] and Yafet [17]. Typical spin relaxation times in metals are on the order of 10 ps.

Spin Detection

Silsbee [18] proposed that spin accumulation can be detected by using a second ferromagnetic probe F2 in contact to the normal metal, placed within a spin diffusion length from the injector (see Figure 2.3(a)). This detector acts as a spin analyzer: the detected signal is proportional to the projection of nonequilibrium magnetization in N onto the magnetization of F2. If a low impedance ammeter connects N and F2 in the external circuit, current will flow through the interface:

$$J_e = \frac{1}{e}[g_\uparrow(E_{F,\uparrow}^{(n)} - E_F^{(f)}) + g_\downarrow(E_{F,\downarrow}^{(n)} - E_F^{(f)})] \quad , \tag{2.8}$$

where $g_\uparrow$, $g_\downarrow$ are interfacial spin conductances per unit area for current from sub-band $\uparrow$ or $\downarrow$. Equation 2.8 shows two currents flowing between N and F2: one current is forward (N to F2) between the spin-up sub-bands, and the other is backward (F2 to N) between the spin-down sub-bands. Using Equations 2.6 we can re-write the current in the form:

$$J_e = \frac{1}{e}[(E_F^{(n)} - E_F^{(f)})(g_\uparrow + g_\downarrow) + \mu_B \frac{\delta M}{\chi}(g_\uparrow - g_\downarrow)] \quad . \tag{2.9}$$

If the external circuit connecting N and F2 has high impedance (for example, if a voltmeter is connected in the circuit), current will not flow across the interface: $J_e = 0$. Equation 2.9 then reduces to:

$$-\frac{1}{e}(E_F^{(n)} - E_F^{(f)}) = \mu_B \frac{\delta M}{e\,\chi} \frac{g_\uparrow - g_\downarrow}{g_\uparrow + g_\downarrow} \quad . \tag{2.10}$$

The left-hand side of Equation 2.10 is a voltage term: the nonequilibrium magnetization in N results in a voltage V_d across the interface with detector F2:

$$V_d = \mu_B \frac{\delta M}{e\,\chi} \frac{g_\uparrow - g_\downarrow}{g_\uparrow + g_\downarrow} = P_2 \mu_B \frac{\delta M}{e\,\chi} \quad . \tag{2.11}$$

Combining equations 2.5 and 2.7 for I_M and δM, and using a free-electron expression for the normal metal susceptibility $\chi = \mu_B^2 N(E_F)$, with $N(E_F)$ given by equation 2.3, we can rewrite the above expression as:

$$V_d = P_1 P_2 \frac{\delta_s^2}{2AL} I_e \quad . \tag{2.12}$$

In the above equations P_1 and P_2 represent the fractional polarization of the carriers across interface F1/N and F2/N, and and A are the resistivity and cross-sectional area of the normal metal wire.

We refer again to the DOS picture describing magnetization transport across interfaces to examine the changes in the detector's DOS. Figure 2.3(c) considers the case when the magnetization orientations of injector and detector are parallel. When bias current is injected from F1 into N, the nonequilibrium spin population created in N shifts the spin sub-bands of the normal metal. When a high impedance voltmeter in the external circuit connects N and F2, the chemical potential of F2 rises to align with $E_{F,\uparrow}^{(n)}$ to prevent current flow; this change eV_d gives the measured voltage derived above. If the relative orientation of F1 and F2 is antiparallel (see Figure 2.3(d)), the chemical potential of F2 lowers to align with $E_{F,\downarrow}^{(n)}$; the voltage measured is $-V_d$. Since the nonequilibrium magnetization δM is proportional to $E_{F,\uparrow}^{(n)} - E_{F,\downarrow}^{(n)}$, it can be measured experimentally by changing the relative alignment of the magnetization of F1 and F2 between parallel and antiparallel.

Spin Injection and Detection in Mesoscopic Lateral Spin Valves

The first spin injection experiment described in this chapter introduced a "nonlocal" measurement configuration: the injected current did not flow through the path across which voltage is measured. If

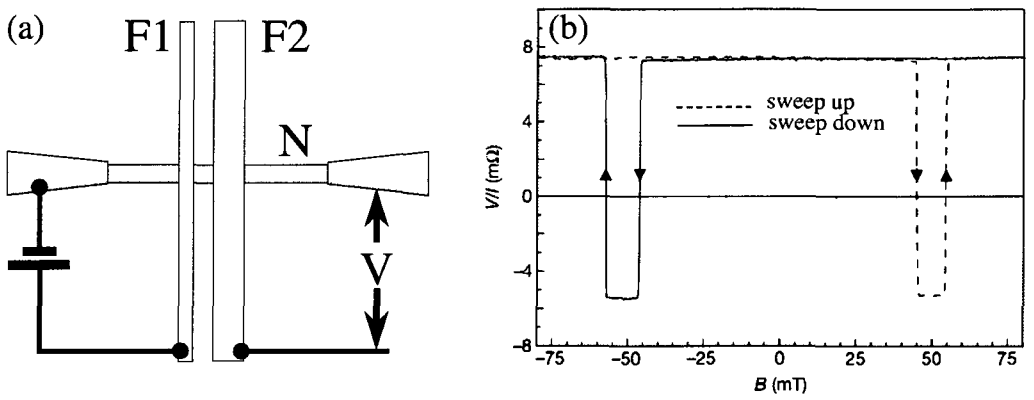

Figure 2.4 (a) Typical lateral spin valve structure. The measurement configuration is the nonlocal voltage detection. (b) Nonlocal resistance versus magnetic field curve, showing characteristic switching when the magnetization of F1 and F2F1/N became parallel or antiparallel. Adapted from [19].

we express the spin-related interfacial resistance R_S defined earlier as V_d/I_e, then spin accumulation can be detected as a resistance change of $2R_S$ when the magnetization of the two ferromagnets changes from parallel to antiparallel alignment. This spin resistance R_S is now a nonlocal resistance. The nonlocal measurement has been used extensively in the last decade to study spin accumulation in mesoscopic lateral spin valves. A schematic drawing of such a device is shown in Figure 2.4(a). The main difference between this type of device and that used in the first spin injection experiment is the width and thickness of the normal metal, which are much smaller in mesoscopic devices. The ferromagnetic wire F1 is used to inject spin-polarized current in the normal metal N. The other ferromagnetic wire F2 detects the voltage due to spin accumulation a distance L away from the injection point. The two ferromagnets are made of different widths in order to have different coercivities $H_{c1} \neq H_{c2}$. Therefore, an external magnetic field applied along the wires switches the magnetization orientation of each wire independently. Figure 2.4(b) shows changes in the nonlocal resistance as a function of the applied field. When the magnetic field reaches the value H_{c1}, the magnetization of the wider wire flips. F1 and F2 now have antiparallel magnetization orientation. At the field value corresponding to H_{c2}, the other wire flips its magnetization, and the relative magnetization orientation is again parallel. Using equation 2.12 and the definition of R_S, we obtain expressions for the nonlocal resistance.

For a separation between detector and injector smaller than the spin diffusion length $L \ll \delta_s$, the nonlocal resistance is:

$$R_S = \pm P_1 P_2 \frac{\delta_s}{2A} \ . \tag{2.13}$$

For $L > \delta_s$, the nonlocal resistance decays exponentially as a function of L:

$$R_S = \pm P_1 P_2 \frac{\delta_s}{2A} e^{-L/\delta_s} \ . \tag{2.14}$$

In the above equations, the + and − signs correspond to parallel and antiparallel magnetization alignment of the probes. The resistance difference between parallel and antiparallel alignments gives the spin accumulation: $\Delta R = 2R_S$.

2.2.2 Magnetoresistance

Even though ferromagnetic materials are spontaneously magnetized at room temperature, they are not saturated. This is due to the fact that the material is divided into many small domains. Each domain is spontaneously magnetized to saturation, but the direction of magnetization varies from domain to domain, so the net magnetization $\vec{M}$ is almost zero.

When an external magnetic field is applied, the domains of magnetization oriented close to the direction of the field will increase in size at the expense of those whose moment lies antiparallel to the field. There is now a net magnetization $M = M_S \cos\theta$, where θ is the angle between $\vec{M}$ and the field direction, and M_S is the saturation magnetization. At high enough field, $\vec{M}$ has rotated completely, and it is parallel to the field; the ferromagnet is saturated with a magnetization M_S.

Ideally, at saturation, the magnetization of a ferromagnetic structure is oriented along a uniaxial anisotropy axis. Figure 2.5(a) illustrates the magnetization reversal process. The wire axis is along x, and the magnetization vector points in the -$\hat{x}$ direction at zero external field. Two magnetization states are then defined, positive and negative, according to the orientation of the magnetization vector relative to this axis. If the external magnetic field $\vec{B}$ is applied parallel to the anisotropy axis, the state with magnetization oriented in the same direction as $\vec{B}$ is referred to as the "parallel" or "up" state. When $\vec{M}$ points in the opposite direction to $\vec{B}$, the state is called "antiparallel" or "down".

Figure 2.5(b) shows the resistance change of a ferromagnetic material as the magnetic field is increased from zero in both the positive and negative direction. The curves are for two different orientations between the magnetic field direction and the wire axis: $\theta = 10°$ and $\theta = 80°$. Each curve has two parts: a reversible magnetization rotation part proportional to $\cos\theta$, and an irreversible

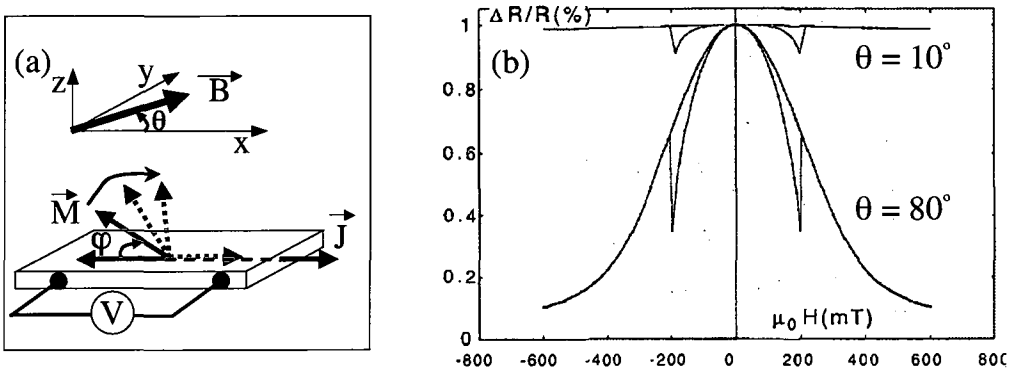

Figure 2.5 (a) Schematic view of magnetization rotation and reversal in a ferromagnetic wire as the magnetic field is increased. The wire axis is along $\hat{x}$, and the current flows along this axis. At the beginning, the magnetization is aligned along the wire and points in the -$\hat{x}$ direction. (b) AMR hysteresis loops calculated using the Stoner-Wohlfarth model. The external field is oriented at $\theta = 10°$ and $\theta = 80°$ with respect to the wire axis. From [20].

jump, which occurs at the external field value called the switching field, or the coercive field.

The mean magnetic field inside a ferromagnetic material is $4\pi M_S$; for typical ferromagnets this is approximately 1–2 T. However, the external field required to switch the magnetization along the wire is somewhat smaller than this, on the order of a few hundred mT.

2.2.3 Anisotropic Magnetoresistance

The dependence of magnetic properties on a preferred direction in space is referred to as magnetic anisotropy. In 1857 Thomson (Lord Kelvin) found that the electrical resistivity of a ferromagnet changes with the relative direction of the charge current with respect to the magnetization direction. It took almost a century for this discovery to be explored further, both theoretically and experimentally. This effect is now known as anisotropic magnetoresistance (AMR), and is due to differences in electron scattering when the electric current through a ferromagnetic material flows at an angle with respect to magnetization orientation.

The electric field inside a magnetized material can be written in terms of three contributions to the resistivity:

$$\vec{E} = \rho_\perp \vec{J} + (\rho_{||} + \rho_\perp)(\hat{\alpha} \cdot \vec{J})\hat{\alpha} + \rho_H \hat{\alpha} \times \vec{J} \ , \tag{2.15}$$

where $\vec{J}$ is the current vector, $\hat{\alpha}$ is the unit vector in the magnetization direction, $\rho_\perp$ and $\rho_{||}$ are the resistivity components for $\vec{J}$ perpendicular and parallel to $\vec{M}$, respectively, when there is no external

field applied, and ρ_H is the Hall effect resistivity. Using the general form for resistivity $\rho = \vec{E} \cdot \vec{J}/J^2$ and the above equation, we obtain the following expression for the AMR resistivity:

$$\rho_{\mathrm{AMR}} = \rho_{\perp} + \Delta\rho \cos^2 \quad , \tag{2.16}$$

where $\Delta\rho \equiv \rho_{\parallel} - \rho_{\perp}$, and is the angle between $\vec{M}$ and the electric current $\vec{J}$ oriented along the wire axis, as shown in Figure 2.5(a). Since the external applied field is also usually oriented along this axis, the AMR curve can be linked to the rotation of magnetization. We then have $M = M_s \cos$, and $R = R_0 + \Delta R_{\mathrm{max}} \cos^2$, where R_0 is the resistance in zero field, and ΔR_{max} is the difference in resistance between the saturation value and R_0.

Chapter 3

Transport Phenomena in Superconducting Hybrid Structures

In this chapter we review background information on hybrid structures containing at least one superconducting part. In the first section we will give a relatively detailed description of the superconductor–normal metal structures, and then, in the second section, we will extend the concepts to the case when the normal metal is ferromagnetic. In the last section we discuss nonlocal Andreev reflection processes in both normal metal and ferromagnetic devices.

3.1 Superconductor-Normal Metal Heterostructures

In this section we examine superconductor–normal metal hybrids, and review the Blonder-Tinkham-Klapwijk (BTK) model [21] formulated for electron transport in these structures. We describe the characteristics of the Andreev reflection process and its relation to the proximity effect, and describe the re-entrance effect. Lastly, we discuss Josephson effect and multiple Andreev reflections in structures made of a normal metal wire sandwiched between two superconductors, forming an SNS junction.

3.1.1 Non-Equilibrium Superconductivity: Charge Imbalance

Consider an NIS junction: a normal metal N in tunnel contact with a superconductor S. When a voltage V larger than the superconducting gap $V \gg \Delta/e$ is applied between the normal metal and the superconductor, quasiparticles of electron-like or hole-like character are injected into the superconductor. An electron incident from N into S has different probabilities of entering the electron-like branch and the hole-like branch of the quasiparticle spectrum of the superconductor (see Figure 3.1). This results in a charge imbalance between the electron-like and hole-like branches.

If we define $n_>$ and $n_<$ as the number of quasiparticles per unit volume in the electron-like and hole-like branches, respectively, then this imbalance is characterized by the net quasiparticle charge density $Q^* = n_> - n_<$. Electrical neutrality requires a compensatory change in the number

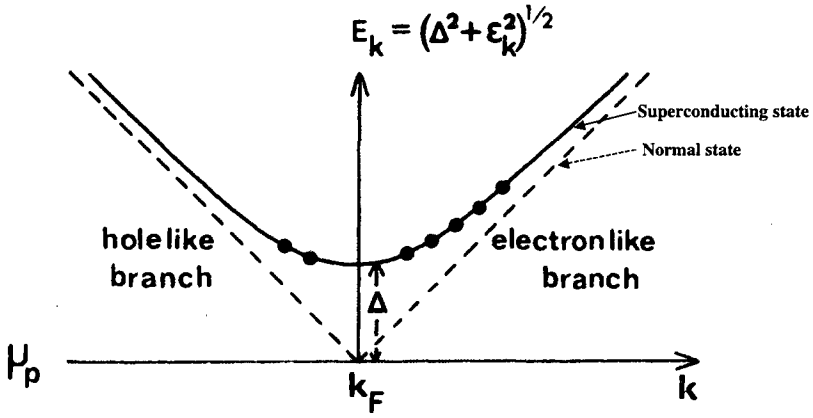

Figure 3.1 Quasiparticle spectrum with schematic indication of electronlike and holelike population imbalance. Reproduced from [22].

of electrons in the BCS ground state, which is produced by a shift in the chemical potential of the pairs. Therefore, the electrochemical potential μ_n of the quasiparticles and that of the superconducting pairs μ_p shift in opposite directions from their common equilibrium values. This results in a measurable difference in the electric potential in the same metal.

Tinkham and Clarke [22] showed that the measured voltage is given by

$$V = \frac{Q^*}{2eN(0)g_{\mathrm{NS}}} \quad , \tag{3.1}$$

where $N(0)$ is the density of states in the normal metal at the Fermi level, and $g_{\mathrm{NS}} = G_{\mathrm{NS}}/G_{\mathrm{NN}}$ is the normalized tunnel conductance of the junction. Therefore, by measuring V, one can determine Q^*.

When current injection in the superconductor stops, the time it takes the superconductor to reach equilibrium is given by the charge imbalance time:

$$\tau_{Q^*} = \frac{4}{\pi}\tau_E \frac{k_{\mathrm{B}}T_c}{\Delta} \quad , \tag{3.2}$$

where τ_E is the energy relaxation time for an electron at the Fermi surface. This sets the time for the perturbations on the quasiparticle branch to relax to zero by inelastic scattering. This time τ_{Q^*} diverges as $1/\sqrt{1-T/T_c}$ near T_c because in this temperature region only a fraction $\Delta/k_{\mathrm{B}}T_c$ of the thermally occupied states just above the gap can relax the charge imbalance, and $\Delta \to 0$ as $T \to T_c$, as discussed in Chapter 2.

When the area of quasiparticle injection is large, diffusion does not play an important role, and

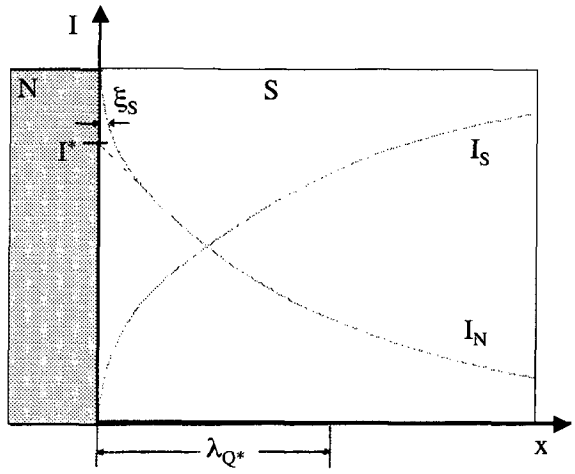

Figure 3.2 Schematic representation of the conversion of normal current into supercurrent at an N/S interface. I^* is the quasiparticle current associated with creation of charge imbalance, which decays over the charge imbalance relaxation length λ_{Q^*}. The Andreev current is carried for a distance of $\sim \xi_S$ as a quasiparticle current before decaying into a pair current. Reproduced from Blonder et al. [21].

the steady-state charge imbalance is determined by the competition between injection rate $dQ_{\rm inj}/d$ and relaxation rate Q^*/τ_{Q^*}. However, if charge imbalance occurs in a one-dimensional diffusive system characterized by diffusion constant D, then Q^* decays exponentially as $\exp(-x/\lambda_{Q^*})$, where

$$\lambda_{Q^*} = \sqrt{D\tau_{Q^*}} = \sqrt{\frac{v_F l}{3}\tau_{Q^*}} \tag{3.3}$$

is the charge imbalance relaxation length in the superconductor.

Electrons from the normal metal incident on the superconductor at energies $E \gg \Delta$ pass through the interface depositing all of their charge as Q^*, for both the case of a tunnel barrier between N and S, or when there is no barrier. A very different effect occurs if the incident electrons come in at sub-gap energies $E < \Delta$. In this case, they cannot enter the superconductor as quasiparticles because there are no quasiparticle states in the gap. The transfer in this case occurs via a two-step process, illustrated in Figure 3.2: First, the electrons enter as evanescent waves in the gap which decay into the condensate over a distance comparable to ξ_S, and smaller than λ_{Q^*}. After this, the transfer occurs via Andreev reflection: the incident electrons are reflected back into the normal metal as holes, and a charge $2e$ is transferred in the pair condensate. Thus, even for $eV < \Delta$, a quasiparticle current penetrates the superconductor a depth $\xi_S(T)$ before the current is converted into supercurrent carried by Cooper pairs.

3.1.2 The Blonder-Tinkham-Klapwijk Model

Blonder, Tinkham, and Klapwijk (BTK) modeled one dimensional transport through a normal metal–superconductor interface for the case of arbitrary barrier strength . In this model there are

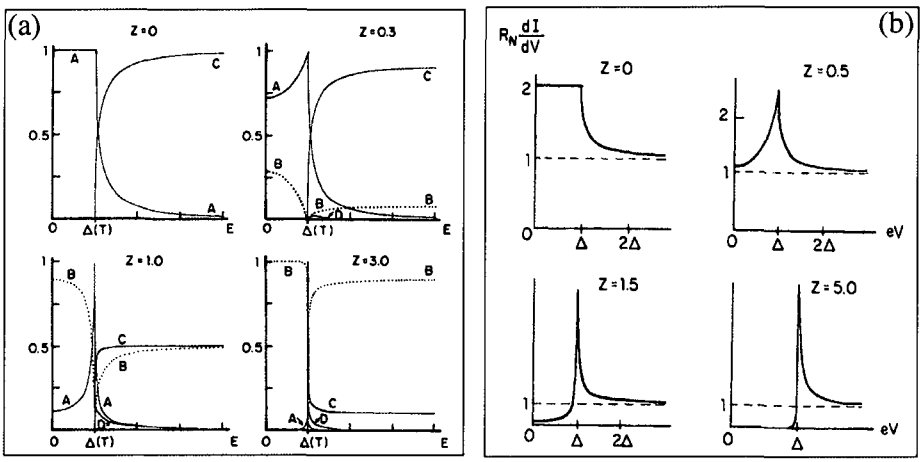

Figure 3.3 (a) Transmission and reflection coefficients at the N/S interface as a function of the incident electron energy E. Each plot is for a different barrier strength, characterized by Z. (b) Calculated differential resistance curves vs. the bias voltage at zero temperature for various barrier strengths Z. From Blonder et al. [21].

four possible transport processes of an electron incident on the N/S interface from the normal metal side: transmission through the interface with a wave vector on the same side of the Fermi surface ($q^+ \rightarrow k^+$), with probability $C(\epsilon)$; transmission with crossing through the Fermi surface ($q^+ \rightarrow -k^-$), with probability $D(\epsilon)$; ordinary reflection, with probability $B(\epsilon)$; and Andreev reflection as a hole on the other side of the Fermi surface, with probability $A(\epsilon)$.

The BTK model introduces a dimensionless parameter Z to characterize the barrier strength, in terms of which the transmission coefficient is $1/(1+Z^2)$, and the reflection coefficient is $Z^2/(1+Z^2)$. The probabilities of the processes A, B, C, and D are plotted in Figure 3.3(a) as a function of the incident electron energy E for values of Z ranging from zero (metallic interface) to 3 (tunnel barrier). For high transparent interfaces, and for energies lower than the superconducting gap, all current is transmitted into the superconductor via Andreev reflection. If the energy is increased above the gap, the probability for transmission as a quasiparticle starts increasing. If the barrier is raised to $Z = 0.3$, we see that a fraction of the incident electrons will undergo normal reflection. The higher the barrier, the more incident electrons are reflected. In the tunnel barrier case, all incident electrons are reflected.

Differential conductance curves at zero temperature for various Z values, calculated using the BTK model, are shown in Figure 3.3(b). In the case of no barrier ($Z = 0$) and for $E < \Delta$ the differential conductance is twice that of the normal state because only the Andreev reflection process is possible, and this process transfers double charge in the superconductor for each incident

electron. By contrast, in the strong barrier limit, there is no conductance in the gap; current is carried by quasiparticles above the gap.

Boundary Resistance in NS Structures

Pippard et al. [23] were the first to measure a sharp increase in the resistance of an SNS structure near the transition temperature of the superconductor. They proposed an explanation based on an additional boundary resistance associated with a discontinuous jump in the electric potential at the N/S interface due to zero electric field inside the superconductor. Yu and Mercereau [24] showed that the potential in the superconductor is not zero throughout, but decays exponentially. The works of Tinkham and Clarke [22] and Clarke [25] revealed that this potential on the superconducting side of the interface is due to quasiparticle charge imbalance.

Hsiang and Clarke [26] have proposed a theory to explain the rise in the resistance of SNS structures near T_c. The boundary voltage V_b that results from charge imbalance, divided by the total current $I = I_{QP} + I_{\text{pairs}}$, is expressed as a boundary resistance:

$$R_b = \frac{Z(T)\lambda_Q^* \rho_S}{A} \quad , \tag{3.4}$$

where ρ_S is the normal state resistivity of the superconductor, A is the cross-sectional area of the interface, and $Z(T)$ is a universal function of temperature. As $T \rightarrow T_c$, $Z \rightarrow 1$. In this case the boundary resistance is equal to the resistance of a length λ_{Q^*} of the superconductor in the normal state.

3.1.3 Andreev Reflection

We now discuss in more detail the process of Andreev reflection. An electron in a normal metal incident on the interface with a superconductor with energy $\epsilon < \Delta$ cannot be transmitted because there are no states available in the superconductor at the same energy, so it is reflected back. Andreev [27] realized that a peculiar type of reflection takes place: the electron is reflected as a hole into the normal metal, and a Cooper pair is transmitted in the superconductor. Figure 3.4 illustrates the differences between regular reflection and Andreev reflection.

We now discuss the characteristics of the Andreev reflection process.

1. Retro-reflection: The reflected hole has the same momentum as the incident electron, but opposite velocity. Therefore, the reflected hole retraces the path of the incident electron. This retro-reflection is perfect only for electrons with energy equal to the Fermi energy. If the energy

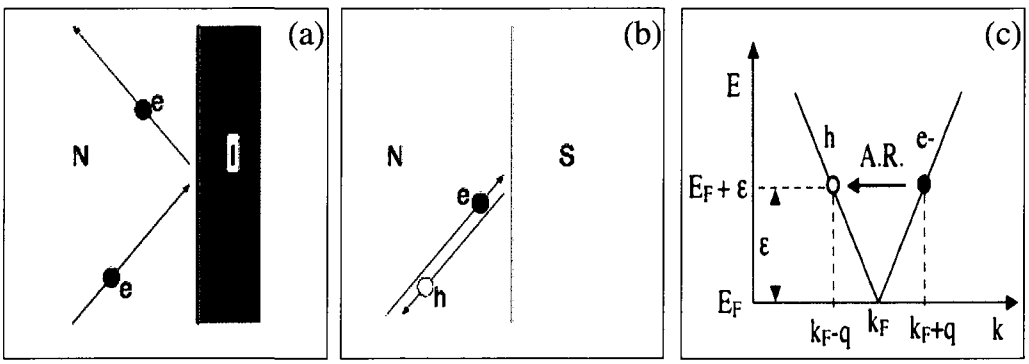

Figure 3.4 Reflection processes that occur in a normal metal: (a) Normal (specular) reflection at the interface with an insulator. The process conserves charge, but does not conserve momentum. (b) Andreev retro-reflection by a superconductor for incident electron with energy near the Fermi level ($\epsilon < \Delta$). The process does not conserve charge, but conserves momentum. From [28]. (c) Wave-vector difference between the incident electron and reflected hole for energy ϵ above the Fermi energy. From [29].

is higher than that, $E_F + \epsilon$, the electron wave-vector k_e is larger than the Fermi wave-vector k_F: $k_e = k_F + q$. The reflected hole has a wave-vector $k_h = k_F - q$, so the difference in wave-vectors is $\delta k = 2q$ (see Figure 3.4 c.). It follows that the incident electron and the reflected hole have different wavelengths in the normal metal.

2. Opposite spin and charge: An incident spin-up electron is reflected into a hole with opposite spin. All incident electrons can be Andreev reflected at the superconductor–normal metal interface because the normal metal spin-up and spin-down bands of electrons are identical. This spin-flip reflection will become important in the F/S structures due to the different spin bands of the ferromagnet.

The incident negatively charged electron is reflected as a positively charged hole; this results in an apparent $2e$ charge loss. However, charge $2e$ enters the superconductor as a Cooper pair; the missing charge is only with respect to excitations. Therefore, the Andreev process enhances the current, and reduces the resistance.

3. Coherence: The reflected hole acquires a phase shift due to the phase of the superconducting wavefunction $_S$. It also carries phase information about the electron phase $_e$. Therefore, the Andreev reflection of a state at energy ϵ is accompanied by a phase change of $\delta = {}_S + \arccos(\epsilon/\Delta)$. For an incident electron at the Fermi energy (i.e., $\epsilon = 0$), the reflected hole has a phase shift of $\pi/2$.

4. Energy conservation: If the incoming electron has energy ϵ above the Fermi energy, then the reflected hole will have energy ϵ below the Fermi level.

3.1.4 The Proximity Effect

Transport properties in SN heterostructures can be modeled using two types of approaches. One approach is the Andreev reflection process described in the previous section. The other approach considers the effects of the superconducting order parameter penetration into the normal metal side; the induced superconducting properties into the normal metal region are referred to as the superconducting proximity effect.

The proximity effect is described in terms of Cooper pairs diffusing into the normal metal region. This process is regarded as equivalent to the Andreev reflection process: a reflected hole moving away from the S/N interface is equivalent to an electron moving towards it, so the Andreev reflection can be seen as two normal metal electrons being injected in the superconductor, and converted into a Cooper pair. The two normal electronic states correlated by the Andreev reflection at the interface are called "Andreev pairs". Being correlated through the pair potential in the superconductor, we can view them as Cooper pairs induced in N by the proximity with S. Therefore, the absorption of Cooper pairs in a superconductor through Andreev reflection is equivalent to the transfer of Cooper pairs out of the superconductor.

The Andreev reflection process generates phase correlations in a system of non-interacting electrons. These correlations decay as Cooper pairs/Andreev pairs diffuse away from the interface. As mentioned in the previous section, retro-reflection at energies greater than the Fermi energy results in a wave vector difference between the electron and the hole; the phase difference between them will increase as the pair travels through the normal metal.

At a distance L from the S/N interface, the phase shift is $\delta\varphi = L^2/L_\epsilon^2$, where $L_\epsilon = \sqrt{\hbar D/\epsilon}$ is the energy-dependent phase coherence length. This mesoscopic length represents how far the electrons in a Cooper pair will dephase when traversing the normal metal. At a distance smaller than L_ϵ the phase drift is small, and scattering by impurities affects the electron and the hole the same way. However, at a distance L_ϵ, the phases and the trajectories of the two particles have shifted enough that the scattering becomes decorrelated. For this reason the length L_ϵ is called the coherence length of the electron pair, and is given by the minimum between the thermal coherence length L_T, and the electron phase coherence length L_φ: $L_\epsilon = \min(L_T, L_\varphi)$. At energies $\epsilon = 2\pi k_B T$, the thermal length is the characteristic decay length. At energies close to the Fermi level ($\epsilon \approx 0$), the coherence length is given by the single-electron phase breaking length. The phase-breaking events in the normal metal are inelastic processes and external magnetic fields.

The phase shift $\delta\varphi$ can also be written in terms of energy as ϵ/E_{Th}, where $E_{Th} = \hbar D/L^2$ is

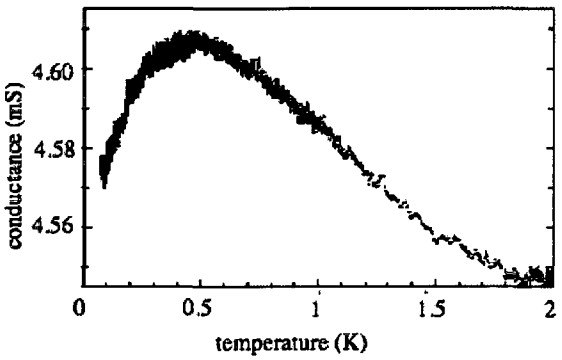

Figure 3.5 Temperature dependence of the conductance of a N/S junction. The conductance first rises as the temperature is lowered, reaches a maximum at $G \approx 1.015\ G_N$, and then it drops back to the normal state value at $T = 0$. This behavior is called re-entrance. From [28].

the Thouless energy of a normal metal sample of length L and diffusion constant D. Therefore, only electrons with energy below the Thouless energy are still correlated at a distance L from the interface.

The Thouless energy was originally introduced as the inverse diffusion time of electrons in a disordered conductor; it later emerged as an important energy scale in mesoscopic superconductivity. The Thouless energy is the characteristic energy scale in proximity-induced superconducting effects in the normal metal. In the following sections we will see that the minigap that opens in the density of states of a normal metal in contact with a superconductor is on the order of E_{Th}; the non-monotonic temperature and voltage dependence of the conductance of a proximity-coupled normal metal wire has a maximum at $k_{\mathrm{B}}T$ or $eV \approx E_{\mathrm{Th}}$; and, in long diffusive SNS junctions, the characteristic voltage $I_c R_N$ is determined by a universal function of the Thouless energy.

3.1.5 The Re-entrance Effect

The proximity effect results in an enhancement of the conductivity of the normal metal. As the temperature is lowered below the transition temperature of the superconductor, the conductance of an NS structure increases above the normal state value G_N, reaching a theoretical maximum of 15% of the normal state conductance at a temperature of about $5E_{\mathrm{Th}}/k_{\mathrm{B}}$ [30]. As the temperature is lowered further, the conductance decreases and, at $T = 0$, it is exactly equal to the conductance of the normal state, $G = G_N$. This non-monotonic behavior is illustrated in Figure 3.5 and is referred to as the re-entrance effect.

The temperature dependence is understood as follows. At temperatures right below T_c, the conductance of the structure increases because superconductivity expands into the normal metal, effectively shrinking the normal metal part of the system. However, below a specific temperature,

the conductance starts decreasing. This surprising behavior is generally explained in terms of a real gap that develops in the density of states of the normal metal, $\Delta_N \sim \min(\Delta, E_{\mathrm{Th}})$, as a result of the penetration of superconducting correlations into N. The presence of the gap means that there are fewer states available for carrying current, and therefore the system conductance decreases.

The SN conductance is always greater than its normal state value. Understanding why the $T = 0$ conductance is not smaller than G_N requires more analysis. Golubov et al. [30] have shown that the re-entrant behavior is due to non-equilibrium effects in the normal metal generated by the presence of both superconductivity correlations and the penetration of an electric field that drives the quasiparticle distribution out of equilibrium. Therefore, both correlated and uncorrelated electrons contribute to the current, and the conductance does not become lower than G_N.

3.1.6 The Josephson Effect

The Josephson effect is a phenomenon manifested by the flow of non-dissipative DC current, or supercurrent, between two superconductors coupled by a weak link. The Josephson supercurrent is a function of the difference Δ in the macroscopic phases of the two superconductors:

$$I_S = I_c \sin \Delta \quad , \tag{3.5}$$

where I_c is the maximum supercurrent that can flow. This critical current depends on the properties of the weak link.

If the weak link is a normal metal, the structure is called an SNS junction. The first experiments with SNS junctions were performed on layered structures, with the thickness of the N layer on the order of the superconducting coherence length ξ_S. The proximity effect was described by a spatial-dependent pairing correlation function, which decays inside the normal metal, and supercurrent flow was understood as resulting from the overlap of these correlation functions of the two superconductors.

Experiments on mesoscopic SNS Josephson junctions fabricated in a planar geometry, with a normal layer longer than ξ_S, showed that the above picture does not provide an exhaustive understanding of the phenomena observed. The Andreev reflection is the fundamental process which enables supercurrent through these junctions, and the microscopic mechanism responsible for supercurrent is the transport of correlated electrons between the two superconductors. In a ballistic SNS junction, where the length of the normal metal is smaller than the elastic mean free path,

electron trajectories are well defined; Andreev bound states are formed [31–33], and they carry the supercurrent. In the case of diffusive transport, Andreev bound states are not present; the superconducting correlations in the normal metal are described by the "supercurrent-carrying density of states" function. Supercurrent can flow if the length of the normal wire is smaller than the phase coherence length in the normal metal L_ϵ. A general study of the Josephson effect in diffusive SNS junctions can be found in the work of Zaikin and Zharkov ([34]).

The maximum supercurrent that an SNS junction can carry depends on the length of the normal wire. There are two cases: in a long SNS junction defined by a length $L > \xi_S$ (or equivalently, $E_{\rm Th} < \Delta$), the critical current at $T = 0$ is given by $eR_N I_c = 10.82 E_{\rm Th}$; in the limit of short junctions $L < \xi_S$, $eR_N I_c = 2.07\Delta$, where R_N is the normal state resistance of the SNS structure. Therefore, in a long junction the normal metal determines the properties of the system, while in a short junction, the superconductor is responsible for the observed effects.

3.1.7 Multiple Andreev Reflections

In short SNS junctions, with length comparable to or smaller than the superconducting coherence length $L \lesssim \xi_S$ ($E_{\rm Th} > \Delta$), electrons and holes with subgap energies resulting from Andreev reflection processes at the two interfaces are trapped in the normal metal once the critical current is exceeded. In order to escape as quasiparticles in the superconducting electrodes, they need more energy, and they gain it by undergoing multiple Andreev reflections (MARs) at the two S/N boundaries. If a voltage bias V is applied across the junction then, with each passage through the normal metal, the electron (or the hole) gains eV in energy. After several cycles of Andreev reflections, the energy is raised above the gap energy, and quasiparticles can enter the superconductor. In these junctions transport is described by the coherent MAR theory [35]. The current-voltage characteristic of these junctions shows "subharmonic gap structure" (SGS), which refers to current singularities at voltages $V_n = 2\Delta/ne$, with $n = 1, 2, 3, \ldots$ representing the number of reflection cycles.

In a long SNS junction with length L satisfying $\xi_S < L < L_\epsilon$ ($E_{\rm Th} < \Delta$), coherent transport is determined by the Thouless energy $E_{\rm Th}$. Here two regimes are present. In the low-bias regime $eV < E_{\rm Th}$, the MAR process is coherent, and the proximity effect gives rise to SGS with additional peaks at $V_n = 2(\Delta + E_{\rm Th})/2ne$ [36]. For high bias voltages $eV > E_{\rm Th}$ transport occurs via incoherent MARs, which show excess noise compared to the NNN system [37].

3.2 Superconductor–Ferromagnet Heterostructures

3.2.1 Modified BTK Model for Transport Across an F/S Interface

In a ferromagnet–superconductor structure the Andreev reflection process is modified due to the presence of different spin bands for spin-up and spin-down electrons. Therefore, the incoming electron and reflected hole occupy different spin bands. Consequently, the Andreev reflection probability is limited by the number of minority carriers in the ferromagnet. For example, in the case of a fully polarized ferromagnet ($P = 1$), Andreev reflection cannot occur because there are no spin-down states available for the reflected hole. For arbitrary polarization, the conductance at zero bias voltage becomes $G(0) = 2(1-P)G_N$, as compared to $G(0) = 2G_N$ for an unpolarized metal. This result is used to experimentally measure the degree of spin polarization of a ferromagnet in the so-called point-contact Andreev reflection (PCAR) method.

Transport in FS structures is described by an adaptation of the BTK theory to include spin polarization [38]. Figure 3.6 shows normalized conductance curves calculated using this modified model. In panel (a) the interface transparency is high, and we notice that for $P = 0$ the conductance is twice the normal state value, as expected. As the polarization is increased, the conductance decreases, and reaches zero in the case of a fully polarized ferromagnet. In panel (b) and (c) the spin polarization is kept constant; as the barrier strength Z is increased, Andreev reflection becomes suppressed, and sharp peaks appear at energies equal to $\pm\Delta$.

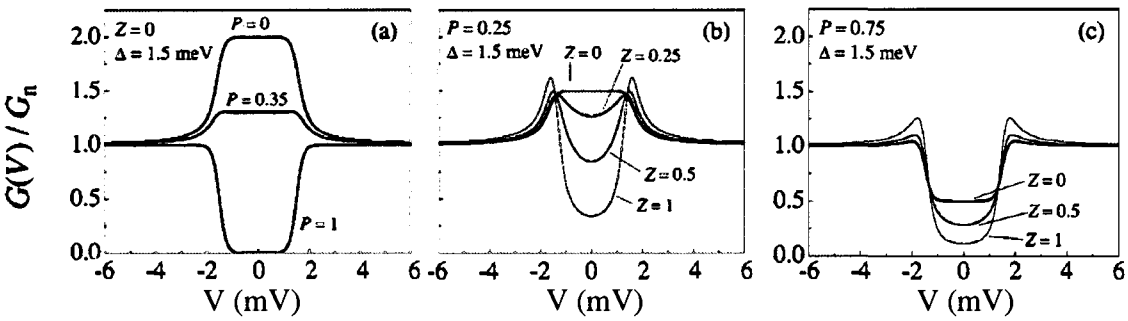

Figure 3.6 Normalized conductance curves for transport across an F/S interface. P is the polarization of the ferromagnet, Z is the barrier strength, and Δ is the superconducting gap. (a) High interface transparency SF structures: as P increases, the normalized conductance decreases. (b) and (c) For a fixed value of P, the conductance decreases as the barrier strength increases. Reproduced from [38].

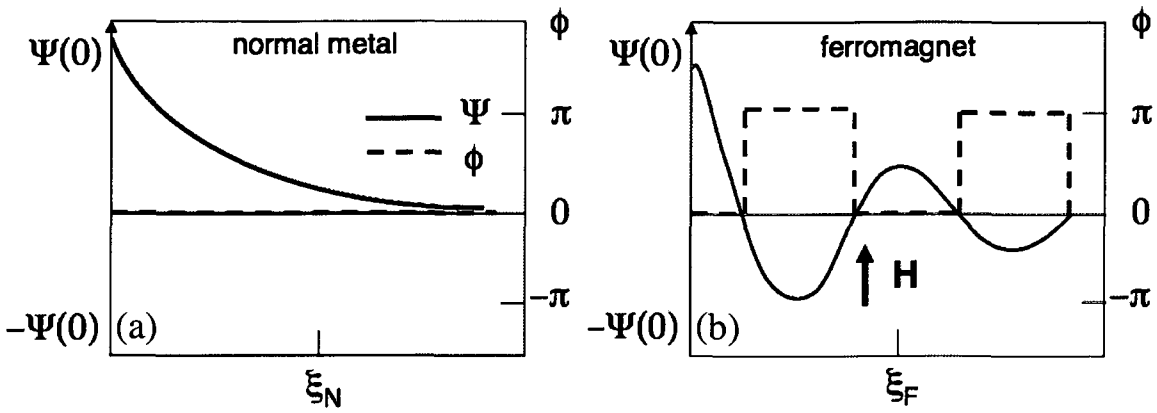

Figure 3.7 The decay of the superconducting order parameter inside a normal metal (a), and inside a ferromagnetic material (b). The normal metal coherence length L_ϵ is denoted here by ξ_N.

3.2.2 Proximity Effect in Ferromagnets

The proximity effect in an SF structure has a very different manifestation compared to the normal metal case. In a normal metal the order parameter decay is a monotonic function of distance x from the interface, as illustrated in Figure 3.7(a):

$$\Psi(x) = \Psi(0)e^{-x/L_\epsilon} \quad , \tag{3.6}$$

where $\Psi(0)$ is the magnitude of the order parameter inside the bulk of the superconductor.

When Cooper pairs penetrate into a ferromagnet, the energies of the spin-up and spin-down electrons are shifted by the exchange field by an amount $2E_{\text{exch}}$, where E_{exch} is the exchange energy of the ferromagnet. In order to conserve the total energy, the electrons in a Cooper pair adjust their kinetic energies. As a consequence, the spin-up electron accelerates and the spin-down electron decelerates, so the Cooper pair acquires a finite center-of-mass momentum $Q = 2E_{\text{exch}}/\hbar v_{\text{F}}$. This induces spatial oscillations of the pair amplitude in the ferromagnet, illustrated in Figure 3.7(b). The order parameter at a distance x inside a ferromagnet has the form:

$$\Psi(x) = \Psi(0)e^{-x/\xi_F}\cos(Qx) \quad , \tag{3.7}$$

In diffusive proximity-coupled ferromagnet-superconductor systems the expected penetration length of pair correlations in the ferromagnet is given by the exchange length $\xi_F = \sqrt{\hbar D_F/2\pi E_{\text{exch}}}$ where D_F is the diffusion constant of the ferromagnet, and $E_{\text{exch}} = k_{\text{B}}T_{\text{Curie}}$. For a strong ferromagnet such as cobalt, the exchange length is on the order of a few nanometers.

The proximity effect has been investigated in SFS multilayers formed with a diluted ferromagnetic barrier, usually CuNi or PdNi alloys [39], which reduces the exchange energy, thus increasing ξ_F. Supercurrent can flow in these structures provided that the thickness of the weak ferromagnetic layer is less than 10–20 nm. Therefore, the proximity effect in SF layered structures has short range.

Boundary Resistance in FS Structures

In a superconductor–normal metal system, the difference between the resistance of the structure in the normal state of the superconductor R_{NN} and the resistance in the superconducting state R_{NS} is determined by the extent of the proximity effect inside the normal metal, in addition to the loss of resistance of the superconductor. As discussed previously, in FS structures the contribution of the classical proximity effect to the resistance is small. However, there is another effect that can have a large contribution to the variation in resistance below the critical temperature. This effect is spin accumulation, and the mechanism by which it arises has been explained by de Jong and Beenakker [40].

Above the critical temperature in a FS system, spin-polarized current can flow through the entire structure. The conductance is given by:

$$G_{\mathrm{FN}} = \frac{e^2}{h}\left(N_{\downarrow} + N_{\uparrow}\right) \ . \tag{3.8}$$

In the superconducting state, all spin-down electrons can be Andreev reflected into spin-up holes. These reflections contribute $2e$ to the conductance, thus doubling its value from that of the normal state. However, the reflection is incomplete for the spin-up electrons, since the number of spin-down channels into which the holes can be reflected is less than the number of spin-up channels. The conductance in this case has the form [40]:

$$G_{\mathrm{FS}} = \frac{e^2}{h}\left(2N_{\downarrow} + 2\frac{N_{\downarrow}}{N_{\uparrow}}N_{\uparrow}\right) = 4\frac{e^2}{h}N_{\downarrow} \ . \tag{3.9}$$

Comparison of G_{FS} and G_{FN} shows that below T_c, the conductance can decrease compared to the value in the normal state if $N_{\downarrow}/N_{\uparrow} < 1/3$, or it can increase if the ratio is larger than $1/3$. Taking this idea one step further, Jedema et al. [41] have shown that the necessity to match the spin-polarized current coming from the ferromagnet with the spinless current inside a superconductor causes spin accumulation at the interface, inside the ferromagnet. This spin accumulation is expressed as a spin contact resistance of the form:

$$R_{\mathrm{FS}}^{(C)} = \frac{P^2 \lambda_{\mathrm{sf}}}{\sigma_F (1 - P^2) A} \quad , \tag{3.10}$$

where P is the polarization of the current in the ferromagnet, λ_{sf} is the spin-flip length, $\sigma_F = \sigma_\uparrow + \sigma_\downarrow$ is the conductivity of the ferromagnet, and A is the cross-sectional area. This spin accumulates over a distance equal to the spin-flip length.

3.2.3 Long-Range Proximity Effect

The expectation of a very short coherence length inside a ferromagnet has been reconsidered theoretically due to several puzzling experimental results [42–44]. Giroud et al. [42] observed a reentrant behavior of the resistance as a function of temperature in a cobalt ring in contact with an aluminum wire. An analysis of the measurements in terms of the proximity effect led the authors to report the penetration of superconducting correlations into the ferromagnet a distance of 180 nm, much longer than the estimated coherence length in cobalt, $\xi_F \sim 3$ nm.

Soon after, Lawrence and Giordano [43] reported a similar behavior in the temperature dependence of the resistance of nickel wires placed between tin electrodes. They estimated a proximity effect of up to 46 nm in nickel. The same year, Petrashov et al. [44] reported a "giant" proximity effect in nickel wires in contact with aluminum films, with a penetration of correlations to a distance of 600 nm. In all these experiments, the interpretation based on long-range proximity effects arose due to the re-entrant-like shape of the resistance versus temperature curves, which is a hallmark of the proximity effect in S-N structures.

Further theoretical calculations investigated the conditions under which pair correlations can survive up to scales longer than ξ_F in ferromagnetic structures. Fominov et al. [45] predicted the formation of spin triplet superconductivity at an S/F interface if the magnetizations of the two ferromagnets are non-collinear. In this case the superconducting correlations penetrate over a distance set by $\xi_F^{\mathrm{triplet}} = \sqrt{\hbar D_F / 2\pi k_{\mathrm{B}} T}$, where D_F is the diffusion constant of the ferromagnet. This expression is similar to the normal metal coherence length. For cobalt, using $D_F = 4$ cm^2/s, we estimate $\xi_F^{\mathrm{triplet}} = 220$ nm at 10 mK. This longer penetration length can be easily understood: a triplet superconducting pair propagating through a ferromagnet will not be broken by the exchange field, since both electrons in the pair have the same spin.

Belzig et al. [46] have modeled the effect of spin accumulation at the S/F interface to show that below a certain temperature it leads to an increase in interface resistance, therefore qualitatively explaining the experimental observations. Their theoretical model, presented in detail in chapter 6,

does not include the proximity effect, but only the contribution of the energy-dependent interface resistance.

The experimental work of Aumentado et al. [47] shows that upon isolating the contribution of the interface from that of the bulk ferromagnetic wire, the re-entrant behavior is due to the interface alone, in compliance with the model of Belzig et al.

3.2.4 Inverse Proximity Effect

Similar to superconductivity, ferromagnetism is a long-range phenomenon. When a ferromagnet is brought into proximity to another material, the ferromagnetic order leaks into the material, affecting the density of states. In Chapter 2 we discussed the spin polarization leakage into the normal metal. In a superconductor–ferromagnet structure, ferromagnetic order modifies the density of states near the interface through the exchange interaction, and applies a magnetic field on the superconductor due to its magnetization.

Several authors have discussed the inverse proximity effect in terms of magnetization leakage into the superconductor. In [48], the authors find the magnetic leakage to be on the order of the Fermi wavelength. Bergeret et al. [49; 50] proposed that a screening magnetic moment is induced in the superconductor in proximity to a ferromagnet. In this physical picture, Cooper pairs at the interface share the electrons between the superconductor and ferromagnet such that the spin of the electron in the ferromagnet is parallel to the magnetic moment of the ferromagnet, while the other electron, present in the superconductor, has spin opposite to the magnetization.

Bergeret and Garcia [51] modify this picture slightly by proposing that the polarization at the Fermi level in the ferromagnet determines the screening in the superconductor. According to their calculation, if the density of states at the Fermi level of the majority electrons is larger than the density of states of the minority electrons, then the magnetization of the system is reduced by lowering the temperature below T_c. If, however, the polarization at the Fermi level is due to minority electrons, then the magnetization is enhanced, and the magnetic moment of the ferromagnet is antiscreened by the electrons in the superconductor.

3.3 Nonlocal Processes: Crossed Andreev Reflection and Elastic Co-tunneling

So far we have discussed the case of single normal metal or ferromagnetic wires attached to superconductors. At subgap energies, Andreev reflection governs the conductance of such structures. If another normal wire is attached to the same superconductor at a distance from the first one that is less than the superconducting coherence length (see Figure 3.8(a)), then two additional transport processes are possible. The first one, elastic co-tunneling (EC) (Figure 3.8(b)) involves direct electron transfer between the two normal metal probes. In the other process (Figure 3.8(c)), an electron injected from terminal N1 can reflect as a hole in the second terminal, and a Cooper pair is transmitted in the superconductor; this is called crossed Andreev reflection (CAR).

The detection of these processes is done by injecting current into one of the wires (N2 in Figure 3.8(a)), and measuring voltage across the other one (N1 in Figure 3.8(a)). The result is then analyzed in terms of the nonlocal conductance, given by the ratio of the current and the nonlocal voltage. Both processes (EC and CAR) contribute to the nonlocal conductance, and can be distinguished based on the sign of the nonlocal voltage: if CAR is dominant then, since holes have the opposite charge of electrons, the voltage across N2 will have a sign opposite to that measured in the normal state of the superconductor. If the EC process has higher probability, then the sign of the voltage is the same as in the normal state. If the probabilities of the two nonlocal reflections are the same, then their contributions cancel each other, and the measured voltage is zero.

In the case of CAR, the reflection process is equivalent to the separation of the electrons in a Cooper pair into the different leads, leading thus to the nonlocal transport of an entangled electron pair. Recher et al. [2], and Byers and Flatte [1] were the first ones to suggest this mechanism.

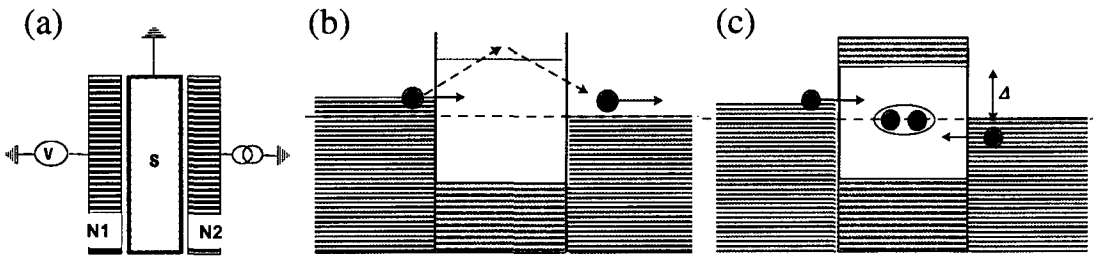

Figure 3.8 Processes at N/S interfaces. (a) NSN structure geometry and measurement configuration. (b) Schematic representation of the elastic co-tunneling process in energy space. (c) Crossed Andreev reflection process. Adapted from [52].

The early theoretical work on the nonlocal conductance of NSN hybrid structures [53] demonstrated that the EC contribution to the nonlocal conductance exactly cancels that of CAR in the lowest order of perturbation theory in the interface transmission. In connection with the experimental result of Russo et al. [6] that claimed evidence for the occurrence of EC at low bias energy and of CAR at higher energies in the same structure, higher order analysis was done by Melin [54], who found that the crossed resistance can exceed the elastic cotunneling contribution if the normal metal phase coherence length or the energy are large enough.

The goal of the theories of nonlocal Andreev processes is to calculate the cross-conductance. The first such calculation done by Falci et al. [53] in a structure with tunnel contacts A and B, and considering ballistic transport in the superconductor, gives the following result:

$$\begin{pmatrix} G_{\mathrm{EC}} \\ G_{\mathrm{CAR}} \end{pmatrix} \approx |T_A d_A|^2 |T_B d_B|^2 \frac{\exp(-2L/\pi\xi_0)}{(k_F L)^2} \begin{pmatrix} \cos^2(k_F L) \\ \sin^2(k_F L) \end{pmatrix} . \tag{3.11}$$

In this expression $T_{A,B}$ and $d_{A,B}$ are the tunneling probabilities at each interface, and the size of the two contacts, respectively, while L is the distance between the contacts. This result shows that the conductance of the two processes decays exponentially with the ballistic superconducting coherence length ξ_0, and attenuates as $1/L^2$ as the distance between the contacts increases. This result is derived for a single channel transport. In practice, the wires are large and consist of multiple, independent conductance channels, so that the oscillatory character in equation 3.11 averages away with no interference. Therefore, the magnitude of the two processes is approximately equal, so they will not be distinguishable in normal metal systems.

For practical purposes the diffusive limit is more useful, and this was examined by Feinberg [55], who modified the spatial dependence in equation 3.11 into

$$\frac{\exp(-L/\xi_S)}{(k_F L)(k_F l_e)} , \tag{3.12}$$

where $\xi_S \sim \sqrt{l_e \xi_0}$ is the dirty limit coherence length, and l_e is the elastic mean free path. This result says that in diffusive systems it is possible to observe EC and CAR processes over a larger separation between the probes compared to the ballistic system.

While there has been extensive theoretical work devoted to determining the relative strength of these subgap processes, the experimental reports are very few. Cadden-Zimansky and Chandrasekhar [4] find that the nonlocal resistance of an NSN structure with transparent interfaces is positive, indicating that the EC contribution is larger than that of CAR. Kleine et al. [5] have

recently demonstrated a systematic dependence of these nonlocal processes on the interface transparency, and find that for small contact resistances CAR is the dominant process.

Deutscher and Feinberg [56] were the first to realize that, due to the spin structure of Cooper pairs, CAR would become the dominant transport process if the two wires are ferromagnetic and have antiparallel magnetization. They predicted that in this magnetization alignment a negative voltage drop would be measured in the nonlocal configuration.

In summary, the current understanding of the nonlocal processes in FSF structures is that, if the two ferromagnets are fully polarized, then for parallel magnetization alignment only EC processes will contribute to the conductance, while for antiparallel magnetizations the conductance is due to CAR. Two experimental signatures are expected. The first is rapid attenuation as the separation L between probes increases, and exponential decay with the ratio of this separation and the superconducting coherence length (i.e., L/ξ_S). The second signature is phase coherence effects between the electrons in the two probes due to correlations acquired by the reflection on the superconductor.

Chapter 4

Sample Fabrication and Experimental Setup

4.1 Sample Design Considerations

There are fairly stringent design requirements that must be met in order to be able to observe CAR and EC processes. First of all, the size of the contact between the ferromagnetic probes and the superconductor should be smaller than the coherence length of the superconductor. This is required in order to avoid quenching superconductivity in the region between the two contacts; if that were to happen, the CAR process would be strongly suppressed. As shown in [57] for the case of weak links, the order parameter is depressed only in the contact region when the contact diameter is much smaller than ξ_S.

The ferromagnetic elements generate magnetic field lines that emanate from one end and close on the other if the magnetic wires are single domain. The fringe fields a few nanometers outside the surface of the probes are as high as the internal field, on the order of 1-2 T. The field decays by an order of magnitude within 10-100 nm of the end. Therefore, the two probes will depress superconductivity in a small region around the tips. Superconductivity will not be completely suppressed due to these fringe fields because the critical field of aluminum for magnetic fields applied in the film plane is much larger ($\sim$ 5 T).

Second, the device would work best if the distance between the tips of the two probes is on the order of, or smaller than, the coherence length, because the probability for CAR and EC processes decays exponentially with ξ_S. This condition makes some superconducting materials not a good choice for these experiments (e.g., Nb, Pb) due to the fabrication difficulty in placing two features this close together ($\xi_S^{Nb} = 40$ nm). We use aluminum as the superconducting material for its relatively long coherence length: in the dirty limit, $\xi_S^{Al} \sim 100 - 300$ nm. Also, aluminum films with reproducible properties are easy to grow. In addition, transition-metal impurities do not have magnetic moments in aluminum [58–60], thus simplifying the interpretation of specific results (e.g., we can exclude Kondo effects).

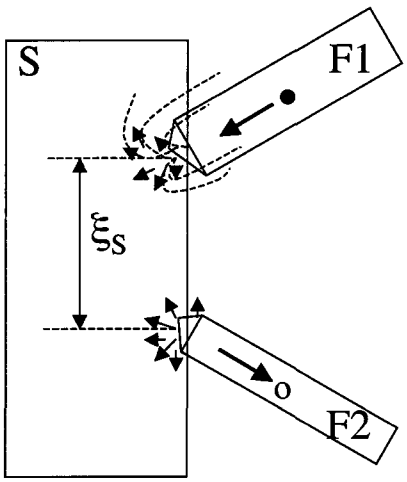

Figure 4.1 Device with two spin-polarized contacts placed at a distance on the order of the superconducting coherence length. Dipolar fringe magnetic fields surround the ferromagnets; they have the same direction as the magnetization of the probe. If the two ferromagnets F1 and F2 have opposite polarization, CAR process is favored: a spin-up electron incident on the interface F1/S can be reflected as a spin-down hole in F2. Perturbation of the superconducting gap occurs in a small region around the FM tips.

Third, in order to avoid quenching magnetism at the tips of the two probes, the exchange field of the ferromagnet should be larger than the superconducting gap. Therefore, the choice of ferromagnets is important, and the strong elemental ferromagnets (Ni, Co, Fe) are good candidates.

There are a few other choices that we made to improve the overall device. For example, we designed the ferromagnetic probes with a pointed tip to ensure single magnetic domain structure in the overlap area. Also, in order to bring the ferromagnetic probes as close together as possible, we designed them at an angle of 60° with respect to each other, thus avoiding proximity-exposure problems during fabrication. We choose to make samples in the transparent contact regime (as opposed to tunnel barrier contact) because in this case the cancellation of EC and CAR signals is predicted to be the smallest [61].

4.2 Fabrication Techniques: Lithography and Metal Deposition

There are two major steps involved in the fabrication of our devices: a lithographical step, in which the device design is transfered onto a substrate, and a metal evaporation step. Each of theses steps is used alternately several times before a single device is completed.

The substrates onto which our devices are fabricated are silicon wafers with a few hundred nanometers of silicon oxide layer on top. These wafers are cut into 10 mm × 10 mm pieces that represent the "chips" on which the devices are created.

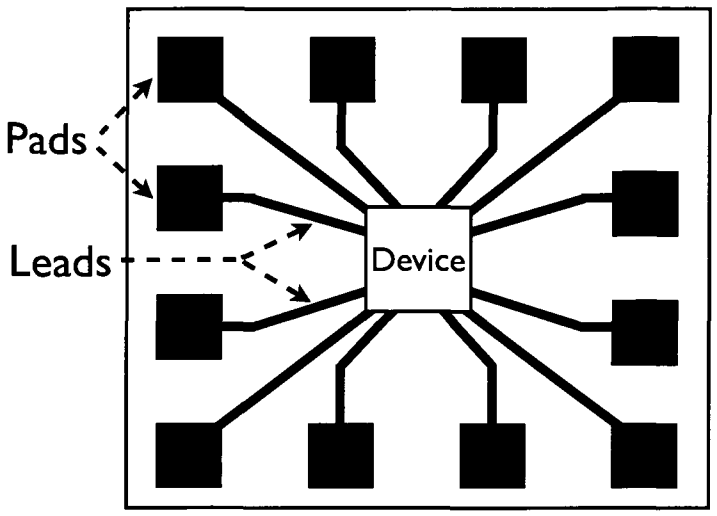

Figure 4.2 Schematic drawing of a chip with 12 pads. The measuring leads converge to the middle, where the device is created at a later time.

The first step in the making of all of our devices is defining the measuring leads and the pads that are used to connect the device to the measurement apparatus. A schematic drawing of the features patterned on the chip is shown in Figure 4.2. These features are large relative to the rest of the device: the pads are 900 μm $\times$ 900 μm, and the width of the leads is 100 μm near the pad, tapering down to 15 μm in the area of contact with the small device. The patterning technique for features of this size is optical lithography, schematically illustrated in Figure 4.3.

The optical lithography procedure involves three steps: coating the chip with a photoresist layer, exposure of the layer to UV light sent through a premade optical mask, and developing of the imprinted features. All steps are performed in a class-100 cleanroom (less than one hundred particles larger than 0.5 μm in each cubic foot of air space).

The photoresist is a liquid polymer sensitive to UV light. We use AZ5214 PR, which gives a thickness of $\sim$ 1.4 μm when spun at 4,000 rpm. After the chip is coated with a few drops of PR (Figure 4.3(a)), we align an optical mask that has the features we want on top of the chip. This is done with an Oriel Mask Aligner and UV Exposure System with a resolution of 2 μm under optimum conditions. Since there are no features on the chip at this point, the alignment is a coarse procedure in which we want to fit the area defined by the pads onto the chip boundaries. Next, UV light is sent through the mask, "exposing" the photoresist. After exposure, photoresist molecules broken down by UV light are removed in a developer solution made of AZ 326 Developer diluted with deionized water in a ratio of 1:5. The result, shown in Figure 4.3(c), is a chip with big pads and leads defined in the photoresist.

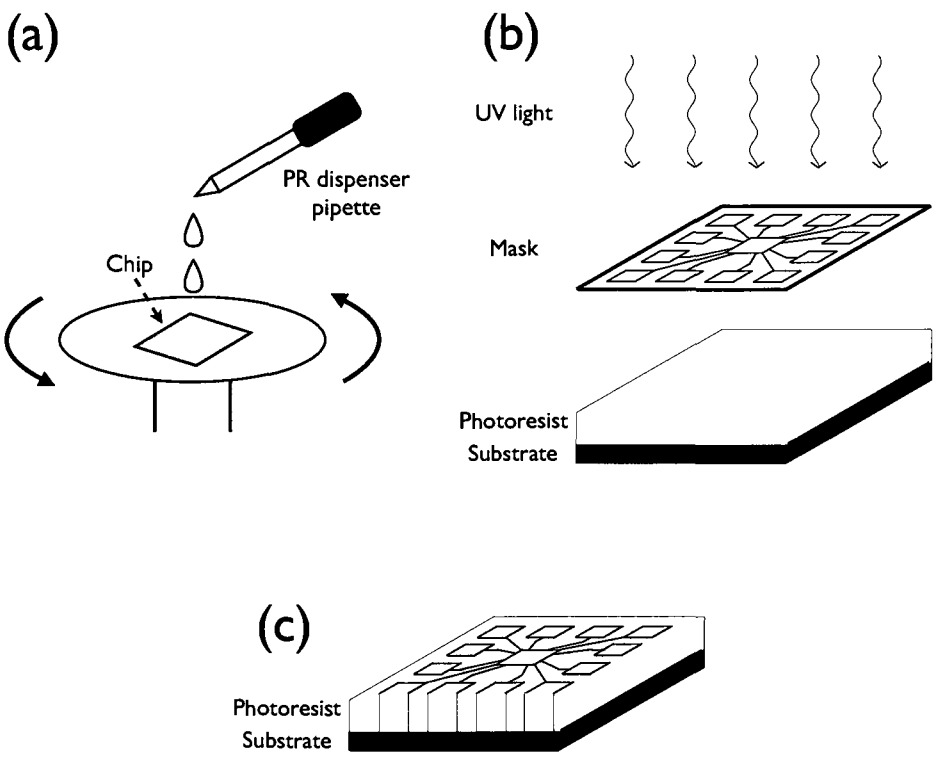

Figure 4.3 Fabrication steps for the optical lithography procedure. (a) Coating the chip with PR on a Automated Photoresist Spinner. (b) Exposure of the PR by UV light though a mask that has the pattern we want to imprint. (c) The result of the mask transfer into the PR after developing.

The next processing step is metal deposition, illustrated in Figure 4.4. Our pads and leads are made of 80–100 nm thick gold, with a base of 10 nm titanium to ensure good adherence to silicon. The metals are deposited by electron beam evaporation in a Temescal evaporation system.

Once taken out of the evaporator the chips are immersed in acetone: this is the "lift-off" fabrication step, in which the photoresist is dissolved. The metals on top of the photoresist layer are also removed. The only remaining metal is that in direct contact with the silicon substrate at the location of the features defined by the lithography step.

Now, having defined the contact pads on the chip, we move on to fabricating the actual devices we are interested in. The small-size features of our devices require electron beam lithography instead of optical lithography. These two processes are very similar in the steps involved; they mainly differ in the chemicals used for coating the chips and developing the features, and the type of mask involved. The polymers sensitive to electron beam energies are polymethyl methacrylate (PMMA) and methyl methacrylate (MMA). The developer is methyl isobutyl ketone (MIBK), which we dilute in isopropanol in a ratio of 1:3 to obtain high resolution features. The mask used to transfer the

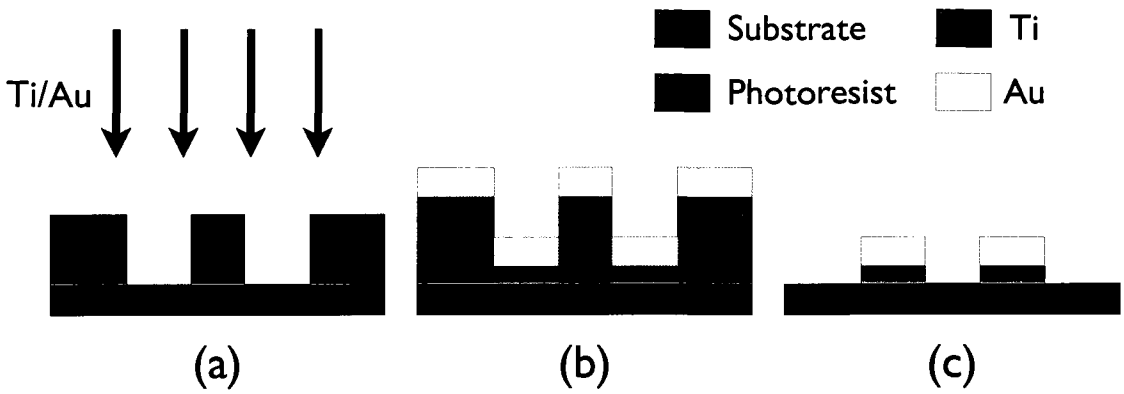

Figure 4.4 Metal deposition for creating the pads and big leads on the chip. (a) Titanium is first deposited to ensure good adherence of the pads to the substrate, followed by ebeam evaporation of gold. (b) The resulting stack of PR, Ti and Au when metal deposition is finished. (c) Sample pads and leads defined after the resist is dissolved in acetone.

desired pattern onto the chip is a computer design file that is read by the ebeam writing instrument. The instrument used for writing our devices is Raith e-Line, an ultra-high resolution electron beam lithography system capable of 5-nanometer line resolution. A finely etched tungsten crystal is the filament from which electrons are extracted by way of a very high potential gradient $V_{\text{ext}} = 5.7$ kV applied between the filament and a nearby anode. The filament and another anode are connected to a high-voltage power supply that will accelerate the extracted electrons to the sample location. The software that runs the instrument reads the design file that has the pattern, and moves the beam across the chip, exposing various areas according to the pattern.

When the e-beam lithography is finished, the chip is immersed in the developer solution. The polymer molecules broken by the electron beam are dissolved, and the result is a series of gaps in the PMMA of width and length equal to the feature sizes.

The metal deposition in all our small devices is done by thermal evaporation in a vacuum in the low 10^{-6} Torr range. The instrument we use is a Commonwealth Scientific Millatron, with a base pressure of 4×10^{-7} Torr. The devices studied in this dissertation differ in the way the metals are deposited; we will therefore describe the procedures separately.

1. FSF Spin Valves

Figure 4.5 illustrates the fabrication of our FSF devices. A thick stack of polymer PMMA/MMA ($\sim$ 90 nm) is exposed by the electron beam writer to define the pattern (Figure 4.5a). The base resist (8.5MMA EL9) has a much larger sensitivity to the electron beam than the top resist (950K PMMA A2); therefore, by controlling the exposure parameters, we can achieve a large "undercut"

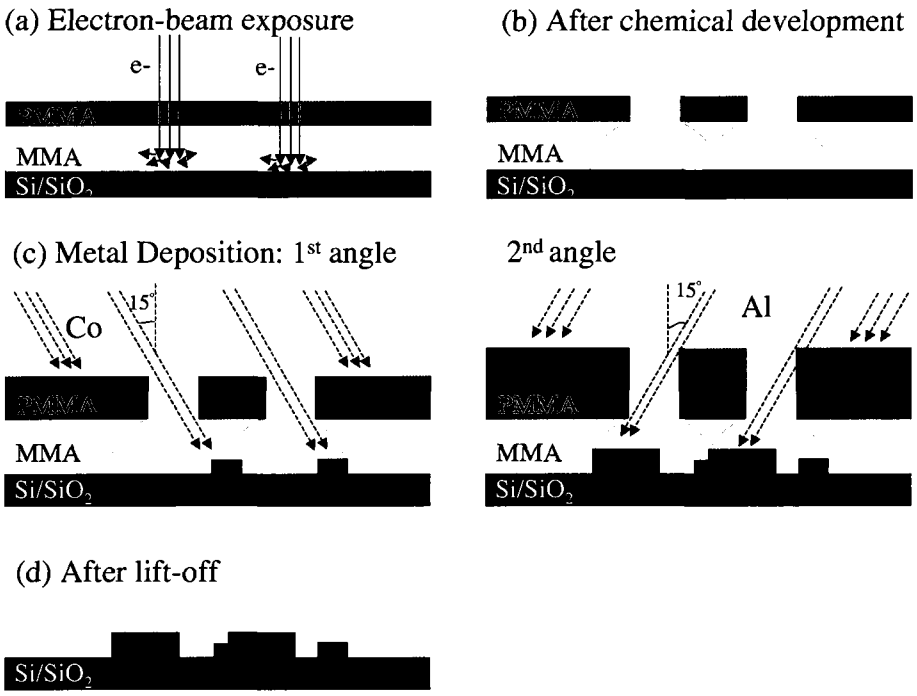

Figure 4.5 Fabrication steps for making FSF lateral spin-valve devices with high-transparency contacts using the shadow-angle evaporation technique.

profile and a suspended layer (see Figure 4.5b). This profile allows us to use a technique called "shadow-angle" evaporation to deposit two different metals on top of each other without breaking the vacuum. First, 20 nm of Co is deposited at an angle of $-15°$ onto the Si/SiO_2; it is important to have this layer first on the substrate so that the film sits flat, thus preventing the formation of magnetization domains. Then 60 nm of Al is deposited at $+15°$ angle to make an overlap of about 60 nm with the tips of the ferromagnetic probes. Scanning electron microscope pictures of finished FSF devices are shown in Figure 4.6.

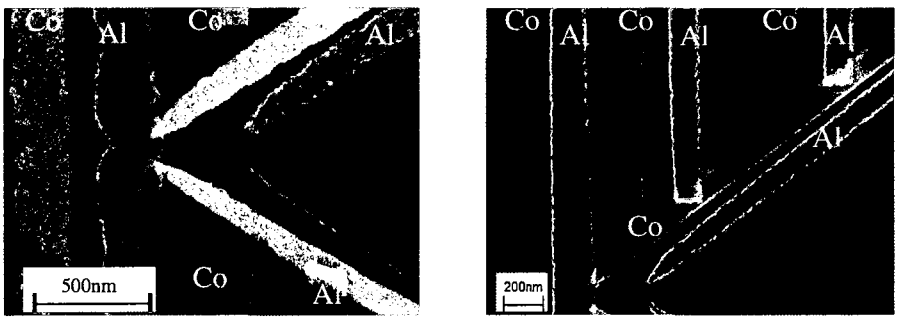

Figure 4.6 SEM images of finished FSF samples. Every line has its shadow, but only the lines of interest are connected to outer pads.

Table 4.1. Wire dimensions and material characteristics in our F F spin-valve devices. All quantities are determined from measured resistivity at 2 K.

	FSF 1			FSF 2			FSF 3		
	injector	detector	S wire	injector	detector	S wire	injector	detector	S wire
Width (nm)	150	120	320	150	120	270	170	130	330
ρ ($\mu\Omega$·cm)	16.0	18.5	2.3	17.4	17.4	2.6	23.6	23.2	1.3
$R_\square$ (Ω)	8.0	9.3	0.38	8.7	8.7	0.43	11.8	11.6	0.21
D (cm^2/s)	3.1	2.7	21.4	2.8	2.8	18.9	2.1	2.1	37.9
l_e (nm)	0.48	0.40	4.9	0.44	0.44	4.3	0.33	0.33	8.7
ξ_F (nm)	1.3	1.2	...	1.24	1.24	...	1.07	1.08	...
ξ_S (nm)	...	...	89	...	...	83	...	...	118
$L_T/\sqrt{\ }$ (nm)	48	45	128	46	46	120	40	40	170

Typical dimensions of the ferromagnetic probes and superconducting wires, along with material properties, are listed in Table 4.1. The resistivity ρ is determined from 4-point resistance measurements at 2 K. The sheet resistance $R_\square$ is then calculated from $R_\square = \rho/t$, with t being the thickness of the material: 60 nm for aluminum, 20 nm for cobalt. The diffusion constant D is determined by the expression $D = 1/Ne^2\rho$, where e is the electron charge and N is the density of states. The values of N we use are $N_{\mathrm{Co}} = 1.27 \times 10^{29}$ eV^{-1} m^{-3} and $N_{\mathrm{Al}} = 2.4 \times 10^{28}$ eV^{-1} m^{-3}. The elastic mean free path l_e is calculated using the equation $D = v_F l_e/3$, where v_F is the Fermi velocity. For cobalt we use $v_F = 1.9 \times 10^6$ m/s, and for aluminum $v_F = 1.3 \times 10^6$ m/s. The exchange length in the ferromagnetic material is given by $\xi_F = \sqrt{\hbar D/2\pi k_{\mathrm{B}} T_{\mathrm{Curie}}}$, with $T_{\mathrm{Curie}} = 1388$ K for cobalt. The superconducting coherence length ξ_S is calculated from the mean free path value as $\xi_S = \sqrt{\xi_0 l_e}$, where $\xi_0 = 1600$ nm is the aluminum coherence length in the clean limit. The thermal length L_T is obtained via the expression $L_T = \sqrt{\hbar D/2\pi k_{\mathrm{B}} T}$.

2. SFS and SNS Loops

The SFS and SNS loop devices presented in Chapter 7 are fabricated by the following steps. First, the overlap between the normal metal wires and the superconducting strip is defined by shadow-angle evaporation of the two metals, as described in the FSF case. Then, the chips are coated again with PMMA (400 nm of 950K PMMA A4), and the loop feature is ebeamed. The last step, metal deposition in the trench that defines the loop, is done after a soft cleaning of the normal metal or ferromagnetic wires using the Ar ion mill of the thermal evaporator. For the SNS SQUIDS we deposit 50 nm of silver as the normal metal, while for the SFS rings we use 20 nm of nickel. SEM pictures of the intermediate step and the finished device are shown in Figure 4.7.

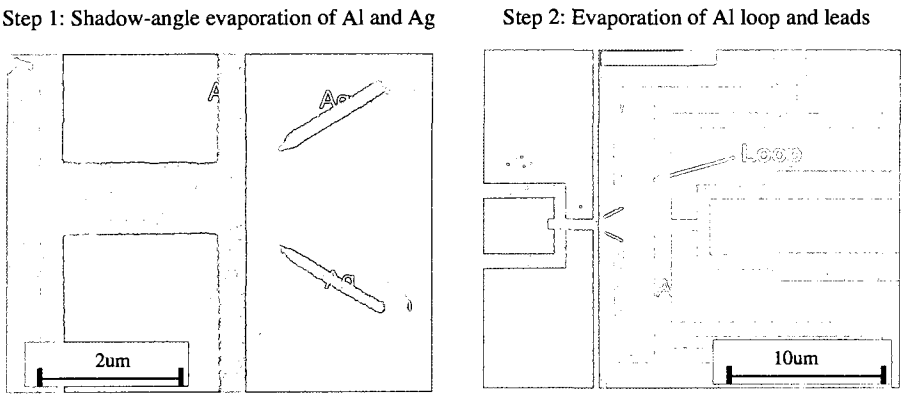

Figure 4.7 SEM images of the steps involved in the fabrication of SNS SQUID devices. The SFS ring structures (not shown) are made the same way.

3. S–FF–S Devices

These devices, although simple in appearance, are the most difficult to make due to their small dimensions. Even though we separate the processing of the ferromagnetic wires from that of the aluminum electrodes, making a good device takes many attempts.

The device fabrication steps are illustrated in Figure 4.8. We start with a thin layer of PMMA (70 nm of 950K PMMA A2), in which we define two narrow, short lines by ebeam exposure. The ferromagnetic wires are then created by straight-on thermal evaporation of 20 nm of cobalt into the ebeamed trenches, followed by lift-off (Figure 4.8 (a)-(c)). These steps do not present difficulties.

The next three steps, involved in making the aluminum electrodes, have an increasing level of difficulty. The first one, ebeam exposure of two relatively large features (the superconducting electrodes) in close proximity (50 nm or less apart) on a thick layer of PMMA (400 nm), requires very good knowledge of the relative impact of the various ebeam exposure parameters.

Once ebeam lithography is finished, the device is loaded into the thermal evaporator. Before the actual evaporation we clean the tips of the cobalt wires that will contact the aluminum electrodes. This is done by soft argon ion-milling (250 V, 50 mA) for one minute. We had some trouble with this step due to a neutralizing current that generally did not in fact neutralize the beam current; therefore, some devices were blown out by the high current incident on the ferromagnetic wires. To prevent this, we continually monitor the evaporation chamber charging during ion-milling, and adjust the neutralizer current appropriately. Right after ion-milling, we evaporate 60 nm of aluminum on the substrate. The last step, the lift-off, is probably the most difficult and least controllable of all steps: the narrow aluminum strip between the two electrodes is very hard to remove. We soak the

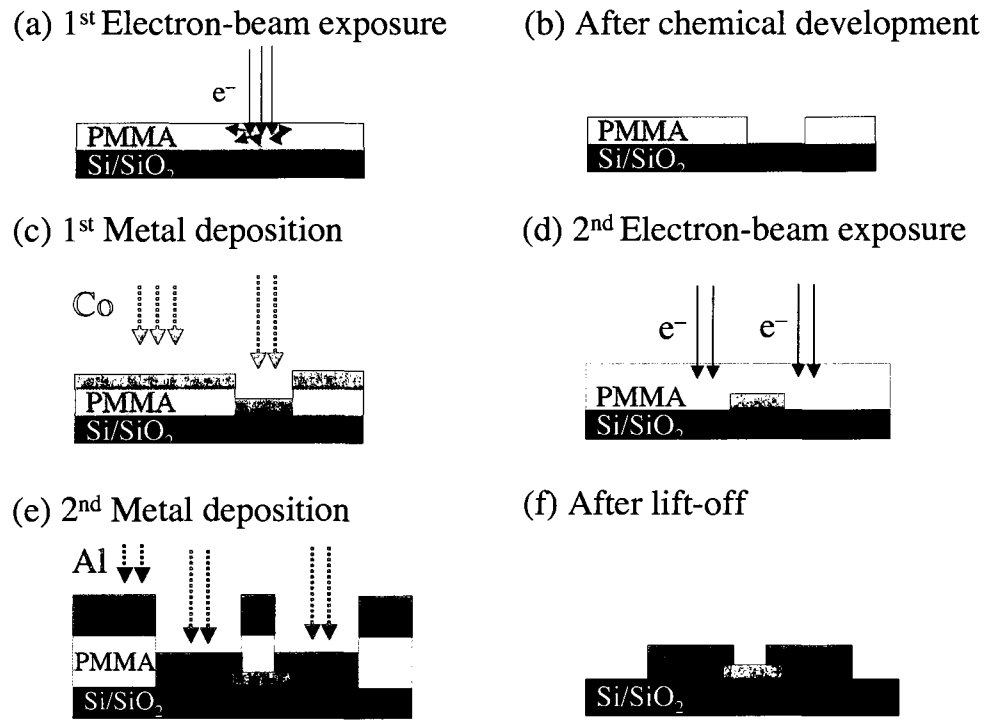

Figure 4.8 Fabrication steps for making S–FF–S devices.

devices for 24 hours in acetone at room temperature, and then gently agitate them in a sonicator bath for about 10 minutes. This procedure seems to give the best results.

SEM pictures of the three finished devices are shown in Figure 4.9. The relevant dimensions of these devices are summarized in Table 4.2.

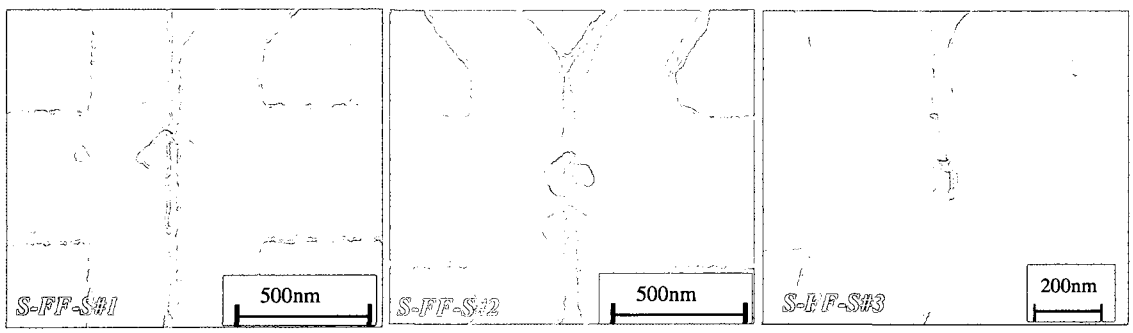

Figure 4.9 Scanning electron microscope images of three measured S–FF–S devices.

Table 4.2. Dimensions of the wires and separation between features in S–FF–S devices estimated from the SEM images shown in Figure 4.9.

	SFFS #1	SFFS #2	SFFS #3
Distance between S electrodes (nm)	35	31	64
Smallest separation between FM wires (nm)	42	42	29
Interface overlap (left, right) (nm)	70, 125	87, 87	29, 71
Width of F1 (nm)	118	125	116
Width of F2 (nm)	104	90	84

4.3 Measurement Instruments

4.3.1 Dilution Refrigerator, Filters and Shielding

All our samples are measured in an Oxford Instruments Kelvinox TLM dilution refrigerator, in which the sample is placed directly into the $^3He/^4He$ mixture. This arrangement ensures good sample thermalization and a high stability of the thermal environment. The base temperature reached during our measurements is 8 mK. We can control the temperature in the range 8 mK - 1.5 K, which is useful for measuring the temperature dependence of signals of interest.

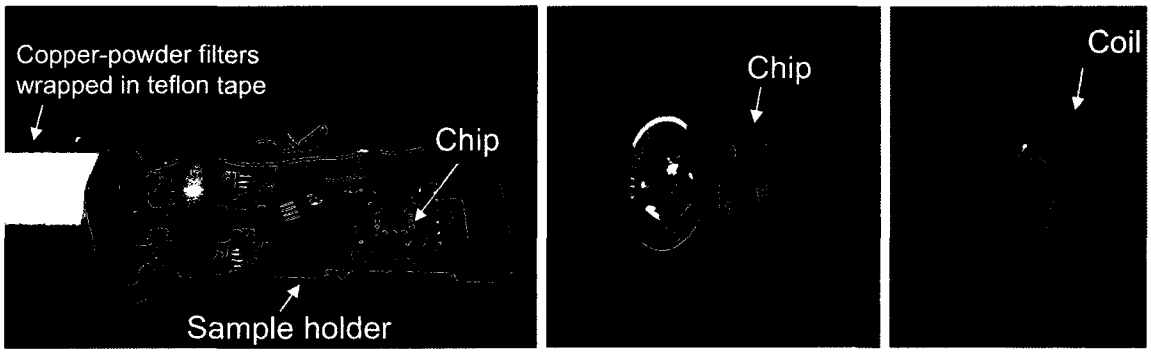

Figure 4.10 Photograph of the sample holder at the bottom of the fridge probe. At this level we also have copper powder filters on twisted pair measurement leads, but they are not visible due to the teflon wrap. A photograph of the hand-made coil for the SNS SQUIDs and SFS rings is shown in the last panel.

The sample is mounted on a sample holder at the bottom of the fridge "probe", which is a rod about nine feet long. The sample holder (Figure 4.10) has a calibrated ruthenium oxide thermometer

on the opposite side of the chip mounting surface. Also placed on the back of the sample holder are 2.2 kΩ resistors in series with the measuring leads to protect from accidental electrical discharge, and to reduce the noise.

The chip is attached to the sample holder with thermal paste. The twelve pads arranged around the edge of the chip are connected to thin copper wires using indium pieces: a small amount of indium is pressed on the pad, then the wire is pressed into it, and another piece of indium is pressed on top for good mechanical contact. The procedure is done on a static mat and with a grounding strap attached to the arm in order to avoid static electricity discharge through the sample, which would destroy it.

The wires connected to the sample are twisted in pairs, and connect to non-magnetic pins attached to the edge of the sample holder. From here wires go to the resistors on the back of the sample holder, and then up on the probe into the powder filters. From this stage they run all the way to a 24-pin Fisher connector at the top of the probe. The resistance of the wires is about 300 Ω above the resistor stage.

The powder filters consist of a metal powder (copper, in our case) and epoxy mixture through which the measurement wires are embedded. The surface area of the grains in the filter allow for rapid attenuation of the RF radiation transmitted though the powder.

Outside the dilution fridge the lines go into the shorting box at the top of the probe, which protects the sample from electrostatic discharge. From here, coaxial cables run to the instruments.

4.3.2 Electronics: DC and AC Electronics, Magnetic Field Bias, Data Acquisition

Measurements are done in an electromagnetically screened room providing shielding from 150 kHz to 10 GHz. Since we do not need to apply a magnetic field for measuring SNS devices, we place an additional level of shielding in the setup: a Cryoperm shield around the sample holder screens magnetic fields that would otherwise compromise our measurements.

The resistance is measured in the standard 4-wire configuration using an ac resistance bridge made by Linear Research (model LR-750). The excitation currents are chosen by selecting both a voltage excitation range and a resistance range on the instrument; then the current sent to the sample is given by the ratio of the two. The frequency of the excitation is set to 15.9 Hz. The instrument communicates with the computer via GPIB (General Purpose Interface Bus).

Similarly, the resistance of the sample holder thermometer is measured by a resistance bridge

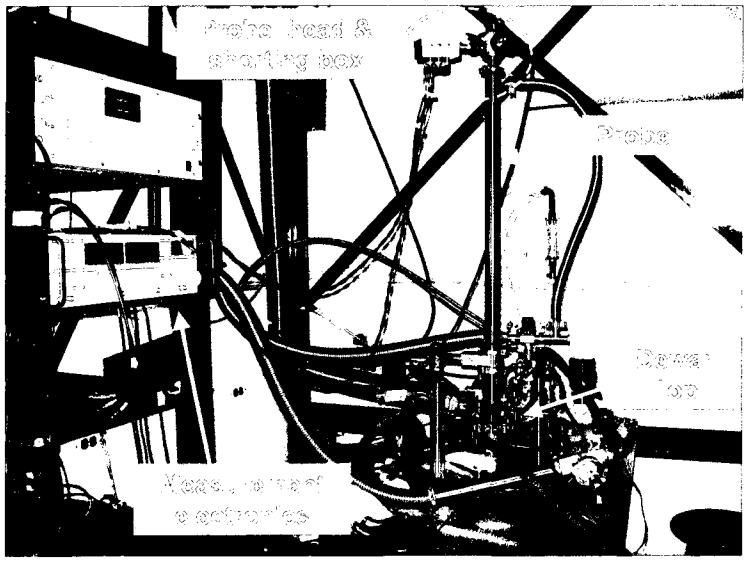

Figure 4.11 Photograph of the top of the Oxford TLM dilution refrigerator used in measuring our devices. The fridge is inside an electromagnetically screened room. Measuring instruments are placed on a rack inside the room, and are connected by coax cables to the sample shorting box at the top of the probe.

made by LakeShore (Model 370), designed for low noise, low excitation power AC resistance measurements. The measured resistance is converted to temperature using the calibration curve of the thermometer. The instrument is interfaced with the computer via GPIB.

Current–voltage (IV) characteristics of the devices are measured using a homemade current supply and an Ithaco 1201 low-noise differential preamplifier. The current supply is battery-powered to reduce 60 Hz noise from the AC line. The preamp can also run unconnected from the AC line. The current supply converts the ac-voltage output of a DAQ board into a dc current. The voltage across the sample is measured using the preamp and the DAQ board analog input. The IVs are taken in bipolar retrace mode: current is first ramped to the maximum desired positive value, then ramped back down to zero, followed by a ramp to the maximum negative value, and finally back to zero.

Differential resistance curves versus current are measured using a small ac excitation superimposed on a dc current bias. The voltage drop across the device is measured by the internal preamp of the LR-750 bridge.

In the case of the SNS SQUIDs we measure the modulation of the critical current by a small magnetic field applied with a hand-made superconducting coil. Niobium-titanium wire, 0.1-mm diameter, is wound onto a Teflon screw about 230 times. The magnetic field, in Gauss, is estimated

to be 480 $\times I_{bias}$. This coil is then placed on top of the chip, as can be seen in Figure 4.10. The current bias of the coil is done by applying 5 mA current with one of our home-built current supplies described above.

The high magnetic field applied for magnetoresistance measurements of the ferromagnetic samples is generated by the Oxford Instruments superconducting magnet immersed in the liquid helium bath of the dilution refrigerator. According to the manufacturer, field sweeps of up to 2 T /min leave the temperature of the mixture unaffected. The current through the magnet coils is controlled by the Oxford Instruments Magnet Sweep Power Supply.

Instrument control and data acquisition programs are done by LabVIEW software. Data analysis and graphing is done using Origin software package.

4.4 Sample Characterization and Measurement Overview

There are four temperature regions in which we characterize our samples through transport measurements:

A) Room temperature – whenever possible, we measure the 2-lead and 4-lead resistance of our devices to make sure that we have relatively low resistance values in our devices, which translates into good interfaces between different layers of material. Also, this step tells us whether or not the small devices have been blown up by electrostatic discharge during the wiring process.

Sometimes we measure the resistance of our devices at room temperature due to conduction through the substrate. The sample pads are lithographically shorted together to protect the sample from electrostatic discharge. When cutting these shorts using either a razor blade or a fine diamond scribe tip, there is a risk of cutting too deep through the silicon dioxide layer that covers the substrate. If this happens, room-temperature conduction from one pad to another occurs both through the device of interest and through the substrate. When temperature is lowered to 4 K, conduction through the substrate freezes, and the only electronic transport path between two pads is through our device.

B) Temperature region right above T_c, the transition temperature of the superconductor. We usually make "above T_c" measurements at a temperature of 1.8 K, which is approximately 0.5 K above T_c. At this temperature we characterize our devices by 4-wire resistance measurements and IV curves. In addition to this, for samples made with ferromagnetic probes, we also do magnetoresistance measurements by applying a magnetic field in plane with and parallel to the ferromagnets.

C) Transition temperature T_c: the resistance of our devices in a small range of temperatures around T_c is recorded while cooling down the sample to "base" temperature. We never stay at this temperature to take measurements.

D) Base temperature, which is the lowest achievable temperature in the mixing chamber of our dilution fridge, usually 9 mK. The electron temperature differs in general from the mixing chamber temperature because of the power dissipated in the sample and its environment. This heating of the electrons may come from the current flowing through the sample during measurements, and from electrical noise and thermal radiation from surfaces surrounding the sample.

The measurements performed on our samples at this temperature consist of IV curves and differential resistance curves. In addition to these, when characterizing samples in the loop geometry, we apply a small magnetic field (a few gauss) perpendicular to the loop plane using a hand-wound coil, and measure either the critical current oscillations of the SNS SQUIDs, or resistance oscillations of SFS ring devices.

Chapter 5

Mesoscopic Lateral Spin Valve Structures

In this chapter we present our measurements of ferromagnet–superconductor–ferromagnet (FSF) devices in both the normal state of the superconductor and below the transition temperature. The measurements we report are magnetoresistance curves, resistance vs temperature, IV characteristics, and differential resistance curves for both "local" and "nonlocal" measurement configurations. We first review prior experimental work, then present our own results.

5.1 Prior Experimental Work

Since the first spin injection experiment of Johnson and Silsbee [14] discussed in Chapter 2.2, many research groups have investigated spin injection and detection in diverse lateral geometries, using a variety of materials and interfaces [62]. We will not review here the experiments done in ferromagnet–normal metal structures; they all detect spin accumulation using nonlocal magnetoresistance curves similar to the one in Figure 2.4 [19; 62; 63]. Instead, we will focus on two spin injection experiments in superconducting lateral spin valves aimed at detecting signatures of crossed Andreev reflection (CAR).

The experiments of Beckmann et al. [3; 64] are very similar to the work we present in this chapter. In the first one [3] several Fe probes are placed on an Al superconducting wire at distances on the order of the superconducting coherence length (see Figure 5.1(a)). The overlap between the ferromagnetic probes and the Al wire is very small, about 20×50 nm, in order to avoid suppression of superconductivity. The contacts are metallic, and the transparency is high due to the shadow evaporation technique used when depositing the two metals.

The nonlocal measurements performed in these devices are illustrated in Figure 5.1(a): for current I_A injected into one ferromagnetic probe, the voltage U_B is detected across the interface with another probe, outside the current path. The nonlocal resistance is then defined as $R = U_B/I_A$. For each pair of contacts Beckmann et al. characterize the spin valve behavior in the normal state

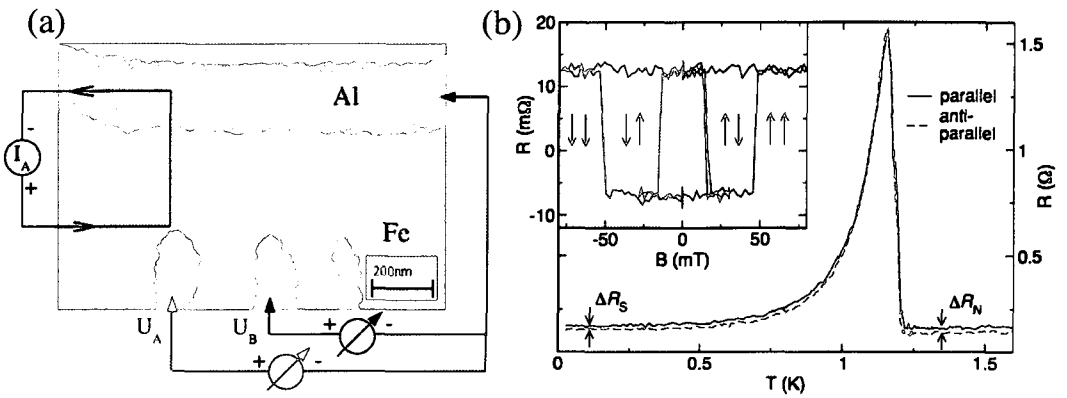

Figure 5.1 Nonlocal resistance measurement in a spin valve device by Beckmann et al. [3]. (a) SEM picture of one FSF device, with current injection and voltage detection configuration for one pair of probes. (b) Temperature dependence of the nonlocal resistance for parallel and antiparallel alignment of the magnetization of the two ferromagnetic probes.

of the aluminum wire; this is shown in the inset of Figure 5.1(b). For a pair of contacts separated by 210 nm, the nonlocal parallel resistance has a value of 13 mΩ, while the resistance for the antiparallel configuration is −8 mΩ. The arrows indicate the four different magnetization states.

For each of the four magnetization states the device is cooled below the superconducting transition temperature of aluminum. The temperature dependence of the nonlocal resistance is shown in Figure 5.1(b). The central result of Beckmann et al. in their first report of nonlocal measurements in FSF structures is the difference between the nonlocal resistance for parallel and antiparallel magnetization alignment in the superconducting state. This behavior is interpreted as evidence for the superposition of EC and CAR transport processes; EC is favorable for the parallel magnetization alignment, while CAR is favorable for the antiparallel one. The lower resistance of the antiparallel state compared to the parallel one is interpreted to be consistent with CAR: when current enters the superconductor from one lead, the voltage read on the other lead is negative if CAR takes place, thus decreasing the positive voltage drop due to EC.

Figure 5.2 shows the decay of the difference in resistance between parallel and antiparallel alignment as the separation between the injector and detector increases. The difference in the normal state is due to spin accumulation in the aluminum bar, while the difference in the superconducting state is assumed by the authors to come from subgap transport processes. The plot shows that the decay in the superconducting state occurs on a much shorter length scale than in the normal state, indicating different transport mechanisms. The decay length scale in the superconducting state is on the order of the aluminum coherence length.

In summary, the experiment shows behavior consistent with EC and CAR transport processes:

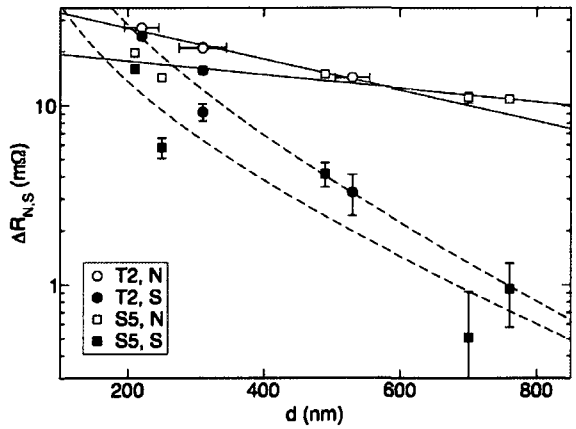

Figure 5.2 Difference in resistance between parallel and antiparallel alignment versus the distance between the contacts in the normal state of aluminum (open symbols) and in the superconducting state (closed symbols). Samples of two different layouts were investigated: layout T2, with three iron wires, and layout S5, with six iron wires. Reproduced from [3].

the resistance value depends on the relative orientation of the injector and detector magnetization, and the resistance difference between parallel and antiparallel states decays on a length scale of the superconducting coherence length as the separation between the ferromagnetic probes is increased. However, the predicted signature of CAR transport is a negative value for the superconducting nonlocal resistance in the antiparallel configuration, and that is not measured in this experiment.

A second experimental investigation [64] by the same authors reports negative resistance in the IV characteristic of an FSF device at small bias currents. The samples used in this study consist of two ferromagnetic leads forming tunnel contacts to the aluminum bar. An SEM picture of one of the three samples measured is shown in Figure 5.3(a). Contact A is the injector, and contact B is used to measure voltage relative to the drain. The measurements reported in this paper are not truly nonlocal, as seen in the current-voltage schematic circuit superimposed on the SEM image. However, the voltage drop V_B along the aluminum bar is zero in the superconducting state if nonlocal Andreev processes do not contribute to transport.

Figure 5.3(b) shows the temperature dependence of the detector voltage: as the device is cooled below $T_c \sim 1.35$ K, the small nonlocal signal decreases monotonically, reaches zero at 0.8 K, and becomes negative for both magnetization alignments. The reported negative resistance that is considered to provide unambiguous evidence for crossed Andreev reflection appears in both parallel and antiparallel alignments. As explained in the theoretical introduction (Chapter 3.3), the calculations for nonlocal conductance due to CAR and EC predict that EC is the dominant contribution for parallel alignment. Therefore, the measured resistance simply being negative is not sufficient to

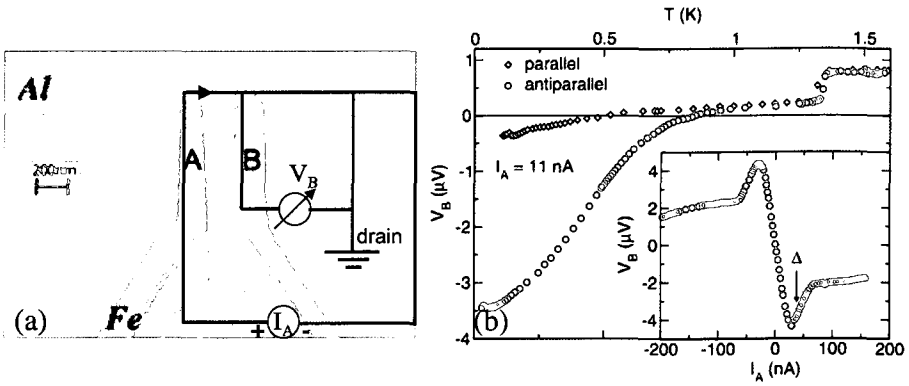

Figure 5.3 (a) SEM image of the contact region of the device, with added schematic of the measurement configuration: current is injected through contact A; the voltage measured at contact B is referenced to the drain contact, about 10 μm away, where the chemical potential of the superconductor can be considered in equilibrium. (b) Detector voltage V_B as a function of temperature for parallel alignment (blue diamonds) and antiparallel alignment (red circles). Inset: Nonlocal IV characteristic in the antiparallel alignment at 25 mK. Δ marks the value of the injecting current that corresponds to the energy gap of the superconductor. Adapted from [64].

support the claim that the measured signal is due to CAR; it needs to be accompanied by the correct magnetization alignment. Other reasons for the observed negative signal should be considered, such as ground loops in the measurement circuit.

5.2 Experimental Results: Nonlocal Signals in Mesoscopic Spin Valve Structures

The devices in this chapter are fabricated using electron-beam lithography and a double-angle shadow evaporation technique to produce highly transparent contacts between the ferromagnet and the normal metal. Two 100–150 nm wide, 20 nm thick cobalt probes are first deposited through the suspended mask using thermal evaporation. Subsequently, an aluminum strip 300 nm wide and 60 nm thick is deposited from a different angle to slightly overlap with the tip of the ferromagnetic wires. The distance between the two metals varies between 100 – 250 nm. Details on the fabrication procedure can be found in Chapter 4.

We use two measurement configurations to characterize our spin valve devices in the temperature region above T_c; they are schematically depicted in Figure 5.4. The first one is the "conventional" spin valve geometry, in which current is injected from one ferromagnet into the other, and the signal is measured across the current flow path. The spin valve resistance R_{SV} measured this way has contributions from the bulk ferromagnetic wire, from the contact resistance between ferromagnetic tips and the normal metal, and from the normal metal part in between the ferromagnets.

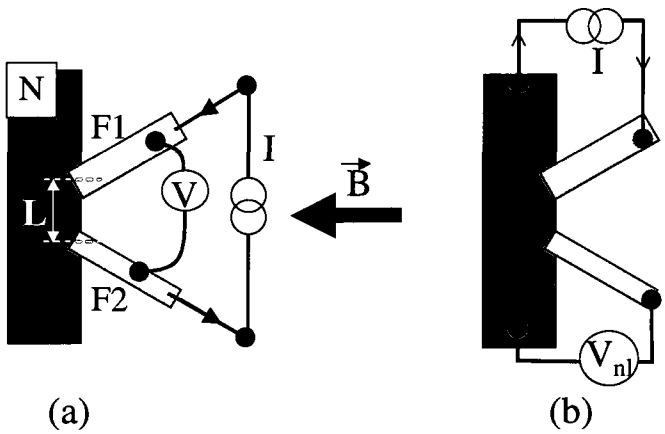

Figure 5.4 Current and voltage leads configuration, and magnetic field direction, for magnetoresistance measurements of FSF devices in the normal state of the superconductor. (a) Conventional spin valve geometry. (b) Nonlocal geometry. Gray wires are ferromagnets, blue ones are the normal metal/superconductor strip.

The other measurement configuration is the nonlocal spin valve technique, used to extract only spin current from the spin-polarized charge current. This is schematically depicted in Figure 5.4 (b). The nonlocal character of the measurement comes from the fact that the current and voltage circuits are separated; the measured voltage is due to diffusive transport of spins in the normal metal, with no accompanying charge current. If there are no spin effects, this nonlocal voltage should be zero.

5.2.1 Spin Injection and Accumulation in Lateral Spin Valve Devices in the Normal State

The purpose of the measurements presented in this section is twofold: first, we want to demonstrate that spin injection and detection is possible in our mesoscopic spin valve devices, and extract the value of the spin diffusion length in the normal metal, and the average polarization of the ferromagnetic electrodes. Secondly, we want to align the magnetization of the two probes parallel or antiparallel in order to look for signatures of EC/CAR processes in the superconducting state.

The magnetoresistance curves for our devices at 1.8 K in the conventional spin valve measurement configuration are taken by sending an ac bias current of 10 μA from one of the probes into the other probe, and measuring the voltage across the two probes, as shown in Figure 5.5(a). The curves show resistance changes when the magnetization of the probes rotates and changes direction as a function of an applied field. For each wire, the magnetization reversal can be decomposed in two parts: a reversible rotation part, and an irreversible jump which occurs at the coercive field of the wire.

The transverse dimension of our cobalt wires is much smaller than the longitudinal one (aspect

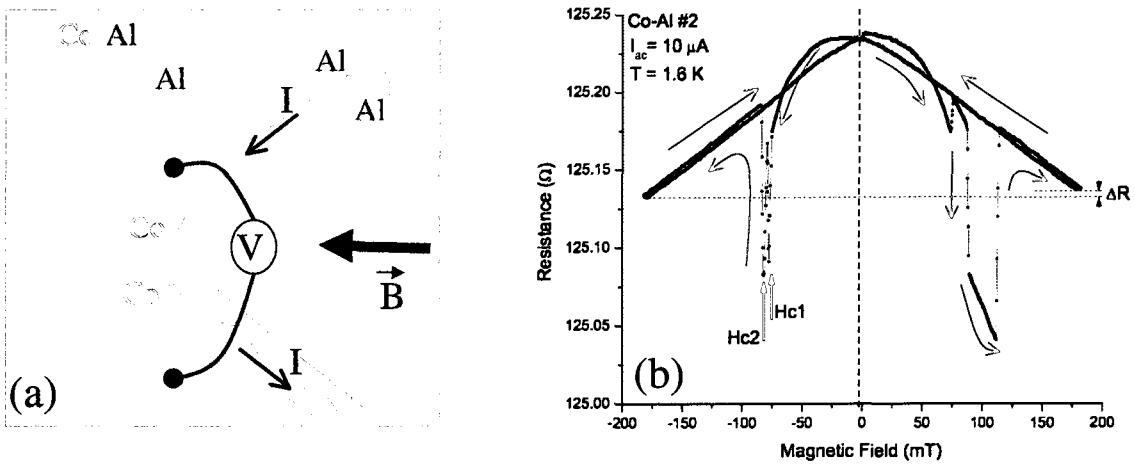

Figure 5.5 Magnetoresistance measurements in conventional configuration of a lateral spin valve device (a) SEM picture of a FSF device, and schematic of current injection and voltage detection setup (b) Typical AMR curve for our devices, taken at 1.6 K. The resistance jumps correspond to magnetization reversal of the ferromagnetic probes. Red arrows indicate the field sweep direction: from zero to saturation value, or from saturation value down to zero.

ratios 16–20), so we expect the magnetization to lie parallel to the wire axis. The external magnetic field is parallel to the plane of the ferromagnetic probes, and makes an angle of 30° to the easy axis of the probes due to their angled design. The magnetization is therefore always at an angle with respect to the applied field, which is evidenced by the downward slope of the curve as the field is increased.

There are also a few degrees of misalignment due to the coarse adjustment of the chip on the sample holder, resulting in a slightly different angle between the applied field and each of the ferromagnetic probes. This is evidenced by the small resistance difference ΔR (see Figure 5.5(b)) at positive and negative saturation field values.

Another point to note in the magnetoresistance curve in Figure 5.5(b) is the fact that the positive and negative coercive field values for the injector are different: the magnitude of the negative value (−77 mT) is slightly higher than that of the positive one (+73 mT). The magnetization reversal is therefore slower in the negative direction, which means that it takes more energy to set the probe in this magnetic configuration.

The last feature of interest is the broad switching of the detector probe on the positive field sweep. This is a typical feature when magnetization reversal occurs through nucleation and growth of reverse domains. Defects and impurities in the ferromagnetic film serve as nucleation sites for reversed-magnetization domains. Also, some samples may have residual reverse domains due to incomplete saturation. In addition to these reasons for the presence of domains in our ferromagnets, we

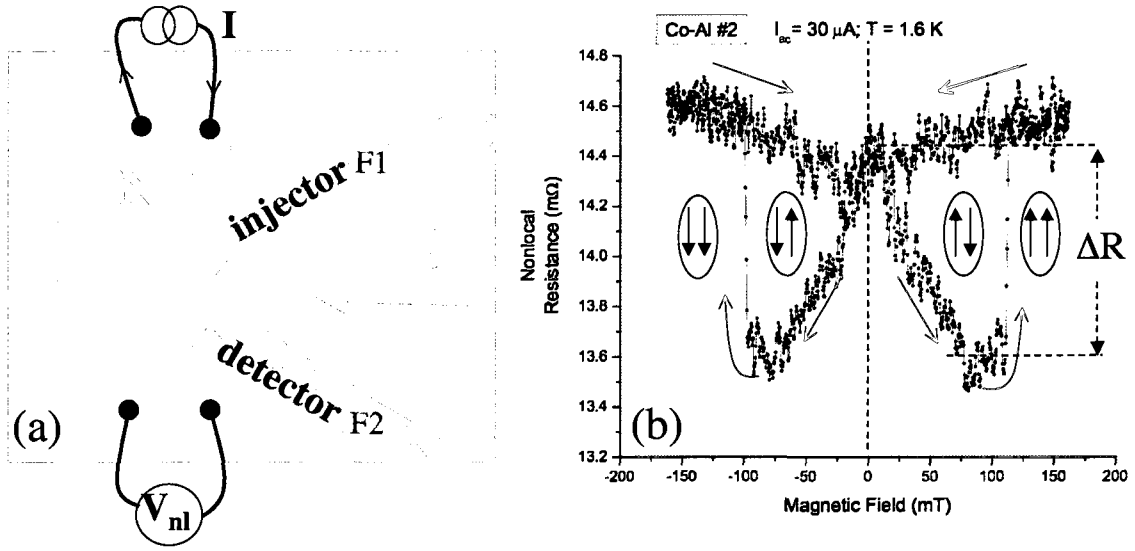

Figure 5.6 Magnetoresistance measurements in the nonlocal measurement configuration (a) SEM image of a lateral spin valve device, showing also the current injection and voltage detection scheme. (b) Nonlocal spin signal at $T = 1.6$ K as a function of the magnetic field applied parallel to the plane of the wires, and perpendicular to the interface. The black arrows label the four magnetization states; the red arrows indicate the sweep up or sweep down of the magnetic field.

have to take into consideration the fact that hexagonal cobalt has strong axial magneto-crystalline anisotropy, which favors a direction of spontaneous magnetization parallel to the -axis. This competes with the demagnetizing field in determining the magnetization configuration. Depending on the transverse dimensions of the wire, it is possible for the -axis to align either parallel or perpendicular to the wire axis [65].

We use the conventional spin valve measurement to confirm the switching of the cobalt probes, but the formation of domains in the ferromagnet and the strong AMR signal make it difficult to set the probes in an antiparallel magnetization state for further characterizing the device in the superconducting state. To eliminate these spurious physical effects, we measure the spin signal in the nonlocal configuration.

Figure 5.6(a) shows the nonlocal resistance measurement for one of our spin valve devices with a probe separation of 100 nm. The measurements were performed using an AC-resistance bridge by sending an AC-current $I = 30$ μA into the injector probe $F1$, and measuring the output AC voltage at the detector $F2$. The detected voltage V_d (equation 2.12) is proportional to the injected spin-polarized current and the polarization of the two electrodes, i.e., $V_d \propto P_1 P_2 I_e$. The sign of V_d depends on the relative magnetization configuration of the two ferromagnetic probes. The ratio of the measured nonlocal voltage to the injected current is called the nonlocal, or spin, resistance R_S.

Figure 5.6(b) shows the field dependence of the nonlocal resistance measured at 1.6 K. The

"up" and "down" magnetization states are defined as magnetization pointing along the wire either toward the interface or away from it, respectively. Also, we will label the relative magnetization alignments of $F1$ and $F2$ as parallel (P) and antiparallel (AP), as they are commonly referred to in the literature, even though the magnetization of the two ferromagnets in our FSF devices is never truly parallel due to the angled design of the probes.

Magnetic behavior is investigated in the following way: first, the magnetization of the ferromagnetic probes is saturated by applying a negative field of several hundred mT in the negative direction. At this point, the injector and detector magnetizations become saturated, and point along the easy axis of the wire, in the direction opposite to the interface. This is the P alignment state of the FSF device; it remains stable as the field is ramped down to zero. When the field is then increased in the positive direction, we observe a "switch" in the resistance at the positive coercive field of the injector (i.e., the wider ferromagnetic probe). Its magnetization reverses at this point and aligns with the new field direction. This is the AP state of the device, with an R_S value lower than that of the parallel state, as explained in Chapter 2.2. If we increase the field further, past the coercive field value of the detector, we notice another switch: the detector magnetization reverses, and the two wires have parallel magnetization once again, this time pointing towards the interface. The alignment will remain unchanged as the field is decreased to zero, and will change again at the negative coercive field of the injector when the external magnetic field is swept in the negative direction.

There are several features of note in the magnetoresistance curve in Figure 5.6(b). First, we note that even though the AMR contribution is absent in the nonlocal measurement, there is still a slope in the measured resistance as the field is increased from zero. Examining Figure 2.4 helps spot the difference very quickly: in the ideal nonlocal geometry, the parallel state resistance is flat up to the point where the switch occurs.

The reason for the different behavior in our devices comes from the angled geometry of the F probes. The electrons enter the N wire polarized at an angle θ with respect to the $\hat{y}$ axis (see Figure 5.6(a)). Let the injected magnetization in zero field be $\delta M\hat{r}$, with $\hat{r}$ at an angle θ from $\hat{y}$. The magnetization projection in the $\hat{x}$-$\hat{y}$ plane is then:

$$\delta M\ \hat{r} = \delta M \sin\theta\ \hat{x} + \delta M \cos\theta\ \hat{y}\ . \tag{5.1}$$

When an external field $\vec{B}$ is applied parallel to the $\hat{y}$ axis, δM will precess about this axis with a cone of semi-angle θ. Therefore, the gradual decrease of the nonlocal resistance in Figure 5.6(b)

is due to the precession of δM.

As the field is increased, the precession destroys the component of magnetization perpendicular to the field (i.e., $\delta M \sin\theta\ \hat{x}$), if $\gamma B T_2 > 1$, where γ is the gyromagnetic ratio, and T_2 is the spin relaxation time; this is the same physics as the Hanle effect used to measure T_2. At $x = L$ the detector measures a voltage proportional to the projection of the unaffected magnetization on the detector axis: $(\delta M \cos\theta)\cos\theta$. In our devices $\theta = 30°$, so in a high external field we detect only 75% of the magnetization injected in the normal metal compared to the usual spin valve design in which the F probes are parallel with respect to each other, and the field is applied parallel to them.

A final point to note about the shape of the nonlocal magnetoresistance curve is that the signal detected at large fields ($\sim$ 150 mT in Figure 5.6(b)) is higher than the one at zero magnetic field. This is easy to understand after the analysis above: at $B = 0$, the nonlocal voltage detected by probe $F2$ is proportional to the projection of the injected magnetization onto the detector axis, $\delta M \cos 2\theta = 0.5\ \delta M$. After precession and at high fields, $V_d \sim \delta M \cos^2\theta = 0.75\ \delta M$.

A more significant effect that our device geometry has on the detection of spin accumulation is related to the magnitude of the P and AP magnetization states. As explained in Chapter 2.2, the magnitude of the detector voltage for the two configurations should be the same, but positive for P alignment, and negative for the AP one. The offset that we see is referred to as the "baseline resistance" $R_B = (R_P + R_{AP})/2$; the ideal geometry should give $R_B = 0$. The magnitude of the observed experimental offset in Figure 5.6(b) is 14 mΩ. The correct interpretation of spin accumulation in our spin valve devices requires an understanding of the spurious contributions to the baseline resistance, and we will discuss this problem below.

The spin diffusion in the normal metal can be treated as taking place in a one-dimensional transport channel if the thickness d and the width w of the normal metal strip is much smaller than the spin diffusion length δ_s. In this approximation spin current is injected symmetrically to the left and to the right of the interface, and also uniformly over the width of the wire. In most experiments this is satisfied if the interface resistance is much larger than the sheet resistance of both $F1$ and N (in addition to d, $w \ll \delta_s$). However, deviations from the ideal geometry may create nonuniform injection along the $F1/N$ interface.

The effect of the probe configuration and interface characteristics on the spin accumulation in lateral spin valve structures has been discussed by Johnson et al. [66]. Figure 5.7 is a schematic depiction of the injection process in the two cases of uniform and non-uniform injection. If injection is uniform along the $F1/N$ interface (panel (a)), carriers will diffuse equally in both positive and

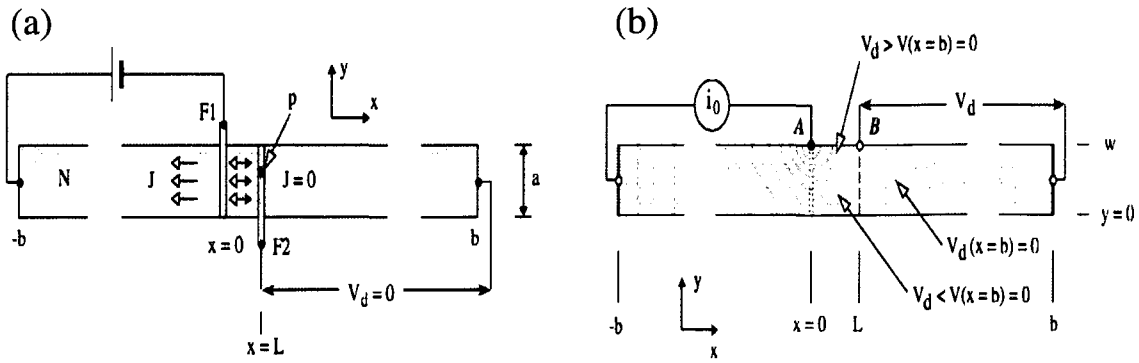

Figure 5.7 Schematic view of spin injection and detection in lateral spin valve devices. (a) Uniform injection to the left and to the right of $F1$. (b) Nonuniform injection. Current i_0 is injected at point A on the injector interface, and detection occurs at point B. Gray lines represent equipotentials. From [66].

negative x directions. An electric field will develop in the $x > 0$ region within a few mean free paths l_e of $x = 0$; this will generate a flow of carriers (depicted with open arrowheads) that will cancel the drift current in this region (black arrowheads). The result is zero net current to the right of the interface. Uniform injection should occur if the interface resistance is much larger than the sheet resistance of both injector and normal metal (e.g., the case of tunnel barrier contacts).

Nonuniform injection (panel (b)) may occur when the interface is highly transparent, and if the sheet resistance of the ferromagnet is higher than that of the normal metal. As a consequence of this, almost all spin-polarized current will be injected in the vicinity of the bottom edge of the F/N interface in a device with full overlap between the F and N wires. In our devices, the partial overlap between F and N is an obvious cause for nonuniform injection. Figure 5.7(b) shows sketched equipotential lines for current injected at point A. Near the injection point the equipotential lines are concentric circles due to radial current flow. Far from the injector in the region $x < 0$, the equipotential lines are vertical and evenly spaced due to uniform current density. In the region $0 < x < w$, the electric field developed to cancel the flow of carriers will deflect the current flowing upstream; the deflected carriers return downstream towards ground at $x = -b$ along the bottom edge of the wire. If the detector is within a distance comparable to w, then the electric field present in this region will cause a nonzero resistance.

The ratio of the sheet resistance of the F metal to the one of the N metal is quite large in our devices $\rho_{\square}^{(F)}/\rho_{\square}^{(N)} = 20.23$ ($\rho_{\square}^{(F)} = 8.7\ \Omega$, and $\rho_{\square}^{(N)} = 0.43\ \Omega$), satisfying the prerequisite for which Johnson's model is applicable. We can therefore use Johnson's analytical expression to calculate the baseline resistance in our devices:

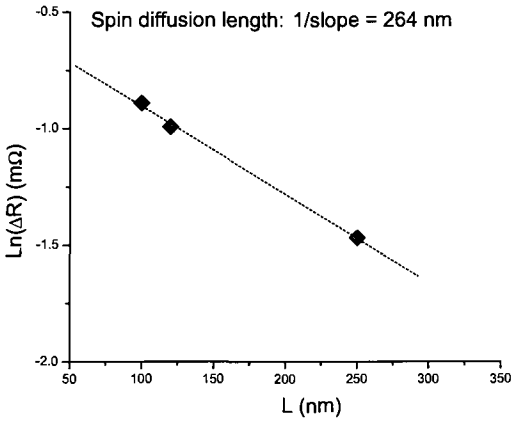

Figure 5.8 Semilog plot of nonlocal spin signal decay as a function of the ferromagnetic probe separation at 1.8 K. Dashed line is the best fit to equation 5.3.

$$R_B = \rho_{\square}^{(N)} \sum_{n=1}^{\infty} (\pm 1)^n \frac{1}{\pi n} e^{-n\pi L/w} \quad , \tag{5.2}$$

where L is the probe separation, w is the width of N, and the $\pm$ sign is a consequence of the placement of detectors on alternate sides of the normal wire. For the device measured in Figure 5.6, $L/w = 0.33$, and the above equation gives $R_B = 59$ mΩ for $n = 1 \ldots 6$. This value is much larger than what we observe. One reason for this discrepancy could be the non-unifom thickness of the N wire: due to the shadow evaporation method, the normal metal film edges taper to zero in the contact region, affecting the current density uniformity at the injection point.

The spin-related resistance R_S decays with L, the separation between injector and detector, so we can extract the spin diffusion length of electrons in aluminum by doing measurements of R_S for different probe separation. The magnitude of spin signal $\Delta R = 2R_S$ is given by:

$$\Delta R = P^2 \frac{\delta_s}{\sigma_{Al} A} e^{-L/\delta_s} \quad , \tag{5.3}$$

where P is the geometric mean of the polarization of the ferromagnetic probes ($P = \sqrt{P_1 P_2}$), and σ_{Al} and A are respectively the conductivity and cross-sectional area of the aluminum wire. The measured decay of ΔR as a function of L is plotted in Figure 5.8. By fitting our data to Equation 5.3 we obtain $\delta_s = 264$ nm in the aluminum strip at $T = 1.8$ K. Using this value we calculate $P = 9.3$ %.

The spin signal $\Delta R = R_S^{\uparrow\uparrow} - R_S^{\uparrow\downarrow} \sim 1$ mΩ (see Figure 5.6(b)) in our devices is much smaller than the values obtained by other research groups [3; 19; 67]; the largest value reported to date is in the

devices measured by Valenzuela et al. ([67]): the spin resistance was as high as 2.5 Ω at 4.2 K, for thicknesses of the aluminum film between 6–10 nm. There are many reasons for which our spin signal is small, including angled probe geometry, high AC measurement currents, a thick normal metal wire, and decrease of spin polarization for highly transparent barriers. All of these parameters can be easily changed to increase the spin accumulation. However, our study is not concerned with the optimization of spin injection and detection. The best parameters for increasing the spin signal (very thin normal metal wires, tunnel contacts between F and N, etc) do not create the best conditions for the investigation we are interested in, i.e., CAR transport in the superconducting state.

5.2.2 Spin-dependent Transport in the Superconducting State of Lateral Spin Valve Devices

In order to look for CAR and EC effects in our devices, we cool the sample below the transition temperature of the superconductor. The antiparallel magnetization state is set by doing a magnetic field sweep in the nonlocal current–voltage configuration. The procedure is shown in Figure 5.9(a) by the green curve. The magnetization configuration of the spin valve at the beginning of this procedure is down-down. We start by sweeping the field in the positive direction up to the value of the coercive field of the injector; when the injector magnetization switches parallel to the applied field, we stop the sweep and ramp the field down to zero. At this point the detector's magnetization is opposite to the field direction, so the magnetization state of the spin valve is antiparallel. As it can be seen in the green plot, the value of the resistance does not change as the magnetic field is decreased, confirming that the magnetization state is stable at zero field.

Once the state is set to the desired configuration, the external field is kept at zero during sample cooling, as well as at base temperature. As we lower the temperature, we monitor the change in the resistance of our devices. Figure 5.9(b) shows the temperature dependence of the nonlocal resistance for sample FSF-2. This signal is measured using a low ac excitation current of 300 nA to avoid heating of the device and quasiparticle injection above the superconducting gap. At this excitation current, the nonlocal signal in the normal state is 26 mΩ.

Right below the superconducting critical temperature $T_c = 1.4$ K the nonlocal resistance goes steeply up to a value that is two orders of magnitude larger than the normal state value. As the temperature is lowered further, the peak decays, and the nonlocal signal saturates to its low-temperature value at $T \sim T_c/2$. The nonlocal signal at 10 mK is $\sim$ 40 mΩ, which represents an increase of 54% over the normal state value.

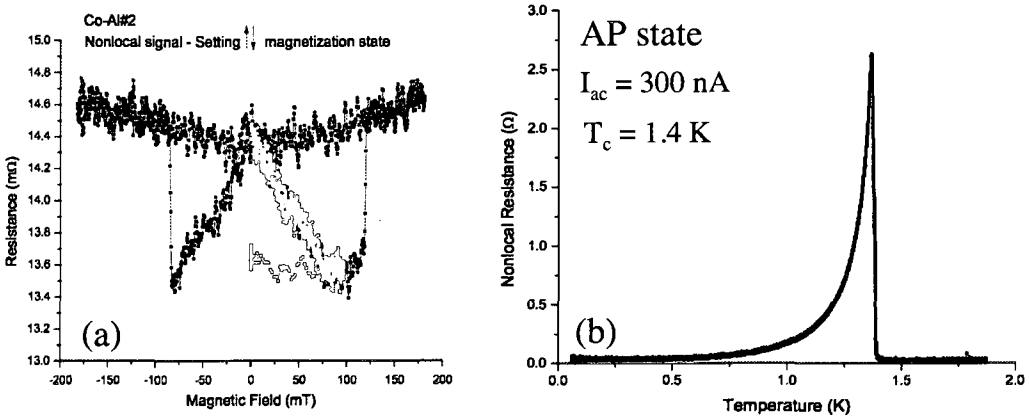

Figure 5.9 (a) Setting the antiparallel magnetization configuration of the two ferromagnetic probes. After doing a full field sweep, shown in black, we start the green sweep in the down-down configuration. (b) Temperature dependence of the nonlocal resistance in the antiparallel alignment of the injector and detector magnetizations. The signal is dominated by the charge imbalance peak, which subsides as the temperature is lowered. At the lowest temperature there is still a finite resistance, $R_S \sim 40$ mΩ. The separation between the ferromagnetic tips is 100 nm.

The pronounced peak right below T_c has been observed in other nonlocal NSN and FSF lateral spin valve structures, and is attributed to charge imbalance effects [3; 4]. We also interpret the rise in resistance right below T_c as due to charge imbalance, which is understood as follows: when current is sent across the F/S interface at T_c, where the superconducting energy gap is small, almost all excitations incident from the ferromagnet propagate into the superconductor, so a population imbalance of electron-like and hole-like excitations appears in the superconductor near the interface, and is detected as an additional voltage.

Golubev and Zaikin [68] argue that the peak occurs at the crossover of two competing processes: Andreev reflection and charge imbalance. Although they claim that their theoretical predictions qualitatively match the experimental results, the resistance peak they predict appears at a temperature $T^* \sim 0.3\ T_c$. They wrongly interpret the temperature scale in the plotted data of Cadden-Zimansky et al. [4] as being normalized to T_c, in which case the theoretical model would indeed match the experimental curve. In both experiments to date that report a peak in the nonlocal signal, the resistance starts increasing right below T_c, and this is what we also measure.

As the temperature is lowered further, the non-equilibrium charge subsides because a substantial fraction of quasiparticles are now Andreev reflected at the interface. At $T \sim T_c/2$ the charge imbalance has decayed considerably: virtually all quasiparticles are Andreev reflected, and no quasiparticle current flows in the superconductor.

We confirm that the peak appears at the temperature corresponding to T_c by recording the local

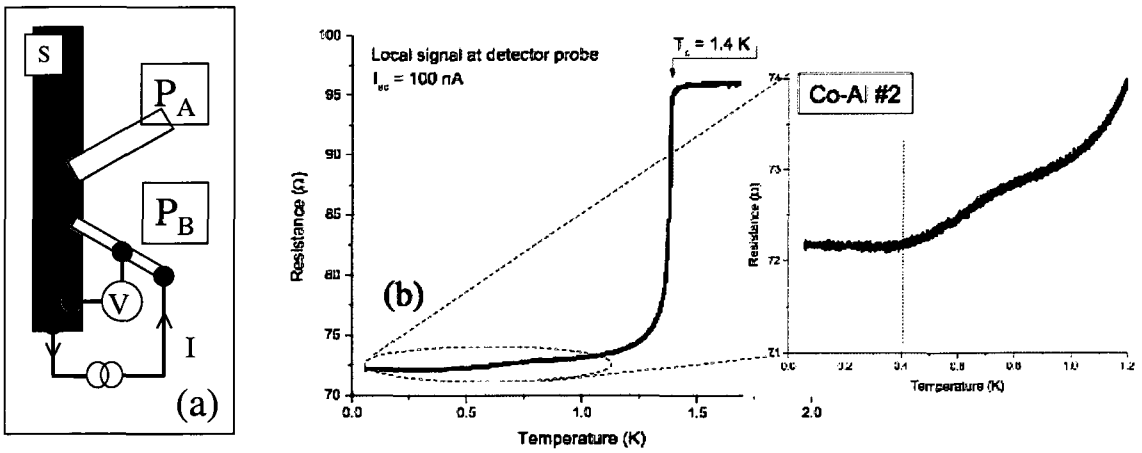

Figure 5.10 Temperature dependence of the local resistance at the detector probe. (a) Current injection and voltage detection scheme. (b) Local resistance behavior as the temperature is lowered through the superconducting transition. The detail shows nonuniform decrease of the resistance below 0.8 K.

resistance of the detector contact as a function of temperature; this is shown in Figure 5.10. A sharp drop in resistance of $\sim 20\ \Omega$ is observed at 1.4 K, so we identify this temperature with the T_c of our aluminum strip.

There are two important features worth noting in Figure 5.10. First, we do not see a charge imbalance peak in this local configuration of current injection and voltage detection. The distance between the FS contact and the voltage drain lead on the superconductor is large, $\sim$13 μm, so any non-equilibrium quasiparticle populations injected at the contact should have relaxed before they reach the drain location. Therefore the absence of the peak is to be expected. However, the nonlocal measurement, which has the same distance between injection point and drain leads, shows a very large charge imbalance signal.

Another interesting feature in the temperature dependence of the local resistance is represented by the non-monotonic behavior after the initial gradual decrease below T_c. As the temperature is lowered further, the slope of R vs. T changes at approximately 0.8 K. This second transition at 0.8 K may be the depressed transition of the Al wire in the vicinity of the ferromagnetic tip. Below this transition the curve shows another gradual decrease until $T = 0.4$ K; the resistance change during this step is 0.7 Ω, a drop of approximately 1%. At temperatures lower than 0.4 K the signal remains constant all the way to base temperature.

The IV characteristic at 10 mK in the nonlocal measurement configuration is plotted in Figure 5.11. As the current is increased through the injector, the voltage drop across the detector is negative at first; this results in a negative nonlocal resistance. When the bias current reaches 3

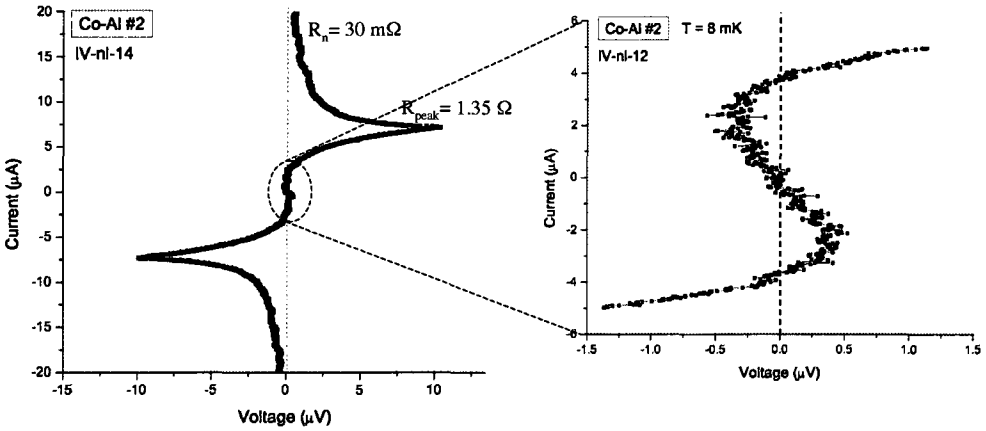

Figure 5.11 IV characteristic in the nonlocal measurement configuration. The detail shows a negative voltage as the bias current is increased.

μA, the nonlocal resistance becomes positive. This resistance turns negative again at ~ 6 μA. The sharp peak of this last transition has a resistance value of 1.35 Ω, which is 100 times higher than the zero-bias value. This peak in the IV is similar to the one in the R vs. T curve, so we attribute it to the transition of the superconductor to the normal state. After this transition the slope drops quickly to the value of the normal state nonlocal resistance, as measured in the magnetoresistance curves.

The slope of the IV at zero bias is surprisingly high: -200 mΩ. We do not seem to measure the same low-temperature value of the resistance in a dc-current injection setup, used to take the IV characteristic, as in the ac-configuration with a resistance bridge, used to record the R vs. T dependence. The 100 nA setting on our LR 750 resistance bridge has a (mid-scale) analog resolution of 16 mΩ, which is an order of magnitude smaller than the difference between the bridge reading and the IV slope. Therefore the discrepancy cannot be explained as due to a bridge offset, unless the instrument does not operate according to specs anymore.

If the excitations are sent across the interface at subgap energies, there are three possibilities for transport across the interface, as explained in Chapter 3.3: the incoming electron is Andreev reflected in the same ferromagnetic probe; it is reflected in the other probe as an electron of the same spin (EC process); or it is reflected as a hole of opposite spin in the other electrode (CAR process). The sign of the detected nonlocal voltage is negative only for the latter case; therefore, we interpret the signal measured as evidence for the realization of CAR transport.

In order to check that the negative signal we measure actually comes from subgap transport in the superconductor, and not from quasiparticles propagating above the gap, we have to determine

the value of the superconducting energy gap of our aluminum strip. For this purpose we use the additional voltage leads on the detector and superconductor to measure the local IV at the detector site. Since the measurement configuration includes the ferromagnet, the superconductor, and the interface, the purpose of the analysis below is to separate the contributions of each part to the measured signal.

Figure 5.12(a) shows schematically the additional leads that can be used to measure our FSF devices. Keeping the same current injection path PB1-S4, we measure the IV characteristics of the junction, of the interface, and of the length of ferromagnet between PB2 and PB3. From the IVs we calculate the dV/dI curves, which are plotted in Figure 5.12(b). All curves start at the same resistance value, and the ones that show a transition have a common bias current value of approximately 6 μA. This is exactly the bias current for which the nonlocal IV curve develops a large peak. We can be confident now that this is the transition of the superconductor around the contact region to the normal state, and therefore bias currents smaller than this value inject electrons below the superconducting gap.

The differential resistance for the detector and superconducting path PB3-S3, plotted as the blue curve in Figure 5.12(b), shows three peaks, corresponding to three superconducting regions along the path across which voltage is measured; each of these can turn normal at different bias currents. First, there is the large contact between the measurement lead PB3, which is a superconducting lead, and the ferromagnetic probe; we expect a weak link at this location. Another region of depressed superconductivity is the interface between the aluminum strip and the ferromagnetic probe. The last region that would change from superconducting to normal state is the part of the aluminum strip enclosed by the voltage probes; we expect this part to transition at the highest current density compared to the other three regions, so we attribute the third peak to this transition.

The differential resistance of the interface is shown in Figure 5.12(b) as the red curve. The behavior with increasing bias current is quite interesting: for $I_{\text{bias}} \sim 6$ μA, we observe a sharp transition to a lower resistance state before the normal state resistance of the structure is reached. This interface behavior has been observed by other groups in samples where the interface resistance is smaller than the electrodes' resistance (e.g., Cadden-Zimansky in normal metal/superconductor cross geometry [4]) but no explanation has been given. We interpret this behavior in terms of spin accumulation at the interface. As the bias current is increased, spin accumulation in the ferromagnetic wire in the vicinity of the interface increases because of partial Andreev reflection in FS structures (see Chapter 3.2). This leads to an increase in the boundary resistance. When

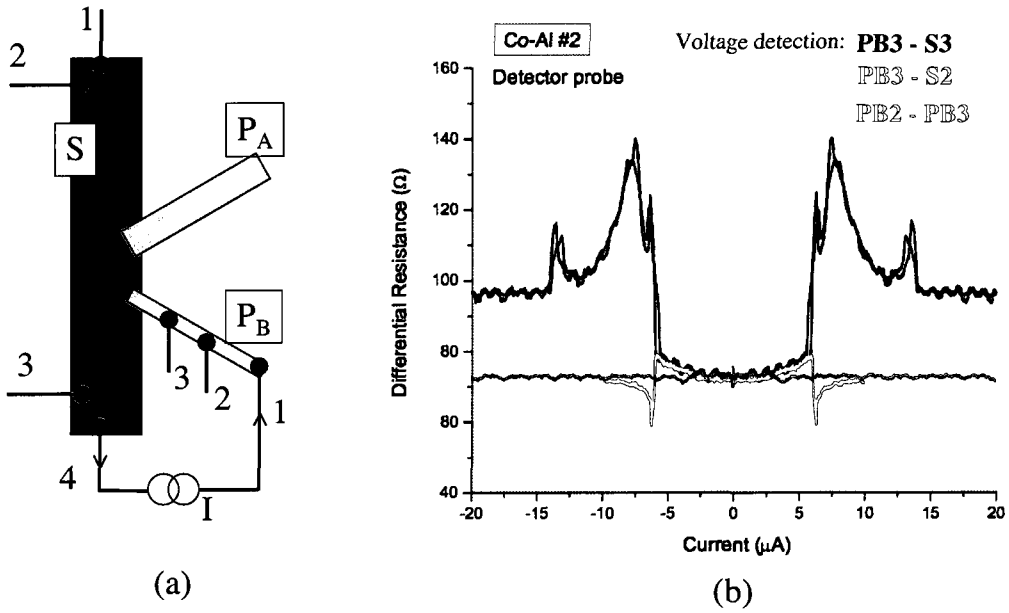

Figure 5.12 (a) Measurement leads for the spin valve device. (b) Calculated differential resistance curves from the IV characteristics measured at 10 mK. For a given current injection path, illustrated in (a), we measure the voltage drop across various parts of the device.

the potential on the ferromagnetic side of the interface is higher than the superconducting gap, significant spin current will enter the superconductor. This results in an abrupt reduction in the boundary resistance, as seen in the differential resistance curve. Further increase in the bias current leads to the transition of the superconducting part of the junction to the normal state.

All samples measured in this chapter were cooled below T_c first in the antiparallel magnetization alignment. None of them survived long enough to give data also in the parallel magnetization state; electrostatic discharge was the major cause of this misfortune. Therefore, not knowing whether the signal in the parallel magnetization configuration is similar in magnitude but opposite in sign to the one in the antiparallel state, we can not claim definite evidence for crossed Andreev reflection subgap transport.

5.3 Summary

We have demonstrated spin injection and detection in mesoscopic spin valves at 1.8 K. We found that spin accumulation is small ($\sim$ 1 mΩ), and spin diffusion length in the normal metal is 264 nm. In the superconducting state of aluminum we measured a negative nonlocal voltage in the antiparallel alignment of the magnetization of the two ferromagnetic probes. This is consistent with transport realized via crossed Andreev reflections. However, we were not able to perform similar

measurements in the parallel magnetization configuration; this would have been the ultimate test of whether the negative signal measured in the AP state is due to CAR or to spurious contributions from the measurement circuitry (e.g., ground loops, faulty wires).

Chapter 6

Double Superconductor /Ferromagnet/Superconductor Junctions

The motivation for studying the devices presented in this chapter comes from a dual interest in bringing together the physics of SFS junctions in the stacked geometry with that of lateral mesoscopic SFS structures, and in probing the coherence of crossed Andreev reflection.

This chapter is organized as follows: in the first section we review the theoretical prediction that led us to fabricate and measure the lateral double-junction device geometry, followed by the most relevant works, both experimental and theoretical, that may help us interpret our results. In the second section we present measurements on double superconductor/ferromagnet/superconductor (S–FF–S) junctions, followed by a discussion of possible explanations for the observed effects. We include a section of measurements on a single SF junction that can help interpret the data on S–FF–S structures.

6.1 Theoretical Predictions and Prior Experimental Work

The motivation for the device geometry mesured in this chapter comes from the theoretical prediction by Mélin [7] for a DC Josephson current due to fluctuations in the device illustrated in Figure 6.1. Supercurrent is not expected through a single ferromagnetic wire unless the wire length is much shorter than the exchange length. In the device proposed by Mélin, two ferromagnetic wires attached between two superconducting electrodes can carry supercurrent over distances longer than the exchange length ξ_h if their length is smaller than the electron phase coherence length l_ϕ. For supercurrent to occur, the ferromagnetic wires should be separated by a distance less than a superconducting coherence length, and their relative magnetization should be antiparallel. A previous calculation [69] shows that the crossed Josephson current vanishes on average in the diffusive limit because the incoming electron and the Andreev reflected hole encounter a different sequence of impurities in the two electrodes. However, Mélin's calculation shows that the statistical fluctuations of the crossed Josephson current are not zero. The fluctuations considered here are due to disorder

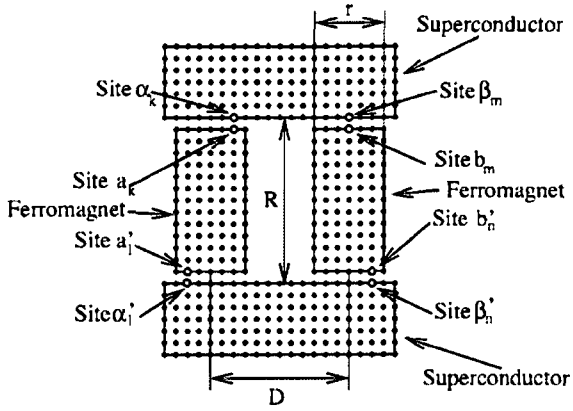

Figure 6.1 Schematic representation of the double junction device. Reproduced from [7].

scattering at impurity sites at the interface.

Mélin's calculation is done in the limit of tunnel coupling between the ferromagnets and superconductors. The tunnel supercurrent in the geometry considered here is the result of the emission of a correlated pair of electrons from the top superconductor by Andreev reflection, followed by the absorption of the pair at the bottom superconductor, also by an Andreev reflection process. These two Andreev reflections can be local or nonlocal, that is, the incoming electron and outgoing hole can propagate in the same or different electrodes.

The calculated local supercurrent $I_S^{\rm loc}$ that results from Cooper pairs propagating in a single junction is proportional to the number of channels $N_{\rm ch}$ at a single interface:

$$I_S^{\rm loc} \sim \frac{N_{\rm ch}}{\sqrt{(1/\xi_h)^2 + \ _h^2}} \ , \tag{6.1}$$

where $_h$ is the wave vector of the supercurrent oscillations, and ξ_h is the exchange length.

The average of the nonlocal supercurrent $I_S^{\rm nonloc}$ vanishes in a diffusive system due to disorder averaging over the elastic mean free path l_d. However, the variance of $I_S^{\rm nonloc}$ is given by:

$$\begin{aligned}\overline{(I_S^{\rm nonloc})^2} = 4\pi^2(e/h)^2\Delta^2 \left|t_{a,\alpha}\right|^4 \left|t_{b,\beta}\right|^4 N_{\rm ch}^2 \overline{f_{\alpha,\beta}^2}\ \overline{f_{\alpha',\beta'}^2} \left(\frac{(\pi\rho_S)^2 l_\varphi}{(k_F a_0)^2 l_d}\right)^2 \\ \times \left\{\exp\left(-\frac{2R}{l_\varphi}\right) + \frac{1}{1+\sqrt{1+[l_\varphi(k^\uparrow - k^\downarrow)]^2}} \exp\left(-\frac{2R}{\xi_h}\right)\right\} \sin^2\varphi \ ,\end{aligned} \tag{6.2}$$

where φ is the phase difference between the two superconductors, l_φ is the phase coherence length in the ferromagnet, and $k^\uparrow$ and $k^\downarrow$ are the spin-up and spin-down Fermi wave vectors.

Equation 6.2 shows two contributions to the variance of $I_S^{\rm nonlocal}$: one that decays over l_φ (long-

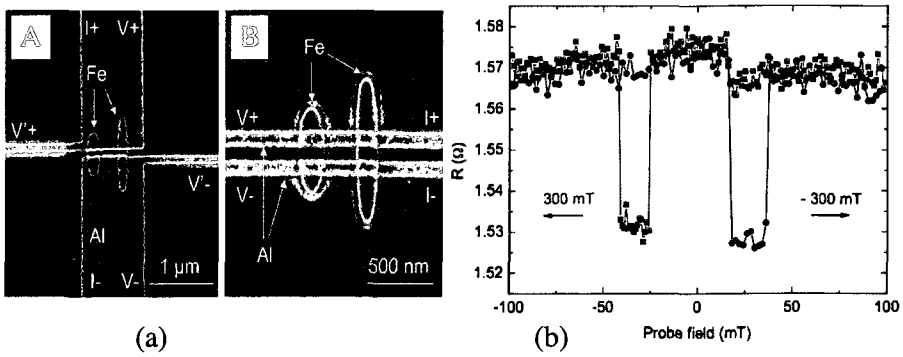

Figure 6.2 (a) SEM pictures of two double-junction device geometries: geometry A has voltage probes close to the interface, and the tips of the Fe ellipsoids overlap the wide Al pads; in geometry B there is no overlap at the ends of the ellipsoids, thus avoiding the stray fields' influence on the superconducting wires. (b) Resistance of a device in geometry type A at a series of values of probe magnetic fields. The curve is taken at 310 mK. Reproduced from [70].

range) and another one that decays over ξ_h. The information about propagation inside the superconductors is contained in $f_{\alpha,\beta}$, $f_{\alpha',\beta'}$ (locations $(\alpha,\ \ )$, $(\alpha',\ \ ')$ are illustrated in Figure 6.1). The average over disorder $\overline{f^2_{\alpha,\beta}}\ \overline{f^2_{\alpha',\beta'}}$ is proportional to $1/N_{\rm ch}$, so $\overline{(I_S^{\rm nonloc})^2}$ scales with the number of channels, i.e., is proportional to the square root of the junction area.

In summary, the calculation shows that while the local supercurrent decays over a distance set by the exchange length ξ_h, the nonlocal supercurrent due to fluctuations can persist over a longer distance given by the phase coherence length in the ferromagnet l_ϕ. This is the effect we are looking for in our experimental investigation.

Luo et al. [70] performed an experiment in the double F/S geometry proposed by Mélin. Their devices are not in the short junction limit that is predicted to carry supercurrent, so are quite different from our devices in terms of the roles that the different length scales may play.

Figure 6.2 shows the two sample geometries investigated by Luo et al. In both geometries two aluminum wires, 100 nm apart, are connected through two parallel ellipsoids with a separation varied between 100 – 500 nm. The ferromagnets are made of 49 nm-thick epitaxially grown iron, and are each designed with different dimensions (900 × 100 nm^2 and 500 × 100 nm^2) in order to achieve different coercivities. MFM imaging shows single magnetic domain configuration.

Luo et al.'s spin valve measurements on a sample in the geometry A are shown in Figure 6.2(b). The curve was obtained using a proble magnetic field method in order to avoid the AMR effects. The method works as follows: Just before the measurement, the magnetization of the two wires is saturated in a field of -300 mT. Then for every data point, a probe magnetic field of varying magnitude is applied for 1 second, then ramped back to zero, and the resistance value is measured.

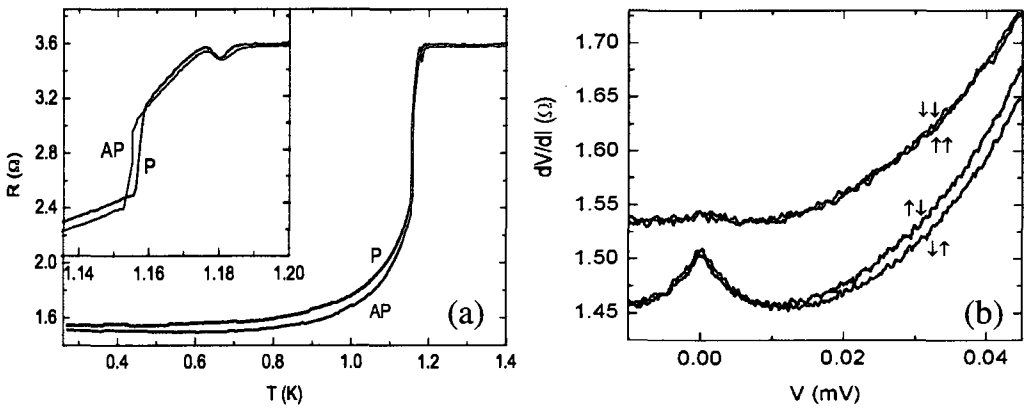

Figure 6.3 (a) Resistance versus temperature curves for parallel and antiparallel magnetization alignments for a device of geometry A. The inset shows detail of features at T_c. (b) Differential resistance curves as a function of voltage in the parallel (top curves) and antiparallel (bottom curves) magnetization alignments. Reproduced from [70].

The changes in the resistance correspond to magnetization reversal in the iron ellipsoids: the lower resistance state is the antiparallel (AP) relative magnetization configuration, while the high field resistance represents the parallel (P) configuration. The resistance difference between P and AP is ~ 40 mΩ.

Figure 6.3(a) shows the temperature dependence of the 2-wire resistance of sample A for both P and AP states as the device is cooled below T_c. The resistance depends on the relative magnetization alignment. The P state resistance is higher than that of the AP state for the entire temperature range, and the resistance difference between the two states has a non-monotonic behavior, showing a maximum at 0.9 K. The two sample geometries show the same temperature dependence, indicating that geometry A is not affected by the stray fields at the ellipsoids' ends.

Figure 6.3(b) shows transport measurements in the sub-gap regime at $T = 260$ mK. The differential resistance curve for the AP magnetic state has a zero-bias peak that is not present in the P state. Neither the behavior nor the magnitude of the measured signals change as the separation between the ellipsoids is increased beyond the superconducting coherence length $\xi_S \sim 100$ nm. This lack of change rules out an interpretation of the data in terms of CAR transport.

Authors conclude that the inverse proximity effect is responsible for the observed dependence of the signal on the relative magnetization alignment of the two ellipsoids: in the P state, the current flowing through both ferromagnetic wires injects the same majority spins, resulting in a significant spin accumulation in the superconductor in the vicinity of the interface; by contrast, in the AP state one ferromagnet injects spin-up quasiparticles, and the other one injects spin-down quasiparticles, which results in reduced spin accumulation in the superconductor, and therefore lower resistance.

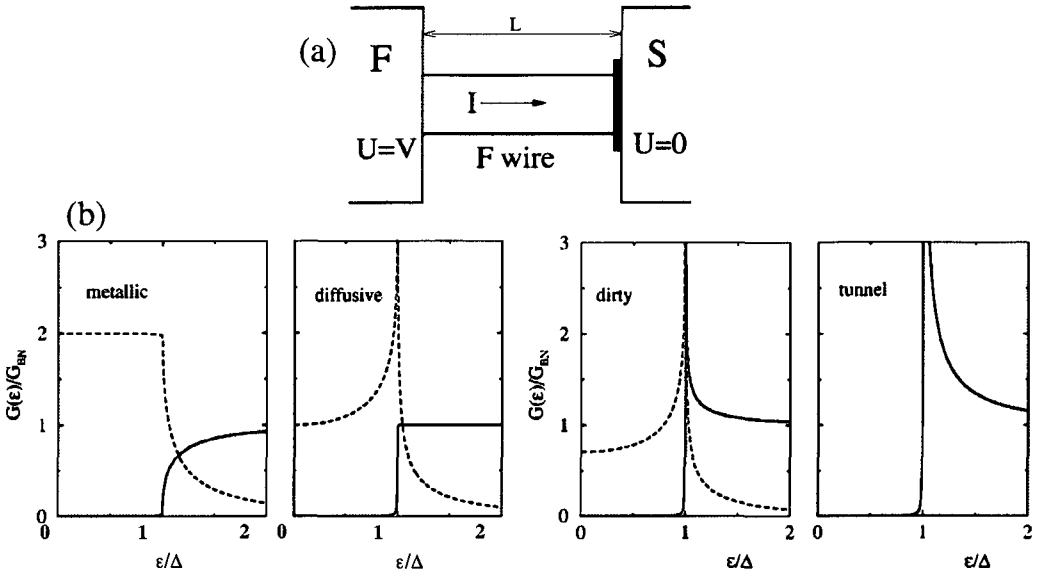

Figure 6.4 (a) Schematic depiction of the F/S structure modeled by Belzig et al.: a ferromagnetic wire connects a ferromagnetic reservoir held at voltage V and a grounded superconducting reservoir. (b) Spectral quasiparticle conductance G_{QP} (solid curves) and Andreev conductance G_A (dashed curves) for different types of contacts. Below the superconducting gap Δ only G_A is nonzero. Reproduced from [46].

In order to better understand the processes involved in the double F/S hybrid structures we will review the theoretical model of Belzig et al. [46] for a single F/S interface. The numerical simulations presented in this paper show behavior qualitatively similar to our data. The model applies to ferromagnets with exchange energy $h_{\mathrm{ex}} \gg \Delta$, which is the case in our structures formed by transition metal ferromagnet cobalt and the superconducting metal aluminum. In this regime the model considers the proximity effect in the ferromagnet to be negligible due to the strong decoherence of quasiparticles belonging to different spin bands. In this case all changes in the behavior of the F/S structure are induced by the interface itself. The authors model multiple interface morphologies, taking into account spin accumulation and heating effects in the ferromagnet.

Figure 6.4(a) shows the F/S structure considered by the authors. The contact between the ferromagnetic wire and the superconductor is described by a distribution of transmission eigenvalues which leads to contact-specific energy dependence of the quasiparticle conductance $G_{\mathrm{QP}}(\epsilon)$ and Andreev conductance $G_A(\epsilon)$.

The energy dependence of these spectral conductances is shown in Figure 6.4(b). The solid curve is $G_{\mathrm{QP}}(\epsilon)$, and the dashed curve is $G_{\mathrm{A}}(\epsilon)$. Below the superconducting gap only the Andreev conductance has a nonzero contribution, gradually decreasing from a value of 2 G_{BN} for the metallic contact to zero for the tunnel junction. Above the gap, the Andreev conductance decays as $1/\epsilon^2$,

and quasiparticle transport (and therefore spin transfer) into the superconductor becomes possible.

In general, the spin-dependent quasiparticle conductances $G^{\uparrow}_{\rm QP}(\epsilon)$ and $G^{\downarrow}_{\rm QP}(\epsilon)$ are of different magnitude and have different energy dependences. The authors assume that the energy dependence of each conductance is the same, so they only consider differences in magnitude (due to different numbers of transmission channels) for the two spin species.

The spin polarization of the boundary conductance is defined as

$$\gamma_{\rm B} = \frac{G_{\uparrow} - G_{\downarrow}}{G_{\uparrow} + G_{\downarrow}} \ , \tag{6.3}$$

where $G_{\uparrow} + G_{\downarrow}$ represents the total conductance of the boundary. The boundary polarization γ_B is assumed to be different from the polarization of the bulk ferromagnetic wire, γ.

The resistance of the ferromagnetic side of the wire in the normal state is

$$R_{\rm FN} = R_{\rm F} + R_{\rm BN} + R_{\rm sf}\frac{(\gamma - \gamma_{\rm B})^2}{1 + R_{\rm sf}/R_{\rm BN}} \ , \tag{6.4}$$

where $R_{\rm F}$ is the resistance of the bulk ferromagnetic wire, and $R_{\rm BN}$ is the normal state resistance of the contact. The last term represents the excess resistance due to spin accumulation in the ferromagnetic wire; we note that the excess resistance increases as the difference between γ and $\gamma_{\rm B}$ increases. The spin flip resistance is given by

$$R_{\rm sf} = \frac{R_{\rm F} l_{\rm sf}}{L} \tanh\left(\frac{l_{\rm sf}}{L}\right)(1 - \gamma^2) \ , \tag{6.5}$$

where $l_{\rm sf}$ is the spin flip length in the ferromagnet and L is the length of the wire (see Figure 6.4a). The resistance change between the superconducting and normal state is:

$$\Delta R_{\rm FS}(T) = R_{\rm FS}(T) - R_{\rm FN} \ . \tag{6.6}$$

With these definitions, the temperature dependence of the boundary resistance is calculated for different current polarizations $\gamma_{\rm B}$ and γ in three cases: elastic scattering, inelastic scattering in linear response, and inelastic scattering in nonlinear response.

We first review the case of elastic scattering in the ferromagnetic wire. The resistance change for $\gamma^2 \ll 1$ (and vanishing boundary polarization $\gamma_{\rm B} \approx 0$) is given by:

$$\Delta R_{\rm FS} = \left\langle \frac{1}{G_{\rm QP}(\epsilon) + G_{\rm A}(\epsilon)} \right\rangle - R_{\rm BN} + \gamma^2 \left[\left\langle \frac{1}{G_{\rm sf} + G_{\rm QP}(\epsilon)} \right\rangle - \frac{1}{G_{\rm sf} + G_{\rm BN}} \right] . \tag{6.7}$$

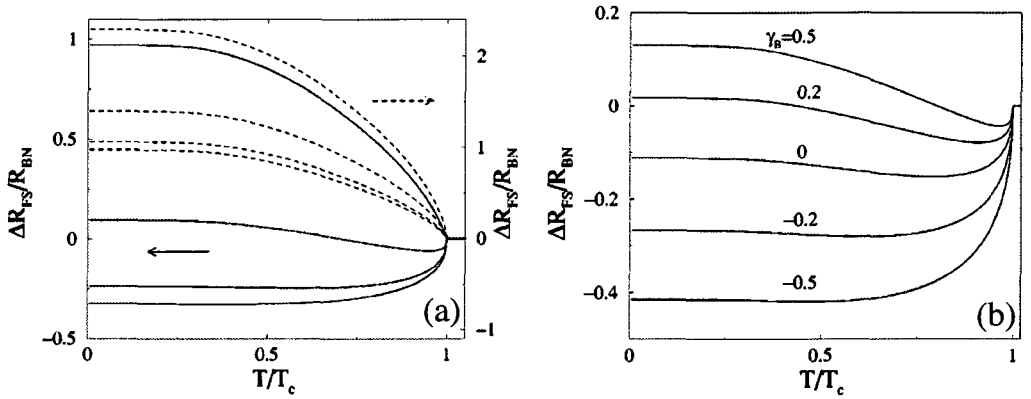

Figure 6.5 Temperature dependence of the resistance change of a ferromagnetic wire attached to a superconducting reservoir in two cases: (a) boundary polarization $\gamma_B = 0$ for two types of contacts: relatively transparent, $q = 0.75$ (solid curves), and less transparent, $q = 0.25$ (dashed curves). The polarization γ of the wire is changed from 0 to 0.6 in steps of 0.2 from the bottom curve to the top curve for each contact. (b) Several values of γ_B for a relatively transparent contact, $q = 0.75$. The wire polarization is $\gamma = 0.3$. For both (a) and (b) $R_F = 100\ R_{BN}$ and $R_{sf} = 3\ R_{BN}$. Reproduced from [46].

This expression is valid for the situation where the resistance of the ferromagnetic wire dominates the resistance of the whole structure. The first two terms represent the resistance change due to changes in the boundary resistance. The last term is the difference in spin accumulation between normal and superconducting states. Only the quasiparticle conductance gives a contribution to spin accumulation since spins cannot be injected in the superconductor by the Andreev reflection process. The angle brackets represent thermal averaging.

Figure 6.5(a) shows the temperature dependence of the resistance change (normalized to $R_{\rm BN}$) for the case when the number of transmission channels is identical for the two spin species. The different curves are for different values of the parameter q, which refers to the relative mixture of tunnel and ballistic contact properties; this allows the authors to model all types of contacts. In this plot the solid curves are for a diffusive contact with relatively high transparency ($q = 0.75$), while the dashed curves are calculated for a less transparent interface ($q = 0.25$). The polarization of the wire is changed from $\gamma = 0$ (unpolarized case) to $\gamma = 0.6$ from bottom to top curves.

The effect of the superconducting transition is to increase the resistance for both types of contacts when the wire has a non-zero polarization. Since γ comes only into the spin accumulation term of the resistance change (equation 6.7), the enhanced resistance is due to spin accumulation. The effect is more pronounced for the transparent contact: the temperature dependence changes from monotonically decreasing in the unpolarized case to a reentrant behavior for larger spin accumulation, when the low-temperature resistance can become higher than the normal state resistance.

The curves for the highest polarization show that the resistance does not decrease at all; it increases right below T_c. The low-temperature resistance change is given by equation 6.7 in the limit $T \to 0$:

$$\Delta R_{\mathrm{FS}}(T=0) = \frac{1}{G_{\mathrm{A}}(0)} - R_{\mathrm{BN}} + \gamma^2 \frac{R_{\mathrm{sf}}}{1 + R_{\mathrm{BN}}/R_{\mathrm{sf}}} \ . \tag{6.8}$$

The third term has a maximum value of $\gamma^2 R_{\mathrm{sf}}$ for $R_{\mathrm{BN}} \ll R_{\mathrm{sf}}$.

Figure 6.5(b) shows the effect of the interface polarization $\gamma_{\mathrm{B}} \neq 0$ on the temperature dependence of the resistance for a relatively transparent contact ($q = 0.75$). Recalling the definition of γ_{B} (eq. 6.3) we see that $\gamma_{\mathrm{B}} = 0.5$ represents the case of more quasiparticle conductance for the spin-up species $G_\uparrow = 3G_\downarrow$ (symmetric case), while $\gamma_{\mathrm{B}} = -0.5$ is obtained for $3G_\uparrow = G_\downarrow$ (antisymmetric case). This implies that there would be a difference in the resistance changes of the structure when the magnetization of the ferromagnetic wire is switched from parallel to antiparallel. We will test for this behavior in our devices.

At low temperature the resistance change is:

$$\Delta R_{\mathrm{FS}}(T=0) = \frac{1}{G_{\mathrm{A}}(0)} - R_{\mathrm{BN}} + R_{\mathrm{sf}}(4\gamma\gamma_{\mathrm{B}} - \gamma_{\mathrm{B}}^2) \ . \tag{6.9}$$

The spin accumulation contribution depends on the relative value of the two polarizations, and can become negative if $4\gamma\gamma_{\mathrm{B}} < \gamma_{\mathrm{B}}^2$.

We now review the case of inelastic scattering with linear response ($V = 0$) for $\gamma_{\mathrm{B}} = 0$. For the case when the electron temperature equals the lattice temperature ($T_{\mathrm{el}} = T$), the resistance change as a function of temperature can be written as:

$$\Delta R_{\mathrm{FS}}(T) = \frac{1}{\langle G_{\mathrm{QP}}(\epsilon) + G_{\mathrm{A}}(\epsilon) \rangle} - R_{\mathrm{BN}} + \gamma^2 \left[\frac{1}{\langle G_{\mathrm{sf}} + G_{\mathrm{QP}}(\epsilon) \rangle} - \frac{1}{G_{\mathrm{sf}} + G_{\mathrm{BN}}} \right] \ . \tag{6.10}$$

This expression is very similar to equation 6.7 derived for elastic scattering. The difference is in the thermal averaging of the conductances: in the inelastic case, the conductance is first averaged, and then the result is inverted.

Figure 6.6(a) illustrates the temperature dependence of the resistance for inelastic scattering in the ferromagnetic wire. The modeled contact is metallic, and the interface resistance is small compared to the bulk resistance of the wire. For the specific parameters chosen in the plot, the resistance change resembles the reentrant behavior of S/N structures.

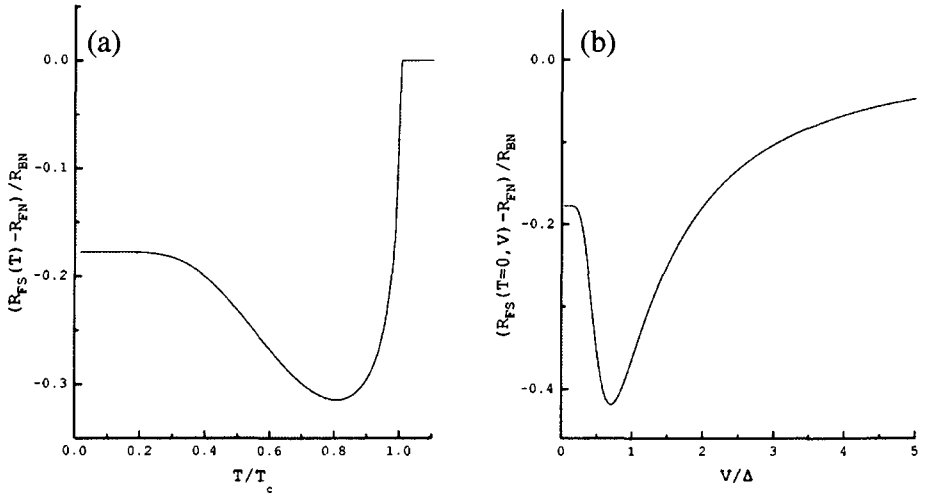

Figure 6.6 (a) Temperature dependence of the resistance change of the ferromagnetic wire in metallic contact with a superconducting reservoir in the case of inelastic scattering in the ferromagnet. (b) Resistance change as a function of bias voltage V. For both (a) and (b) the interface polarization is taken to be zero, and the wire polarization is $\gamma = 0.3$. Other parameters are $R_F = 20\ R_{BN}$ and $R_{sf} = 4\ R_{BN}$. Reproduced from [46].

Thermally-assisted spin current in the superconductor is not possible below temperatures satisfying the condition:

$$k_B T \lesssim \frac{\Delta}{\ln(R_{BN}/R_{sf})} . \tag{6.11}$$

From this condition and for the parameters of Figure 6.6(a), the authors find that spin accumulation is strongly reduced at $T/T_c \sim 0.7$.

The third regime studied by Belzig et al. is that of inelastic scattering where heating effects have to be taken into account, i.e., a finite bias voltage is applied across the structure. Figure 6.6(b) shows the resistance change at $T = 0$ as a function of the bias voltage V for the case of weak electron-phonon interaction in the ferromagnetic wire. The parameters are the same as for Figure 6.6(a). The dip in resistance at $V = 0.7\Delta$ is described by the condition

$$eV \lesssim \frac{\Delta}{\ln(R_{BN}/R_{sf})} \tag{6.12}$$

representing the voltage below which the spin accumulation excess resistance is lowered. Below the dip the resistance dependence on V is due to a competition between the excess spin accumulation-caused resistance, and the reduced interface resistance due to Andreev reflection.

If the electron-phonon interaction is strong, the electron temperature is equal to the lattice temperature, and there is no regime for enhanced spin current in the superconductor due to thermal

activation. In this case the spin accumulation can be reduced only when the ferromagnet is at a higher potential than the value of the superconducting gap. This occurs for

$$eV = \Delta \left(1 + 2\frac{R_{\mathrm{F}}}{R_{\mathrm{BN}}} \right) \quad . \tag{6.13}$$

To summarize, the numerical calculations of Belzig et al. show that the magnitude of the resistance change below the superconducting temperature is of the order of the interface resistance R_{BN} or the spin relaxation resistance R_{sf}.

6.2 Experimental Results

We have fabricated and measured three devices in the geometry proposed by Mélin. The devices are created in two steps. First, we pattern the ferromagnetic features using electron beam lithography, followed by the deposition of 20 nm of cobalt by thermal evaporation. In a second step the superconducting electrodes and the measuring leads are defined, followed by argon ion-milling to remove oxide and residue from the ferromagnetic film. Last, 60 nm of aluminum are deposited, also by thermal evaporation, to overlap the ferromagnetic features in a small area. More details on the fabrication procedure of these devices are given in Chapter 4. The dimensions of the features in the three devices are listed in Table 4.2.

An SEM picture of one of our S–FF–S devices is shown in Figure 6.7. The device proposed by Mélin has tunnel F/S interfaces; we have fabricated our devices with metallic interfaces in order to be in the same regime as the other samples presented in this dissertation, the FSF spin valves and the loop devices. The ferromagnetic wires attached between the superconducting electrodes are made of cobalt, which is a strong ferromagnetic material; the theoretical model assumes the wires are of this type.

The aspect ratio of the ferromagnetic wires in our S–FF–S devices is not optimal for achieving single-domain magnetic structure. In each sample the two ferromagnetic wires have been designed of different widths in order to obtain different coercive fields; typical sizes are $w = 70 - 120$ nm. For length of cobalt wires on the order of $l \sim 170 - 200$ nm, we have an aspect ratio $l/w \sim 2.5$. However, junctions of this size are necessary in order to achieve small separation between the two superconducting electrodes and, at the same time, minimize the interface area between the two metals. An even smaller length is desirable for creating a transport path smaller than the electron phase coherence length, but the magnetic configuration of those wires would likely be multi-domain

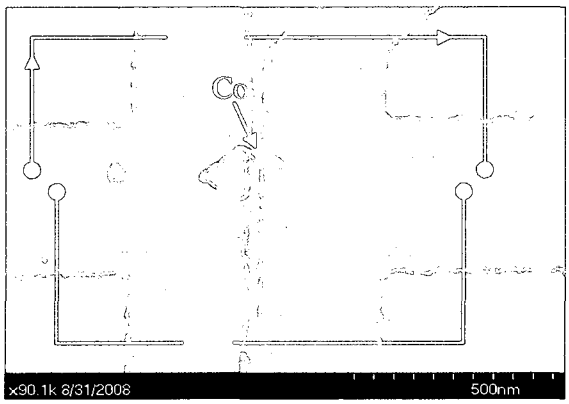

Figure 6.7 SEM picture of a double-junction S–FF–S device, with schematic of current injection and voltage detection measurement configuration.

due to lack of shape anisotropy. This would render it difficult, if not impossible, to identify the antiparallel magnetization state.

We measure electron transport properties in a dilution refrigerator with a base temperature of 8 mK. The measurement configuration is shown in Figure 6.7. First, we do magnetoresistance measurements in the normal state of the aluminum electrodes. Then, we set the magnetization state of the device in either parallel or antiparallel configuration, and cool the device down below the superconducting transition, recording the resistance change as temperature is lowered. Finally, at the lowest temperature of 8 mK, we measure IV characteristics and differential resistance curves. For some devices we also study the temperature dependence of the features in the differential resistance curves.

6.2.1 Magnetoresistance Curves

Magnetoresistance behavior in the normal state is measured by a resistance bridge with an excitation current of 30 μA. The magnetic field is swept by ramping current through a superconducting magnet immersed in the helium bath of the dilution refrigerator. Figure 6.8 shows typical magnetoresistance curves as a function of an applied field along the axis of the ferromagnets.

The ferromagnetic wires are first saturated in the parallel magnetization configuration by applying a large negative field of several hundred mT. As the field is swept from negative to positive, a change in the resistance of the wire with lower coercive field is observed at positive field values. Its magnetization reverses at this point to align with the new field direction, and the device switches to the antiparallel magnetization state, with a lower resistance value than the parallel state. As the

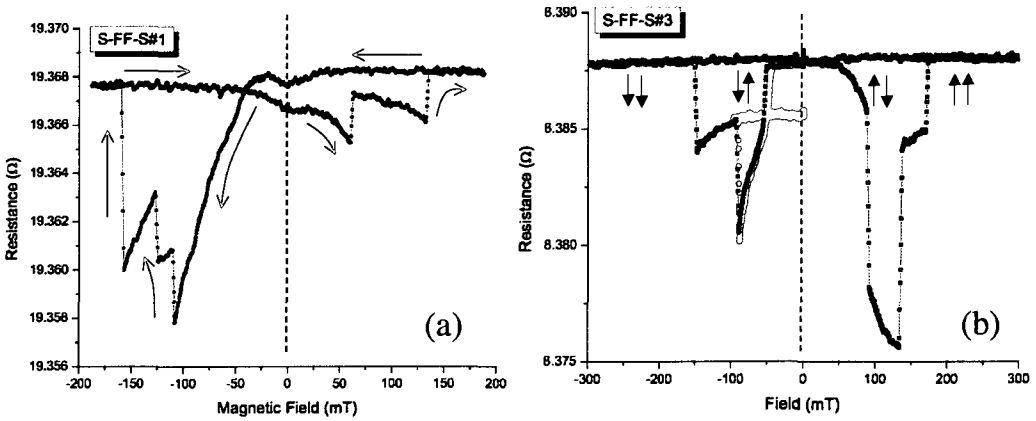

Figure 6.8 Magnetoresistance curves (a) Device S–FF–S#1 forms a domain in the wider probe at the negative coercive field. Red arrows indicate the direction in which the magnetic field increases and decreases. (b) Device S–FF–S#3 forms a domain in the wider probe at the positive coercive field. The green trace shows the magnetic field ramp up to when the antiparallel magnetization state is achieved, and the ramp back to zero that proves the magnetization state is stable. The arrows label the four magnetization configurations of the two wires.

field is increased further, the magnetization of the narrow wire flips, and the device is again in a parallel configuration. For example, for the device in Figure 6.8(a), the antiparallel configuration is found between 60 mT and 130 mT.

We observe domain formation in the wider wire of both samples. This wire has even less shape anisotropy than the narrower one, so it is more likely to develop domains of magnetization oriented away from the wire's easy axis. We believe the domain structure occurs in the bulk of the wire in between the two normal metal electrodes and not at the interface, where the narrow-shaped tip of the wire would constrain the magnetization to point perpendicular to the interface.

One important feature to be kept in mind is that in sample S–FF–S#1, the parallel alignment of the magnetization has different resistance values at positive and negative saturation field. This difference is maintained as the device is cooled down below T_c.

The two devices presented above have a relatively well-behaved magnetic response, despite the poor shape anisotropy. We are able to set the magnetization alignment with confidence to the desired state. This is not true for the third device measured, which has a magnetic behavior that is difficult to interpret. Figure 6.9(a) displays a magnetoresistance curve rich in small resistance switches indicative of the presence of domains in both wires. In addition to this we observe a strong AMR-like effect that is probably due to a slowly rotating magnetization. The explanation for this could be the domain structure in which the wire nucleates; these domains align very gradually with the applied field. Villa et al. [71] show that TEM studies on 60 nm long single cobalt wires reveal

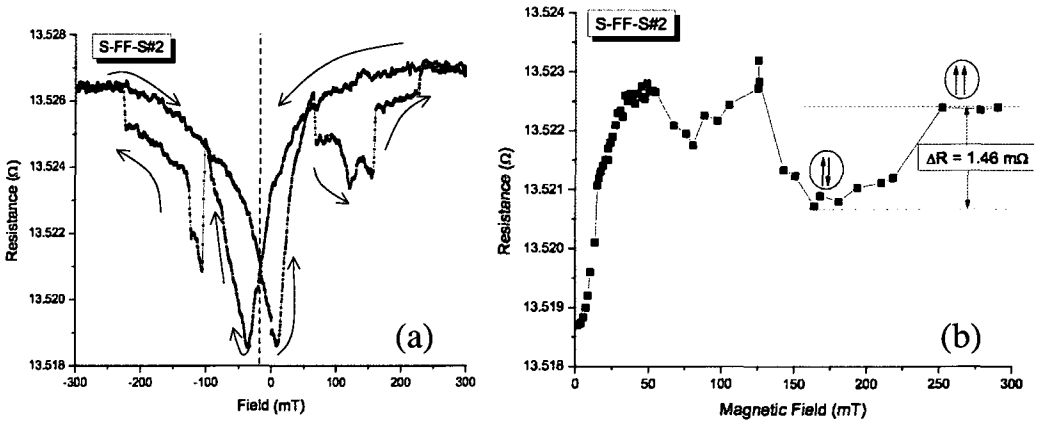

Figure 6.9 Device S–FF–S#2: (a) Magnetoresistance curve. (b) Probe fields method for identifying the antiparallel magnetization state.

a variation of the c-axis orientation along the wire axis. Diffraction patterns show that grains exist with c-axis parallel, perpendicular, or at an angle to the wire axis. Therefore, small cobalt wires might not have a well-defined magneto-crystalline anisotropy.

It is difficult to determine the antiparallel magnetization state using the magnetoresistance curve in Figure 6.9(a). We attempt to circumvent the parasitic effects present in that measurement by employing a "probe field" method, the result of which is illustrated in Figure 6.9(b). The method works as follows. We first saturate the two wires in the negative direction with a magnetic field of -500 mT. Afterwards, for each data point, we ramp the magnetic field in the positive direction to a certain magnitude, wait for a few seconds at that probe field value, then ramp back to zero and record the resistance. The probe field value is increased by 2 mT each time, until the 300 mT saturation value is reached. This way we identify the antiparallel magnetization alignment as the state with lower resistance. However, at small bias fields, the expected flat signal is still missing, and the resistance gradually increases as the field increases.

6.2.2 Single SF Junction: Temperature Dependence of Resistance and Differential Resistance

We include simple SF structures in the lateral geometry on the same chip as the S–FF–S devices. We do this for two reasons. First, in order to extract information about the material properties of the double-junction devices, we need to measure a structure with a single ferromagnet. The second reason is for enabling comparison with the transport behavior of the double-junction devices; this would hopefully help us differentiate between processes that happen in only one S-F contact and

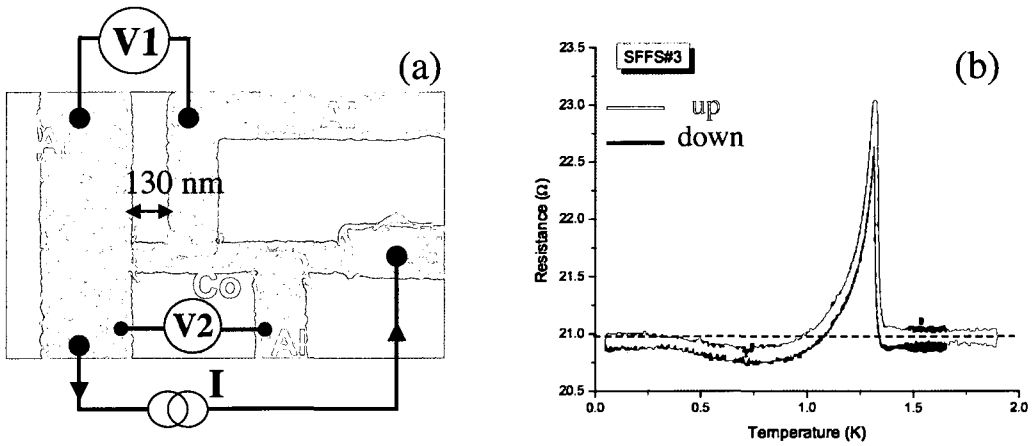

Figure 6.10 (a) Scanning electron microscope image of a single cobalt wire in contact with a superconducutor. The wire was fabricated on the same chip as device S–FF–S#3. The measurements in this section are done on the wire length across which voltage probes $V1$ are placed. (b) Temperature dependence of the resistance of the wire in panel (a). The behavior is measured for both parallel and antiparallel magnetization configuration of the wire (with respect to the applied field).

those that appear in a two-junction structure.

Figure 6.10(a) shows an SEM picture of the SF structure: a length of 130 nm of a ferromagnetic wire is placed between two superconducting voltage probes. Only the overlap with the superconductor to the left will be referred to as the SF "interface". The wire width is 117 nm, and it extends for 85 nm into the left superconducting wire (approximately 1/4 of the superconductor's width).

The resistance versus temperature curves for two different orientations of the magnetization in the wire are shown in Figure 6.10(b). The non-monotonic temperature dependence is reminiscent of the re-entrance effect observed in SN structures: as the temperature is lowered below the superconducting transition temperature $T_c = 1.36$ K, the resistance decreases, reaching a minimum value $R^* = 20.8\ \Omega$ at a temperature T^*, and then increases again to a value $R \approx R_N$ at $T = 10$ mK, where $R_N = 20.97\ \Omega$ is the normal state resistance.

This non-monotonic behavior has been observed in a few other experiments in lateral SF structures [42–44]. These authors have interpreted the results in terms of the proximity effect: pair correlations penetrate the ferromagnetic wires over length scales longer than predicted in strong ferromagnetic barriers. We will begin the analysis of our measurements by considering this possibility as the explanation for our results.

The first feature that we see right below T_c is a large peak in the resistance representing an increase of 10% over the normal state value. We attribute this peak to charge imbalance effects in the superconducting wire: the incident excitations, energetic enough to enter the superconductor

above the energy gap (which is very small close to T_c), disturb the balance of electron-like and hole-like excitations in the superconductor, creating a net charge imbalance that is detected as an increased voltage. As the temperature is lowered, the size of the energy gap increases and the charge imbalance voltage decreases; consequently, we see the resistance of the structure decrease.

In terms of the proximity effect, the high temperature resistance behavior can be explained as the expansion of superconductivity into the ferromagnet, which leads to a decrease in resistance. In the quasiclassical theory of the re-entrance effect, the resistance minimum occurs at a temperature T^* determined by the characteristic energy scale of the proximity effect, the Thouless energy E_{Th} of the metal: $T^* = 5E_{\mathrm{Th}}/k_{\mathrm{B}}$. From our temperature dependence data, $T^* = 0.75$ K, which gives a Thouless energy of 12.9 μeV. Using $D = 3$ cm^2/s for the cobalt wire and the expression for the Thouless energy $E_{\mathrm{Th}} = \hbar D/L^2$, we find $L = 124$ nm. This result represents the length over which the cobalt electrons reflected on the aluminum electrodes keep their phase coherence. This length is much larger than the exchange length $\xi_F = \sqrt{\hbar D/k_{\mathrm{B}}T_{\mathrm{Curie}}} = 1.3$ nm ($T_{\mathrm{Curie}} = 1388$ K for cobalt), so if there are coherence effects present in the ferromagnetic wire, they are not due to the usual proximity effect in superconductor-ferromagnet layered structures which decays on a length scale set by ξ_F. Since this value of L is close to the length of our wire estimated from the SEM image, it would be interesting to see if a device with a somewhat shorter ferromagnetic wire can carry supercurrent. However, we did not do this experiment.

Figure 6.11(a) shows the differential resistance as a function of the bias current measured at 10 mK. We observe a peak at zero bias, and a shallow minimum around 1.24 μA. At $I_{\mathrm{bias}} = 10$ μA the resistance switches to the normal state value via a sharp dip characteristic of the interfaces in all our devices (see the spin valve devices in Chapter 5). The voltage corresponding to this transition is 237 μeV.

The shape of the differential resistance resembles that of the temperature dependence curve. However, the features do not occur at the same resistance value. For example, the resistance minimum R^* is not the same: in the R vs. T curve, $R^* = 20.8$ Ω, while in the differential resistance curve, the minimum occurs at $R = 20.6$ Ω. However, these two need not be the same; if the proximity effect is responsible for the observed behavior, this minimum corresponds to the Thouless energy, and we need to do the following calculation. The length of 124 nm of the coherent part of the wire has a resistance of 8.64 Ω ($\rho = 16.3$ $\mu\Omega$·cm); the voltage drop across it at a current bias of 1.24 μA corresponding to the minimum in the differential resistance curve is 10.7 μV. This is very close to the value calculated for E_{Th}, supporting the interpretation in terms of the proximity effect.

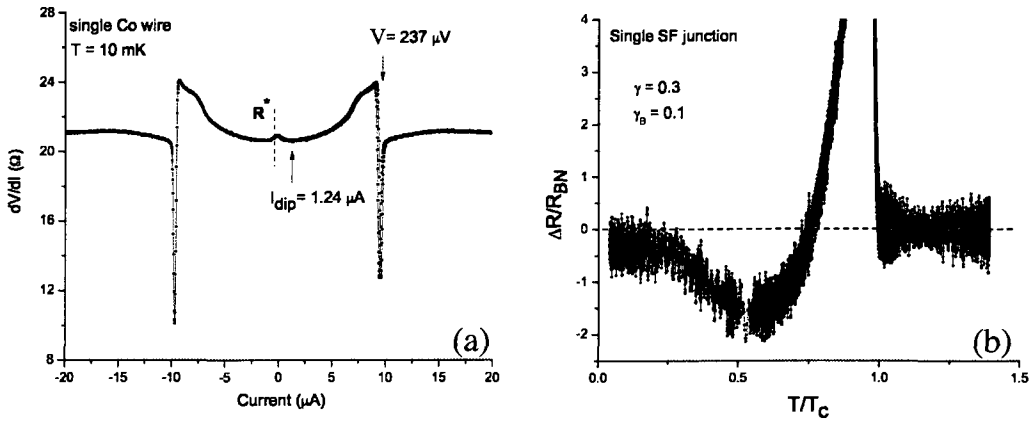

Figure 6.11 (a) Measured differential resistance curve of a single cobalt wire in contact with a superconductor. The intersection of the dashed line with the plot corresponds to the resistance value R^* at the dip in the temperature dependence curve. (b) Resistance change, normalized by the boundary resistance, as a function of temperature for the single cobalt wire structure in Figure 6.10(a).

There are two problems that prevent us from fully embracing the proximity effect picture. First, the resistance drop below T_c is about 15% in normal metal structures subjected to the proximity effect; the drop in our wire is 170 mΩ, which represents only a 0.8% decrease. However, this being a ferromagnet, it may be reasonable to accept a smaller difference. The biggest problem in applying this physical picture to our results is the exceedingly large decay length of pair correlations, which is 100 times longer than the exchange length in our cobalt wire. Such a long scale for the proximity effect has not been seen in SFS junctions with a weak ferromagnetic barrier, so it is difficult to understand why it might occur in our mesoscopic structure.

We find striking resemblance between our measured temperature dependence curves and the ones calculated by the theoretical model of Belzig et al. [46] reviewed at the beginning of this chapter. The charge imbalance peak does not appear in the theoretical curves, but the resistance dip and the flattening of the resistance are qualitatively similar. The behavior of a single F/S interface is calculated by taking into consideration only the interplay between spin accumulation close to the interface, and Andreev reflection at the interface. The proximity effect is not included in the model.

For the case of a diffusive contact the calculated resistance versus temperature curve shows the same re-entrant behavior: after an initial decrease below the critical temperature of the superconductor, the resistance increases again and reaches the normal state value at the lowest temperature (see Figure 6.5, 6.6). According to this model, the shape of the curve can be explained as follows: below the transition temperature the resistance drops as the temperature decreases due to the temperature dependence of the superconducting gap $\Delta(T) \propto \sqrt{T_c/T - 1}$, which affects the Andreev

reflection contribution to the interface conductance. Below a certain temperature given by equation 6.11, spin accumulation in the ferromagnetic wire leads to an enhancement of the resistance. The saturation regime is not explained.

In Figure 6.11(b) we plot again the single SF junction dependence on temperature but this time we monitor the resistance change, normalized by the boundary resistance. By comparing this curve to the curves numerically calculated by Belzig et al., shown in Figure 6.5, we estimate the polarization of our ferromagnetic wire to be $\gamma = 0.3$, and the boundary polarization $\gamma_B = 0.1$.

The magnitude of the resistance change between normal state and superconducting state is 0.44 Ω. Using the calculated value for boundary resistance $R_{BN} \sim 0.1\ \Omega$ of our junction and equation 6.9 at $T = 0$, we determine a spin-flip resistance $R_{sf} = 1.044\ \Omega$.

According to Belzig's model, the dip in the differential resistance curve in Figure 6.11(a) occurs at a voltage given by condition (6.12). Using our junction values for R_{BN} and R_{sf}, we obtain $V_{theoretical} \sim 0.42\ \Delta$. The experimental differential resistance shows a shallow dip with a minimum at $V_{exp} \sim 26\ \mu$V. For these two voltages to be the same, the value of the gap should be $\Delta = 62$ μeV. This is far off from aluminum gap values, usually in the 180 μeV range for bulk samples. An estimate of the gap energy in our sample using the temperature dependence expression

$$\Delta(T) \approx 1.76\ k_B T_c \tanh\left[1.74\sqrt{\frac{T}{T_c} - 1}\right] \tag{6.14}$$

gives 206 μeV at 10 mK. Therefore, the model does not give a good quantitative description for our devices.

To summarize our analysis of the single SF junction, we have two mechanisms that can explain the resistance behavior, both as a function of temperature and of an applied bias voltage. The proximity effect, even though it fits well quantitatively, seems to occur over a length scale much too large for a ferromagnetic barrier. The interface model of Belzig et al., on the other hand, gives unreasonable estimates of the gap energy. The double-junction devices S–FF–S presented in the next section may make it more clear what phenomena is responsible for this behavior.

6.2.3 S–FF–S Junctions: Temperature Dependence of Resistance

We prepare the device in either the parallel or antiparallel configuration, and in each case we cool down below the superconducting transition, monitoring the change in resistance as a function of temperature. Resistance is measured with a resistance bridge with an AC excitation of 100 nA at a frequency of 15.9 Hz. The temperature dependence of the resistance of all three devices is shown in

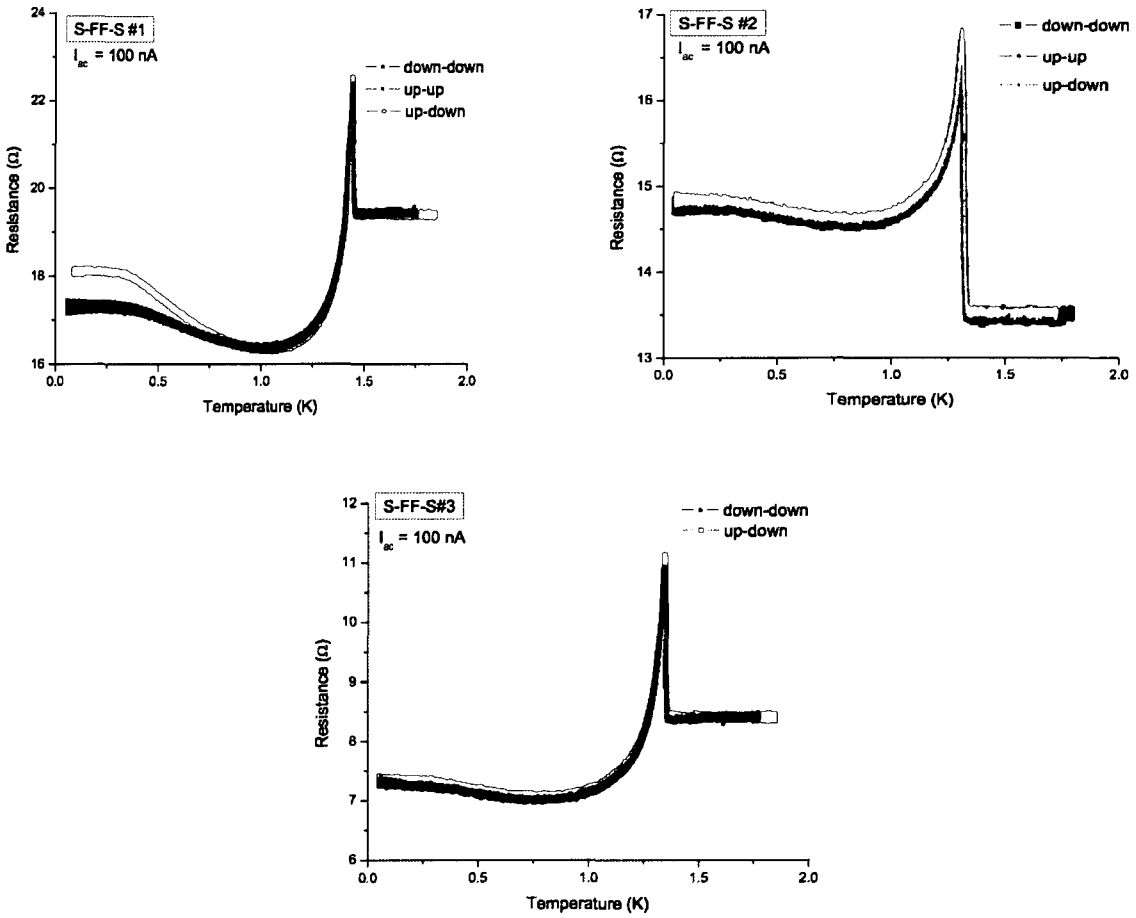

Figure 6.12 Temperature dependence of the resistance of our three S–FF–S devices.

Figure 6.12. The relevant parameters for the temperature dependence of these samples are listed in Table 6.1. Here we label the normal state resistances in the parallel and antiparallel magnetization alignment as R_N^P and R_N^{AP}, respectively. In the ratio $(R/R_N)^{AP}$, R represents the low-temperature value of resistance (i.e., the saturation resistance).

All samples show similar certain behaviors: an increase in resistance right below the transition temperature of the superconductor, followed by a decrease to a minimum value at approximately 0.65 T_c. Below this temperature the device resistance starts increasing again, showing a behavior reminiscent of the re-entrant effect in S/N structures. At 0.25 T_c the resistance saturates to a value close to the normal state resistance.

The most striking feature is the crossover between parallel and antiparallel magnetization states: above T_c, the resistance of the device in the antiparallel magnetization alignment is lower than in the parallel case; at the lowest temperature we find that the antiparallel state has a noticeably higher

Table 6.1. Relevant parameters in the shape of the resistance vs. temperature curves.

Sample	T_c (K)	R_N^{AP} (Ω)	$R_N^P - R_N^{AP}$ (mΩ)	$T_{\rm Dip}/T_c$	$T_{\rm Flat}/T_c$	$(R/R_N)^{AP}$
S-FF-S #1	1.46	19.40	2.50	0.70	0.23	0.930
S-FF-S #2	1.34	13.52	1.45	0.65	0.25	1.097
S-FF-S #3	1.36	8.41	2.40	0.60	0.22	0.870

resistance than the parallel state.

There are also some very important differences between the three devices. One is that the resistance of device S–FF–S#2 remains higher than the normal-state value after the drop below the peak at T_c, and saturates at $\sim 1.1\ R_N$ at low temperature. The numerical simulations of Belzig et al. [46] show that this can happen in dirty interfaces. Another difference in the temperature dependence is related to the crossover between the antiparallel and parallel states, which does not occur at the same value of T/T_c in all samples.

Resistance Peak

The resistance peak of S–FF–S devices is understood in terms of charge imbalance in the superconductor, as explained for the case of S–N interfaces in the introductory chapter (see section 3.1.1). However, in these devices we see that the peak height shows a dependence on the polarization of the two wires (see Figure 6.12): the height of the peak for the up-down magnetization configuration is greatest, followed by that for the up-up state, and last, the down-down state. The up-up and down-down states are not identical above T_c, and we see the difference between them in this temperature region as well. Charge imbalance alone cannot explain the observed behavior because this mechanism does not include a dependence on spin.

Figure 6.13 shows closeups of the peak region for two devices. Even though the resistance of one device is twice that of the other, the peak difference between P and AP states is the same, $\Delta R \sim$ 160 mΩ. This suggests that the mechanism that can discriminate between spin-up and spin-down electrons is related only to the superconducting gap, and that spin accumulation at the interface in the ferromagnetic wires does not play a role at this temperature.

The behavior we see must be due to spin imbalance, which can be understood in a similar way to charge imbalance (see section 3.1.1). However, in order to understand spin polarized injection of quasiparticles, we should consider all branches of the quasiparticle spectrum in the superconductor.

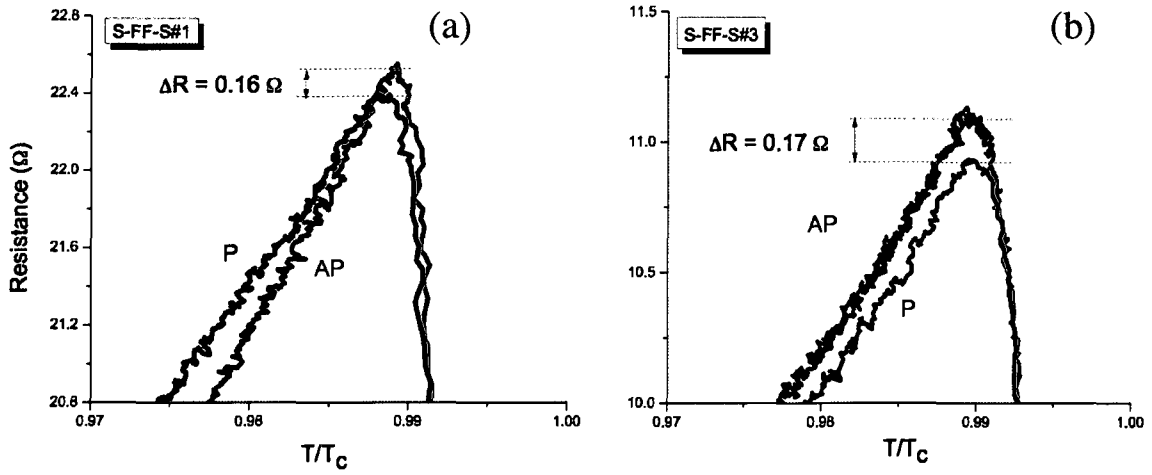

Figure 6.13 Peak resistance at $T \lesssim T_c$ for two S–FF–S samples. The height of the peak depends on the magnetization configuration of the device.

We illustrate in Figure 6.14(a) the four quasiparticle branches: electron- and hole-like branches for spin-up excitations, and electron- and hole-like branches for spin-down excitations. In the parallel magnetization alignment, both ferromagnetic wires inject spin-up polarized quasiparticles. As a result, the electron branch for spin-up excitations becomes overpopulated. A compensatory change in the number of electrons in the BCS ground state is required to maintain electrical neutrality, and this is accomplished by a shift in the chemical potential of pairs relative to that of quasiparticles. This shift is detected as a rise in voltage we measure at T_c. When the two ferromagnets inject opposite spin, both the spin-up and spin-down electron-like quasiparticle branches are imbalanced. We see that the shift in chemical potential between pairs and quasiparticles is higher than in the parallel case, but we do not have an explanation for it.

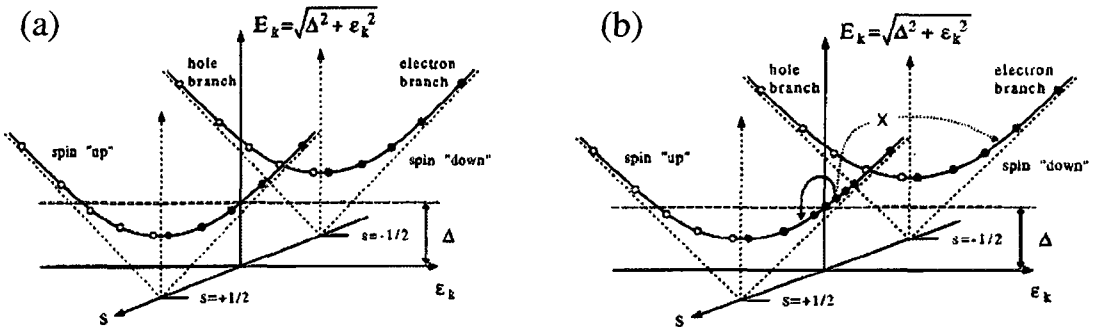

Figure 6.14 Quasiparticle branches in energy dispersion plots with separate branches for spin-up and spin-down quasiparticles. (a) Schematic occupation numbers in thermal equilibrium. (b) Schematic indication of population imbalance that might result from injection of spin-polarized carriers. Reproduced from [72].

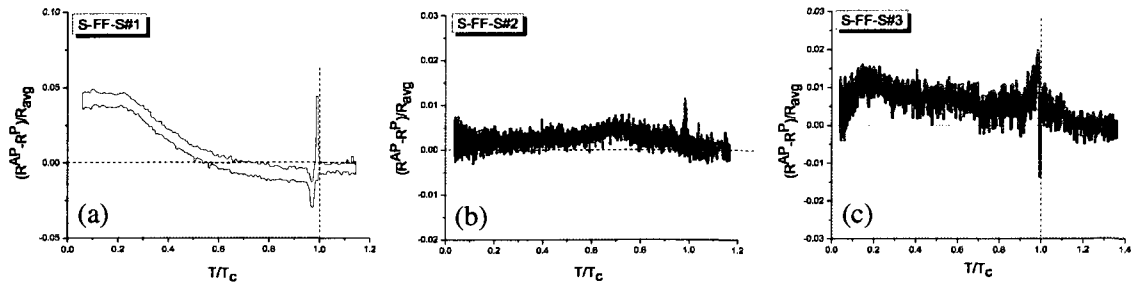

Figure 6.15 Difference between the antiparallel state resistance and the parallel one, normalized by the average value of the two states, for the three S–FF–S devices.

There is no other reported observation of the dependence of the resistance peak at the superconducting transition temperature on the spin polarization of the injected electrons. Nonlocal measurements in FSF spin valves (e.g., Beckmann et al. [3]) do not see a difference in the charge imbalance peak between the two magnetization alignments. Also, no theoretical model for a separate mechanism related to the magnetization of the non-equilibrium spin polarized quasiparticles is found in the literature.

Low Temperature Behavior

As the temperature is lowered below T_c, we observe a clear enhancement in the resistance of the antiparallel configuration for device S–FF–S#1, and a smaller, but still visible difference in the other two devices. This can be clearly seen if we plot the difference of the two states $R^{\mathrm{AP}} - R^{\mathrm{P}}$, normalized by their average $R_{\mathrm{avg}} = (R^{\mathrm{AP}} + R^{\mathrm{P}})/2$, as shown in in Figure 6.15.

The difference between the two states is not a monotonic function of temperature, and the behavior is not identical in the three devices. In device S–FF–S#1 the AP resistance increases as the temperature is lowered until the saturation point is reached at $T = 0.2\ T_c$. By contrast, in sample S–FF–S#2, shown in panel (b), we see a maximum in the difference at $T = 0.7\ T_c$, which corresponds to the dip in the R vs. T curve. From this point, as the temperature decreases, the resistance of the P state increases, but remains smaller than that of the AP state at the lowest temperature.

The difference $R^{\mathrm{AP}} - R^{\mathrm{P}}$ for the third device measured is shown in Figure 6.15(c). We see an increase below T_c similar to that of S–FF–S#1, but at the same temperature where S–FF–S#1 flattens out, the parallel state resistance of S–FF–S#3 starts to increase dramatically, reducing the difference to almost zero at the lowest temperature.

We are not certain why the three devices behave differently. All the fabrication steps are identi-

cal. Sample dimensions, summarized in table 4.2, are comparable, except for the larger separation between the superconducting electrodes in device #3. There is however one important difference between device #1, which shows the largest difference between P and AP configurations, and the other two devices: the cobalt purity was increased from 99.95% to 99.995%. This was done for the purpose of increasing the polarization of the material to check whether the low-temperature split between P and AP states might be increased in this fashion. We see the opposite, but we do not have a physical picture that correlates the reduced splitting to the polarization in the wires.

We compare our result to Luo et al. [70], discussed in Section 6.1. In their measurements, the parallel state has higher resistance than the antiparallel state at all temperatures. This can be understood as a result of spin accumulation: in the P configuration, both ferromagnets inject only spin-up quasiparticles, which results in a significant spin accumulation. In the AP state, one ellipsoid injects spin-up quasiparticles, the other spin-down; the spin population in the superconductor is therefore balanced, and the device resistance is lower than in the P state.

Since we see the opposite behavior, we must have a different low-temperature physical mechanism. We will present a possible explanation after we discuss the differential resistance measurements.

6.2.4 S–FF–S Junctions: Differential Resistance

We measured the differential resistance of two of our S–FF–S devices with an excitation current of 100 nA at a frequency of 15.9 Hz added to the DC bias. For device S–FF–S#1 the differential resistance curve was obtained by differentiating the IV characteristic. In the following we present the results on each device separately, and then we discuss possible explanations.

Figure 6.16(a) shows the differential resistance as a function of the bias current for the antiparallel magnetization state of device S–FF–S#2 at the lowest temperature, $T = 10$ mK. We observe a peak at zero bias, and a symmetric structure of peaks at higher bias currents. The zero-bias peak also appears in the differential resistance of a single ferromagnetic wire in contact with a superconductor, as shown earlier. In SN structures this peak is related to the reentrant effect. In SFS junctions it has been attributed to the inverse proximity effect, and has been shown to be greatly reduced in the parallel magnetization configuration [70]. As seen in Figure 6.16(b) and 6.17(b), the zero-bias peak in the differential resistance curves of our structures has not disappeared in the parallel state, so we cannot assign the inverse proximity effect to be the physical mechanism in our devices. The peaks in device S–FF–S#2 occur at $V = 303$, 233, 170, and 126 μV. We will discuss their nature in

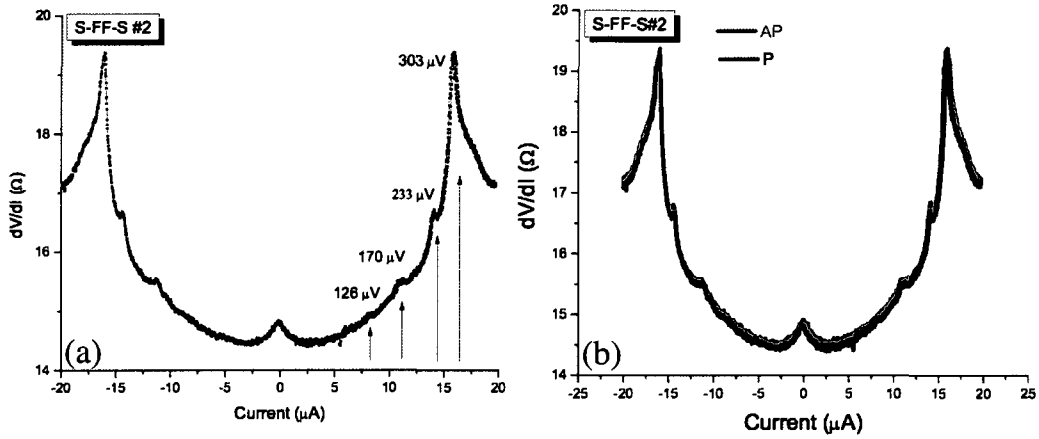

Figure 6.16 a) Measured differential resistance of device S–FF–S#2 in the antiparallel magnetization configuration. (b) Comparison of differential resistance curves of device S–FF–S#2 in the parallel and antiparallel magnetization alignments. Measurements presented are done at 10 mK.

detail after presenting related data from all samples.

The amplitude of all peaks is higher in the antiparallel alignment, except for the peak at transition to the normal state, where the parallel state has higher resistance. This agrees with the signal recorded in the resistance vs. temperature curves. Since the measurement setup for these curves is different than that for the differential resistance, the agreement in the data is reassuring: our results are not due to faulty measurements.

In Figure 6.17(a) we plot the differential resistance dV/dI versus bias current for the antiparallel magnetization state of sample S–FF–S#3. We observe shape and structure similar to those of sample S–FF–S#2. We note five peaks at voltages $V = 238$, 125, 94, 78, and 64 μV. The peaks with the smallest amplitude can be identified more clearly on the negative sweep of the curve.

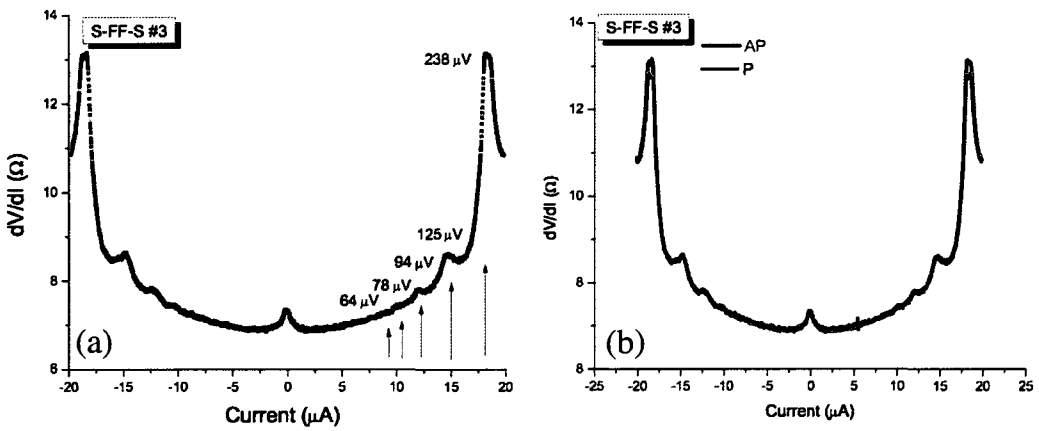

Figure 6.17 (a) Measured differential resistance of device S–FF–S#3 at 10 mK in the antiparallel magnetization configuration. (b) Comparison of differential resistance curves of device S–FF–S#3 in the parallel and antiparallel magnetization alignments.

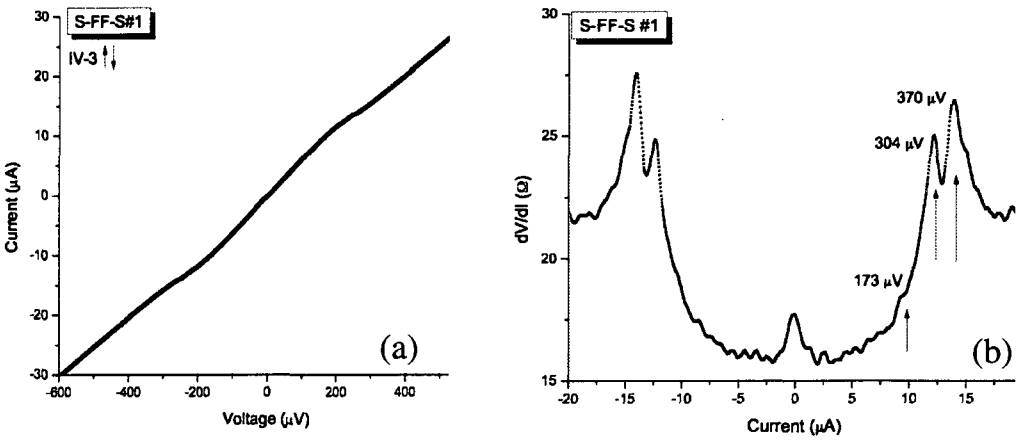

Figure 6.18 IV characteristic (a) and calculated differential resistance (b) of device S–FF–S#1 at 10 mK in the antiparallel magnetization configuration.

Figure 6.17(b) shows the comparison between parallel and antiparallel configurations. Again, the zero-bias peak is present in both states, and the relative magnetization orientation of the two ferromagnetic wires does not change the peak position at finite bias. In this device even the amplitude of the peaks is identical due to an unexplained downturn behavior of the AP-state resistance vs. temperature, as seen in Figure 6.15(c), that brings the resistance value of P and AP states close to each other.

We did not measure differential resistance for the sample that shows the largest difference between P and AP states. We numerically differentiate the IV characteristic (Figure 6.18(a)) to obtain the dV/dI curve shown in Figure 6.18(b). In this device we only see two clear peaks; it is possible that another feature at ~ 10 μA bias current is also a peak.

The measured dV/dI curves versus temperature for two devices are shown in Figure 6.19. The amplitude of the features has a relatively weak temperature dependence. Both the zero-bias peak and the finite-bias peak structure fade out with increasing temperature, but are still visible up to temperatures close to $T_c = 1.34$ K.

For device S–FF–S#2, the features start to change amplitude at a temperature between 300–460 mK. We note that 300 mK corresponds to the temperature below which the R vs. T curve flattens out. At 930 mK the zero-bias peak has not completely disappeared, and also three peaks are still visible. In the case of device S–FF–S#3, the amplitude of the zero-bias peak dropped by 2.2% at 530 mK, and became zero at 1 K, and only two of the five peaks are still clearly visible.

A variety of experiments have reported peaks of this type in the differential resistance. The

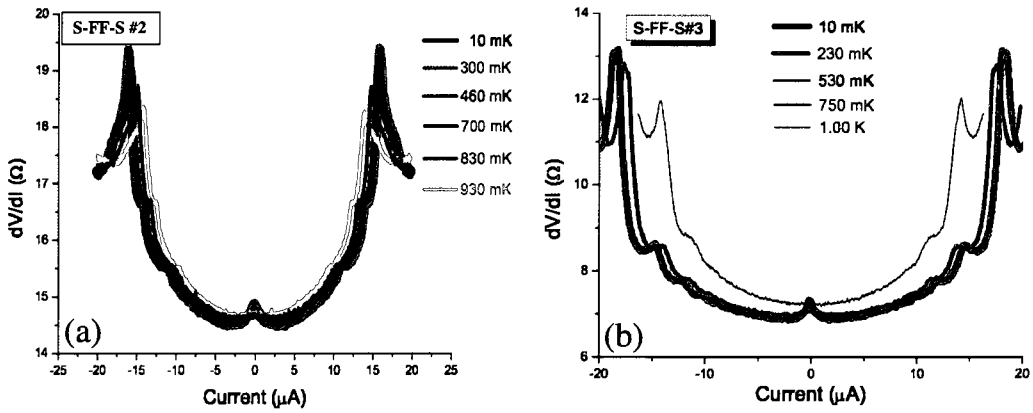

Figure 6.19 Temperature dependence of the differential resistance of device S–FF–S#2 (panel (a)) and S–FF–S#3 (panel (b)) in the antiparallel magnetization configuration.

Table 6.2. MAR peak positions for our three S–FF–S devices.

Sample	S–FF–S#1			S–FF–S#2				S–FF–S#3				
V_{peak}	393	315	170	303	233	170	126	238	125	94	78	64
n	1	1.25	2.3	1	1.3	1.8	2.4	1	1.9	2.5	3	3.7

phenomenon is referred to as the "subharmonic gap structure" (SGS), and is attributed to multiple Andreev reflections (MARs). After examining the behavior of these peaks in our devices as a function of temperature, we ascribe them to MARs. This is the first observation of the phenomenon in a ferromagnetic barrier. All previous studies that report SGS have been carried out in other systems: Dayem bridges [73], SIS tunnel junctions with different superconducting electrodes [74], superconductor/semiconductor/superconductor junctions [75], and SNS junctions [76].

If we assume that the position of the peaks follows the simple scaling relation $2\Delta/ne$, with $n = 1, 2, 3...$ being the number of reflection cycles, encountered in SNS junctions (see Chapter 3), then by dividing the highest peak, assumed to be the 2Δ peak, to the subsequent peaks, we should obtain integer values of n. Table 6.2 gives the peak positions in our devices, and the value of n determined as explained above. In addition to values of n close to 2, 3, 4, we have intermediate values $n = 1.3$, 2.4. We note that some values of the peak voltages appear in more than one device: for example, $V = 170$ μV is present both in S–FF–S#1 and S–FF–S#2, while $V \sim 233$ μV and $V \sim 125$ μV is present both in S–FF–S#2 and S–FF–S#3. A reasonable value for the gap of our aluminum electrodes would be $\Delta = 170$ μeV, but a peak at this voltage does not appear in all three devices.

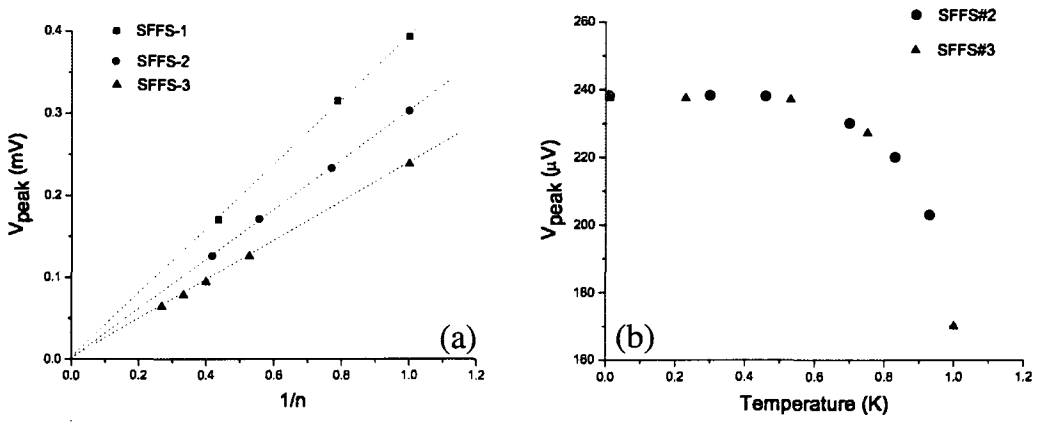

Figure 6.20 (a) Voltage of the conductance peaks versus $1/n$. (b) Temperature dependence of the 2Δ conductance peak for two samples with different resistances.

Figure 6.20(a) shows the scaling of the peaks with $1/n$, with n value taken from Table 6.2. We note that even though the three samples have very different resistances, the voltages at which the peaks occur are not too different, indicating that the presence of the peaks is related to the superconducting gap. Also supporting this claim is the fact that the curve of the $n = 2$ peak versus temperature has the shape of the BCS gap temperature dependence, as can be seen in Figure 6.20(b).

We search for a better peak scaling relation than the $2\Delta/n$ by looking at MARs results in the literature in various other devices, either measured experimentally or only analyzed theoretically, that have something in common with our junctions. We then tried to fit the peak positions we observe to the SGS relation of these other devices.

First we look at SNS junctions in the limit in which the Thouless energy is smaller than the gap energy of the electrodes $E_{\mathrm{Th}} \lesssim \Delta$; a theory of coherent MAR structure [36] predicts that the proximity effect gives rise to additional peaks in the differential conductance at $eV \approx 2(\Delta \pm E_{\mathrm{Th}})/2n$, in addition to the conventional SGS structure $eV = 2\Delta/n$. We estimate $E_{\mathrm{Th}} = 14$ μeV in our devices, so the peaks measured in our samples do not fit this predicted series.

The effect of spin polarization on SGS was taken into account by Martín-Rodero et al. [77]. They have analyzed subgap transport through SFS constrictions, and predict that the peaks should occur at $eV = \Delta/\sqrt{2}n$. Our peak positions do not match this structure either, which is to be expected since the theoretical calculation was done in the limit of transmission through the barrier of only one spin species.

It is clear that a simple answer is difficult to find: the peaks are the result of multiple Andreev reflections in each junction, characterized by somewhat different transmissions through the interfaces

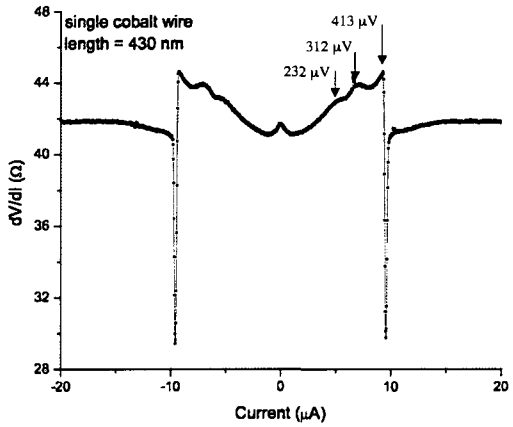

Figure 6.21 Differential resistance measurement across the single SF junction shown in Figure 6.10. The voltage drop measured (V_2 in Figure 6.10) is across 430 nm-long ferromagnetic wire.

due to the fabrication method. Also, electron diffusion is slightly different in the two wires due to surface scattering effects when the wire width is different. The unique geometry of our junctions, and their small size, make it difficult to find a relation between peaks without a detailed theoretical model; proximity effect and spin polarization effects in each of the two parallel junctions of a device combine to give a unique behavior that cannot be obtained by a simple deconvolution of these effects.

We see MAR features also in the single cobalt junction illustrated in Figure 6.10; the differential resistance of this structure is plotted in Figure 6.21. The large-bias peak positions $V_1 = 413$ μV and $V_2 = 312$ μV are similar to the ones found in S–FF–S#1, while the smallest one at $V = 232$ μV is characteristic of the other two devices. In this single junction, $2\Delta = 413$ μV, which gives a value for the gap of 206 μV, consistent with the one calculated from equation 6.14. The SGS structure shows again non-integer values of $n = 1.3$ for the ratio of the two largest peaks V_1/V_2.

We return to the SGS in the double SFS junctions to discuss more implications of the temperature dependence behavior. The SGS and the zero-bias peak show the same temperature dependence, which indicates that the phenomena giving rise to them are related. The amplitude of the MAR peaks depends weakly on temperature. This indicates that the features are not governed by the thermal length, characteristic of the Josephson coupling between the superconducting electrodes, because that would give an exponential dependence on temperature. Instead, we assert that the relevant length scale is the electron phase coherence length $L_\varphi(T)$ in the ferromagnetic barrier. Wei et al. ([78]) found the dephasing time in cobalt at 30 mK to be $\tau_\varphi \sim 1.3$ ps. This gives a value for $L_\varphi = \sqrt{D\tau_\varphi} = 20$ nm, using $D = 3$ cm^2/s in our cobalt wire. We find that the Andreev electron-hole pairs maintain coherence for a longer distance, since our wires are 1.5 (device #2) to 3.2 (device #3) times longer (excluding the overlap regions) than this calculated L_φ.

Since the position and amplitude of the SGS seen in our junctions do not depend on the rel-

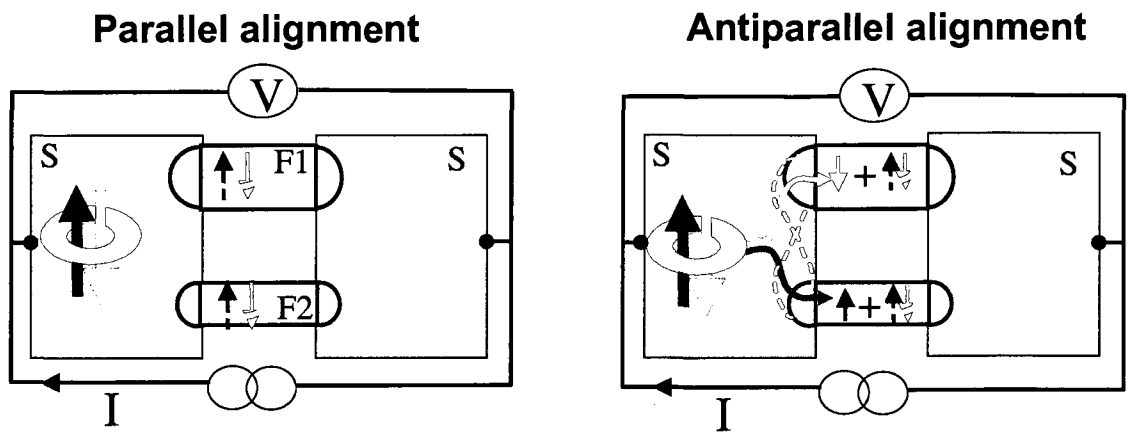

Figure 6.22 (a) Transport between the two SC electrodes for (a) Parallel magnetization alignment (b) Antiparallel magnetization alignment.

ative magnetization orientation of the two ferromagnetic junctions, we did not make considerable progress in understanding the mechanism behind the crossover between the parallel and antiparallel alignments. We put forward a possible explanation for the crossover based in part on the coherent transport of electrons in the SFS junctions evidenced by the presence of MARs, and in part on spin-polarization effects at the interface.

Possible Explanation

Subharmonic gap structure in SNS junctions occurs at bias currents exceeding the critical current. In this regime, both supercurrent and dissipative current flow in the normal metal. It is possible that the same physical picture holds true in our short ferromagnetic junctions: there might be supercurrent flow in the junctions, and we may not have enough resolution to observe it. The measured SGS structure indicates coherent transport, which means that Cooper pairs flow in parallel to the dissipative current. The coherent transport in the S–FF–S devices occurs over distances longer than the exchange length in the ferromagnet. This picture is supported by the analysis of the single SF junction in terms of re-entrant effect, which was in good quantitative agreement with an interpretation in terms of (long-range) proximity effect. We suggest the following mechanism to explain the difference in resistance between P and AP magnetization configurations of the devices; note, however, that this is a simplistic explanation of a phenomenon that should receive a detailed theoretical treatment.

Figure 6.22 gives a schematic description of the proposal. If current is injected from the left SC electrode into the right one, then:

(a) Cooper pairs diffuse into each lead, and travel across the junction as Cooper pairs, if the relative magnetization of the two ferromagnets is parallel. They undergo successive Andreev reflections at the each S/F interface before being absorbed into the right electrode.

(b) If the relative magnetization is antiparallel, then some of the Cooper pairs diffuse into each lead and undergo successive Andreev reflections at each S/F interface, just as in the parallel magnetization case, while some Cooper pairs split into and diffuse as spin-up and spin-down electrons, according to the magnetization orientation of the two junctions. These two electrons that result from a split Cooper pair travel separately through each ferromagnetic junction, increasing the dissipative current, and therefore increasing the resistance.

The splitting of the two electrons according to the magnetization orientation in the two wires is a realization of crossed Andreev reflection (CAR). Detailed theoretical modeling should aim to identify the conditions that make it favorable for the Cooper pairs to split so that further device engineering can enhance this outcome.

6.2.5 Saturation Regime

We observe the saturation of the resistance of our devices at low temperature. The question is whether this is a fundamental quantum mechanical effect, or an effect caused by heating.

The low AC excitation current and low wire resistance of our devices give an estimated 0.1 pW dissipated power in the saturation regime (below 250 mK). These samples are immersed directly into the mixture of ^{3}He and ^{4}He of a dilution refrigerator, which has over 250 μW of cooling power at 100 mK. Therefore, we believe that heating is not causing the measured saturation in resistance.

Mohanty et al. [79] measured the phase coherence time τ_ϕ in clean one-dimensional gold wires, and observed that the phase coherence time saturates at a finite temperature. They show that this behavior is not due to heating or magnetic impurities, as frequently suggested, and attribute the saturation to the limitation of L_φ when the temperature is lowered enough.

Other authors have different explanations for the observed saturation: defect dynamics in the conductors, spin flip scattering, scattering of the electrons contributing to the transport by the zero-point fluctuations of the electromagnetic environment, phase-destructive phonon-emission processes that remain important even at zero temperature, etc.

In our devices the saturation of dephasing occurs on the Thouless energy scale. Due to the uncertainty in the effective length of the junctions we cannot make a precise calculation; however, we can try to estimate it: if the saturation temperature of 250 mK corresponds to the Thouless

temperature $E_{\mathrm{Th}}/k_{\mathrm{B}}$, the junction length should be approximately 90 nm. This value is double the distance between the superconducting electrodes, but smaller than the total length of the junctions when the overlap area is included. Therefore, it is possible for the Thouless energy to set the dephasing length in these devices.

6.3 Summary

In conclusion, we do not observe the Josephson supercurrent predicted for the antiparallel magnetization alignment in our S–FF–S devices. Instead, we observe two effects that have not been reported before. First, we observe a crossover between the resistance of the parallel configuration and that of the antiparallel one as the temperature is lowered below the superconducting transition temperature. Therefore, at the lowest temperature, the resistance in the antiparallel state is higher than that of the parallel state. This is in contrast to previous measurements in SF structures, and contradicts theoretical predictions. Second, we observe a series of peaks in the differential resistance that we associate with multiple Andreev reflections; this result has never been reported in junctions with ferromagnetic barriers.

Chapter 7

Future Work and Summary of Results

7.1 Future Work

In this section we suggest future studies of crossed Andreev reflection aimed at finding signatures of coherence of this process. In addition to suggesting ways to extend the investigation of the double-junction devices, we propose to study a new device geometry, similar to a DC SQUID, and present preliminary results.

7.1.1 Mesoscopic SFS Junctions

Further experimental efforts are necessary in order to draw a conclusion about the observed effects in the double-junction devices. The S–FF–S structures have shown very interesting behavior, but the mechanism behind the effects observed is difficult to determine due to the parallel transport through the junctions. The next step would be to map out the effect of the separation between the two ferromagnetic wires; nonlocal correlations, if present, should decay on a length scale set by the coherence length. Also, another line of investigation could study the same devices, but fabricated with half-metal ferromagnets like CrO_2, or weak ferromagnets such as CuNi or PdNi.

It is desirable to complement these studies with measurements of single, short SFS junctions in the lateral geometry; such measurements could help shed light on some of the effects in the double junctions, especially on the multiple Andreev reflections that do not depend on the relative magnetization orientation in a double-junction device.

7.1.2 Coherence of EC and CAR Processes

Explaining the behavior of the devices presented in earlier chapters could be aided by studying nonlocal Andreev processes in a different design. We present here early experimental steps toward that goal, and discuss how this study can be extended.

Superconductor and Two Ferromagnetic Conductors in Loop Geometry

We have fabricated and measured SFS SQUID-type rings to explore signatures of coherence of the entangled electrons resulting from split Cooper pairs. The design of one such ring is schematically illustrated in Figure 7.1(a); a scanning electron microscope image of one measured device is shown in panel (b). The device consists of two short nickel wires of different width (170 nm and 110 nm) overlapping a 330 nm wide aluminum bar at one end; the overlap area is small, approximately 80 nm. The arms of a large aluminum loop (2 μm $\times$ 20 μm) attach to the wires at a distance 150 nm from the interface. The distance between the tips of the two ferromagnets where they touch the aluminum bar is approximately 70 nm. The large loop design allows us to apply a magnetic field perpendicular to the loop to modulate the phase difference across the two junctions. Details of the fabrication process are given in chapter 4.

Current is injected through leads attached to the middle of the loop, and leaves the device through a lead placed on the aluminum bar at the position of the overlap with the nickel wires. The voltage is measured across the same path, as shown in Figure 7.1(a).

There are two possible results for our measurements. First, it is possible that Josephson current flows in the device below the superconducting transition temperature. This would be an indication of coherent transport through the ferromagnetic wires. Given that the classic proximity effect in ferromagnets has a very short range (a few nanometers), and our wires are much longer than this, we have to look for other mechanisms that allow supercurrent flow. If supercurrent does exist in the device, we can apply magnetic flux into the loop. The critical current is a periodic function of the magnetic flux though the loop, so it should show oscillations. If the Josephson current through the two ferromagnetic junctions is due to Cooper pair transport through each junction, then the oscillation period should be one flux quantum, $\Phi_0 = h/2e$, similar to the DC SQUIDs made of Josephson tunnel junctions. However, the current-phase relation might be different if Cooper pairs split between the two ferromagnetic wires, as might happen if crossed Andreev reflection takes place. In order to identify which mechanism is present, we can study these oscillations by searching for changes induced when varying the relative orientation of the magnetization in the same device or when the probe separation is changed in additional devices. To date, there is no theoretical model that predicts the modulation period of this SFS loops for the case when crossed Andreev reflection is the dominant subgap process.

The angled design of our ferromagnetic wires might prove important when interpreting supercurrent data. When the wires are fully magnetized, the device will have non-collinear magnetization.

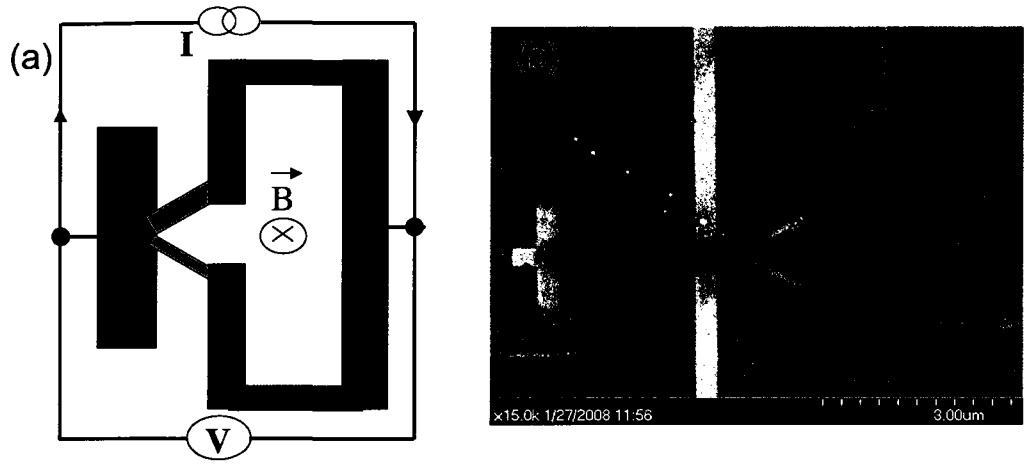

Figure 7.1 Design of ring samples fabricated to detect coherence signatures of EC and CAR processes. (a) Schematic drawing showing the measurement configuration (b) SEM image of one device.

There is a theoretical prediction by Fominov et al [45] for long-range proximity effects in FSF trilayers when the magnetization orientations of the two ferromagnets are non-collinear. In this situation the triplet superconducting component is generated. Even though our structure is not a multilayer, the physical effect should be the same. In this case the pair coherence is preserved up to distances given by $\xi_F^{\text{triplet}} = \sqrt{\hbar D_F / 2\pi k_B T}$. For nickel, using $D_F = 96$ cm^2/s, we estimate $\xi_F^{\text{triplet}} = 2.7$ μm at 10 mK.

The other possible result of our measurement is a finite resistance at the lowest temperature. In this situation, two other cases can be distinguished. In the first one, the electrons crossing the two junctions are correlated by the phase of the superconductor from which they originate. Upon applying a magnetic field to the loop, resistance oscillations may be observed due to interference of the two electrons' wavefunctions. However, if the length of the ferromagnetic junctions is longer than the length over which phase coherence is maintained, no oscillations will occur.

We start our investigation by examining the magnetic behavior of the device. Figure 7.2(a) shows the magnetoresistance behavior in a magnetic field applied parallel to the plane of the wires. The curve is not typical of magnetization switching in ferromagnets with uniform magnetization. We see a few switches to both a higher and a lower resistance state; no saturation is visible up to 100 mT. We conclude that there are many domains of magnetization present in these nickel wires. This poor ferromagnetic behavior makes our goal hard to accomplish: we can not set the magnetization alignment in parallel and antiparallel configurations.

We did however cool down the device through the transition temperature. The temperature

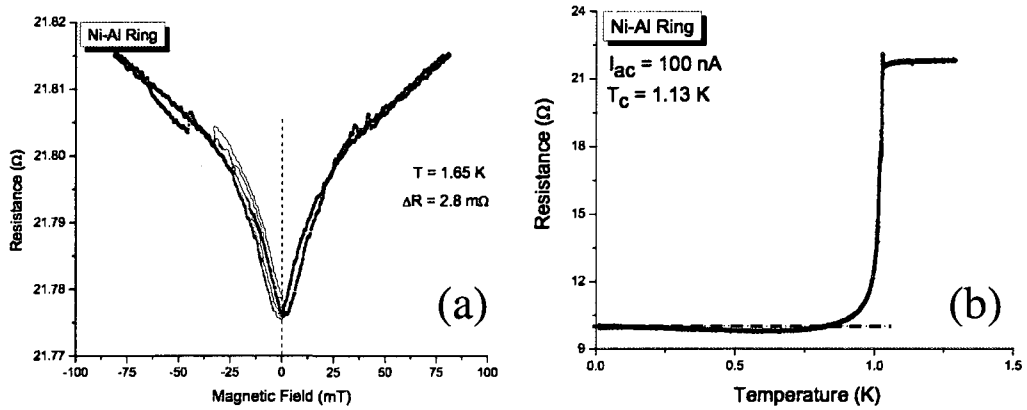

Figure 7.2 (a) Magnetoresistance behavior of the SFS ring in the normal state. (b) Resistance versus temperature dependence as the device is cooled below the transition temperature.

dependence of the resistance is shown in Figure 7.2(b). We observe a small charge imbalance peak right below T_c, followed by an abrupt drop in resistance associated with the aluminum loop becoming superconducting. The resistance goes through a shallow minimum and, as the temperature is lowered further, it slightly increases to reach saturation below 180 mK. Therefore, the resistance is not zero at the lowest temperature, when it is measured with a small AC excitation of 100 nA; however, the possibility of supercurrent flow still exists, if the critical current is smaller than 100 nA.

We characterize the device at 10 mK by measuring IV characteristics and differential resistance curves. We do not resolve a supercurrent in the low-bias regime. Figure 7.3(a) shows the differential resistance of the device measured with an AC current of 300 nA imposed on top of the DC bias current. We note a peak at zero bias that can be understood either in terms of the proximity effect, or as a spin accumulation signal, as shown by the detailed analysis of a similar feature in the devices presented in Chapter 6.

We choose five bias points on the differential resistance curve to investigate the behavior of the resistance when a magnetic field is applied perpendicular to the loop area. These points are indicated by vertical dashed lines in Figure 7.3(a), and the bias current values are 0.5 μA, 1 μA, 2.4 μA, 5 μA, and 7.5 μA.

Figure 7.3(b) shows the resistance versus magnetic field plots for approximately the bias points chosen in panel (a). A fixed DC current of magnitude indicated next to each curve is sent through the device, and the voltage drop is measured with a low-noise preamplifier. The resistance plotted is obtained by dividing the signal by the bias curent. The magnetic field is applied by a small superconducting coil through which we ramp 5 mA to obtain 2.5 Gauss. We calibrated the coil by recording critical current oscillations of an SNS device identical to this one, except for the junction

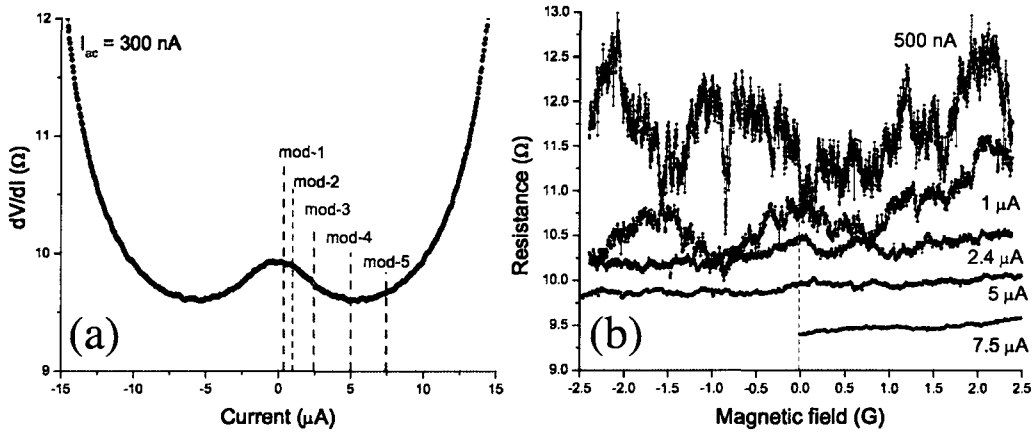

Figure 7.3 (a) Differential resistance curve of the Al-Ni-Al loop. The dashed vertical lines indicate bias current values for which we investigated the resistance oscillations. (b) Resistance oscillations of the SFS ring when a small magnetic flux is applied through the superconducting loop.

material. The number of flux quanta threading the loop at the maximum field applied by this coil is 4. We show measurements of these SNS devices in the next section.

The resistance oscillations we measure are not periodic. We do multiple traces for each value of the bias current, and observe no reproducibility in the measured signal. We conclude that the resistance of the two junctions does not depend on the phase difference across them, which implies that the electron transport through the ferromagnetic wires of this device is not coherent between the two superconductors.

This type of experiment should be investigated further. Coherent signatures of the entangled electrons are a better argument for proving that crossed Andreev reflection operates at the interfaces between superconductors and two ferromagnetic wires. Many improvements can be made. One starting point is to ensure we have single-domain ferromagnetic wires. It may be better to use cobalt instead of nickel, since our results in this dissertation show that cobalt has more suitable magnetic behavior. Another improvement can be made by reducing the length of the junctions to below the electron phase coherence length in nickel, estimated at 80 nm by Kasai et al. [80]. The phase coherence length in cobalt is smaller, approximately 20 nm, so from this point of view nickel is a better choice. Last, observing the phenomena we are looking for here requires large sensitivity in the experimental setup. In the DC measurement we employed, the noise was on the order of 500 mΩ for the lowest bias current, and 180 mΩ for 1 μA. The resolution can be improved significantly using a low-noise resistance bridge.

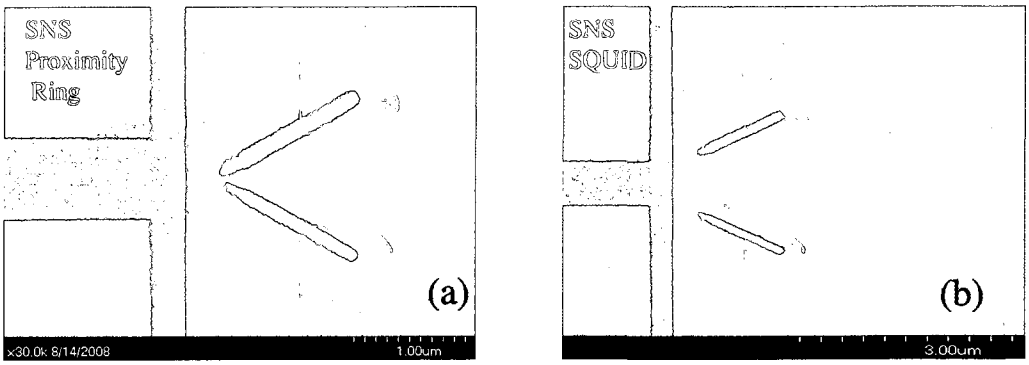

Figure 7.4 Scanning electron images of the superconductor-normal metal-superconductor loop devices (a) Proximity DC SQUID due to the small separation of the two normal metal wires. (b) Regular DC SQUID, where junctions are 1 μm apart.

Superconductor and Two Normal Metal Conductors in Loop Geometry

We have investigated transport properties of several SNS rings in the long junction limit. Scanning electron microscope images of the devices are shown in Figure 7.4. We study two different limits: the proximity limit in which the two normal metal wires are separated by a distance less than the superconducting coherence length (device in panel (a)), and the DC SQUID layout, in which the two junctions are far apart (approximately 1 μm in these devices; shown in panel (b)). In the "proximity SQUID" nonlocal Andreev processes are predicted to play a role and modify the current–phase relation of the Josephson junctions ([81]). The Andreev bound states depend on the coupling corresponding to the nonlocal propagation in the superconductors such that the supercurent is reduced compared to the regular SNS SQUIDs.

Critical current oscillations as a function of the applied flux through the loop are shown in Figure 7.5 for the two types of devices. We observe a non-sinusoidal modulation at low temperature in the proximity ring characterized by skewed oscillations. As the temperature is increased, the modulation of the two types of SQUIDs becomes similar. The value of the critical current is higher in the proximity device, which is contrary to the theoretical prediction. However, the device fabrication does not yield junctions of identical length, and even small variations in the overlap area with the two superconductors can contribute to measurably different critical currents.

We conclude that this approach is not optimal for the investigation of nonlocal effects in SNS structures. A measurement of the current-phase relation is desirable using the phase-sensitive SQUID interferometer techinique developed by Frolov and Van Harlingen [82].

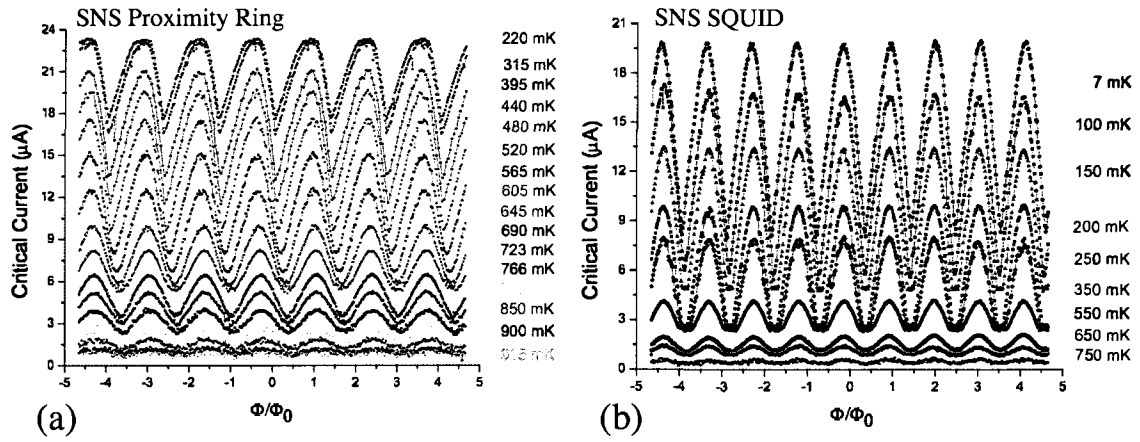

Figure 7.5 Modulation of the switching current by a magnetic field, as a function of temperature. (a) Skewed oscillations in the proximity SQUID at low temperature, and regular sinusoidal oscillations at high temperatures. (b) Sinusoidal oscillations in the regular SQUID at all temperatures.

7.2 Summary of Results

The work presented in this dissertation investigated signatures of nonlocal transport in the superconducting state in two types of devices. The first one, presented in Chapter 5, is a ferromagnet–superconductor–ferromagnet spin-valve geometry. We measure a negative nonlocal voltage in the antiparallel alignment of the magnetization of the two ferromagnetic probes, which is consistent with transport realized via crossed Andreev reflections. However, we cannot claim definite evidence for this because we did not perform similar measurements in the parallel magnetization configuration.

The second type of device, a superconductor–double ferromagnet–superconductor junction, was designed for exploring signatures of coherent transport of the electrons resulting in crossed Andreev reflection. We do not resolve supercurrent through the ferromagnetic junctions, but we see many interesting effects: re-entrant behavior of the resistance as the devices are cooled below the superconducting transition temperature; crossover between the resistance of the antiparallel magnetization alignment and that of the parallel configuration, with the AP state higher than the P state at low temperature; saturation of the resistance at low temperatures related to saturation of dephasing; and multiple Andreev reflection peaks indicative of coherent transport through the short ferromagnetic junctions. The mechanism creating these effects is not understood, and require further experimental investigation.

References

[1] J. M. Byers and M. E. Flatté, Phys. Rev. Lett. **74**, 306 (1995).

[2] P. Recher, E. V. Sukhorukov, and D. Loss, Phys. Rev. B **63**, 165314 (2001).

[3] D. Beckmann, H. B. Weber, and H. v. Löhneysen, Phys. Rev. Lett. **93**, 197003 (2004).

[4] P. Cadden-Zimansky and V. Chandrasekhar, Phys. Rev. Lett. **97**, 237003 (2006).

[5] A. Kleine, A. Baumgartner, J. Trbovic, and C. Schönenberger, cond-mat/0812.3553 (2008).

[6] S. Russo, M. Kroug, T. M. Klapwijk, and A. F. Morpurgo, Phys. Rev. Lett. **95**, 027002 (2005).

[7] R. Mélin, Phys. Rev. B **72**, 134508 (2005).

[8] J. Bardeen, L. N. Cooper, and J. R. Schrieffer, Phys. Rev. **108**, 1175 (1957).

[9] M. Tinkham, Festkörperprobleme 19, Advances in Solid State Physics **19**, 363 (1979).

[10] T. Crane, Ph.D. Thesis, University of Illinois (2005).

[11] N. F. Mott, Proc. Roy. Soc. A **153**, 699 (1936).

[12] M. Johnson and R. H. Silsbee, Phys. Rev. B **37**, 5312 (1988).

[13] A. G. Aronov, JETP Letters **24**, 37 (1976).

[14] M. Johnson and R. H. Silsbee, Phys. Rev. Lett. **55**, 1790 (1985).

[15] M. Johnson and R. H. Silsbee, Phys. Rev. B **35**, 4959 (1987).

[16] R. J. Elliott, Phys. Rev. **96**, 266 (1954).

[17] Y. Yafet, Solid State Physics **14**, 2 (1963).

[18] R. H. Silsbee, Bull. Magn. Reson. **2**, 284 (1980).

[19] F. J. Jedema, H. B. Heersche, A. T. Filip, J. J. A. Baselmans, and B. J. van Wees, Nature **416**, 713 (2002).

[20] J.-E. Wegrowe, S. E. Gilbert, D. Kelly, B. Doudin, and J. P. Ansermet, IEEE Trans. Magn. **34**, 903 (1998).

[21] G. E. Blonder, M. Tinkham, and T. M. Klapwijk, Phys. Rev. B **25**, 4515 (1982).

[22] M. Tinkham and J. Clarke, Phys. Rev. Lett. **28**, 1366 (1972).

[23] A. B. Pippard, J. G. Shepherd, and D. A. Tindall, Proc. R. Soc. Lond. A **324**, 17 (1971).

[24] M. L. Yu and J. E. Mercereau, Phys. Rev. Lett. **28**, 1117 (1972).

[25] J. Clarke, Phys. Rev. Lett. **28**, 1363 (1972).

[26] T. Y. Hsiang and J. Clarke, Phys. Rev. B **21**, 945 (1980).

[27] A. F. Andreev, Sov. Phys. JETP **19**, 1228 (1964).

[28] C. W. J. Beenakker, cond-mat/9909293 (2000).

[29] H. Courtois, P. Charlat, P. Gandit, D. Mailly, and B. Pannetier, J. Low Temp. Phys. **116**, 187 (1999).

[30] A. A. Golubov, F. K. Wilhelm, and A. D. Zaikin, Phys. Rev. B **55**, 1123 (1997).

[31] I. O. Kulik, Zh. Eksp. Teor. Fiz. **57**, 1745 (1969).

[32] C. Ishii, Prog. Theor. Phys. **5**, 1525 (1972).

[33] J. Bardeen and J. L. Josephson, Phys. Rev. B **5**, 72 (1972).

[34] A. Zaikin and G. F. Zharkov, Sov. J. Low Temp. Phys. **7**, 184 (1981).

[35] V. S. Shumeiko, E. N. Bratus, and G. Wendin, Low Temp. Phys. **23**, 181 (1997).

[36] P. Samuelsson, G. Johansson, A. Ingerman, V. S. Shumeiko, and G. Wendin, Phys. Rev. B **65**, 180514 (2002).

[37] E. V. Bezuglyi, E. N. Bratus, V. S. Shumeiko, G. Wendin, and H. Takayanagi, Phys. Rev. B **62**, 14439 (2000).

[38] G. J. Strijkers, Y. Ji, F. Y. Yang, C. L. Chien, and J. M. Byers, Phys. Rev. B **63**, 104510 (2001).

[39] V. V. Ryazanov, V. A. Oboznov, A. Y. Rusanov, A. V. Veretennikov, A. A. Golubov, and J. Aarts, Phys. Rev. Lett. **86**, 2427 (2001).

[40] M. J. M. de Jong and C. W. J. Beenakker, Phys. Rev. Lett. **74**, 1657 (1995).

[41] F. J. Jedema, B. J. van Wees, B. H. Hoving, A. T. Filip, and T. M. Klapwijk, Phys. Rev. B **60**, 16549 (1999).

[42] M. Giroud, H. Courtois, K. Hasselbach, D. Mailly, and B. Pannetier, Phys. Rev. B **58**, R11872 (1998).

[43] M. D. Lawrence and N. Giordano, J. Phys. Cond. Matt. **8**, L563 (1996).

[44] V. T. Petrashov, I. A. Sosnin, I. Cox, A. Parsons, and C. Troadec, Phys. Rev. Lett. **83**, 3281 (1999).

[45] Y. V. Fominov, A. A. Golubov, and M. Y. Kupriyanov, JETP Lett. **77**, 510 (2003).

[46] W. Belzig, A. Brataas, Y. V. Nazarov, and G. E. W. Bauer, Phys. Rev. B **62**, 9726 (2000).

[47] J. Aumentado and V. Chandrasekhar, Phys. Rev. B **64**, 054505 (2001).

[48] K. Halterman and O. T. Valls, Phys. Rev. B **69**, 014517 (2004).

[49] F. S. Bergeret, A. F. Volkov, and K. B. Efetov, Phys. Rev. B **69**, 174504 (2004).

[50] F. S. Bergeret, A. F. Volkov, and K. B. Efetov, Europhys. Lett. **66**, 111 (2004).

[51] F. S. Bergeret and N. García, Phys. Rev. B **70**, 052507 (2004).

[52] A. L. Yeyati, F. S. Bergeret, A. Martín-Rodero, and T. M. Klapwijk, Nature Physics **3**, 455 (2007).

[53] G. Falci, D. Feinberg, and F. W. J. Hekking, Europhys. Lett. **54**, 255 (2001).

[54] R. Mélin, Phys. Rev. B **73**, 174512 (2006).

[55] D. Feinberg, Eur. Phys. Jour. B **36**, 419 (2003).

[56] G. Deutscher and D. Feinberg, Appl. Phys. Lett. **76**, 487 (2000).

[57] I. O. Kulik and A. N. Omelyanchuk, Sov. J. Low Temp. Phys. **4**, 142 (1978).

[58] F. W. Smith, J. Low Temp. Phys. **6**, 435 (1972).

[59] M. J. Zuckermann, Phys. Rev. **140**, 899 (1965).

[60] G. Boato, G. Gallinaro, and C. Rizzuto, Phys. Rev. **148**, 353 (1966).

[61] R. Mélin and D. Feinberg, Phys. Rev. B **70**, 174509 (2004).

[62] R. Godfrey and M. Johnson, Phys. Rev. Lett. **96**, 136601 (2006).

[63] T. Kimura and Y. Otani, Phys. Rev. Lett. **99**, 196604 (2007).

[64] D. Beckmann and H. v. Löhneysen, Appl. Phys. A **89**, 603 (2007).

[65] M. J. Thornton and M. Ziese, eds., *Spin Electronics*, vol. 569 of *Lecture Notes in Physics* (2001).

[66] M. Johnson and R. H. Silsbee, Phys. Rev. B **76**, 153107 (2007).

[67] S. O. Valenzuela and M. Tinkham, Appl. Phys. Lett. **85**, 5914 (2004).

[68] D. S. Golubev and A. D. Zaikin, Phys. Rev. B **76**, 184510 (2007).

[69] R. Melin and S. Peysson, Phys. Rev. B **68**, 174515 (2003).

[70] P. S. Luo, T. Crozes, B. Gilles, S. Rajauria, B. Pannetier, and H. Courtois, Phys. Rev. B **79**, 140508 (2009).

[71] L. Vila, J. M. George, G. Faini, A. Popa, U. Ebels, K. Ounadjela, and L. Piraux, IEEE Trans. Magn. **38**, 2577 (2002).

[72] M. Johnson, J. Supercond. **14**, 273 (2001).

[73] P. E. Gregers-Hansen, E. Hendricks, M. T. Levinsen, and G. R. Pickett, Phys. Rev. Lett. **31**, 524 (1973).

[74] J. M. Rowell and W. L. Feldmann, Phys. Rev. **172**, 393 (1968).

[75] J. Kutchinsky, R. Taboryski, T. Clausen, C. B. Sørensen, A. Kristensen, P. E. Lindelof, J. Bindslev Hansen, C. Schelde Jacobsen, and J. L. Skov, Phys. Rev. Lett. **78**, 931 (1997).

[76] T. Hoss, C. Strunk, T. Nussbaumer, R. Huber, U. Staufer, and C. Schonenberger, Phys. Rev. B **62**, 4079 (2000).

[77] A. Martín-Rodero, A. Levy Yeyati, and J. C. Cuevas, Physica C Supercond. **352**, 67 (2001).

[78] Y. G. Wei, X. Y. Liu, L. Y. Zhang, and D. Davidović, Phys. Rev. Lett. **96**, 146803 (2006).

[79] P. Mohanty, E. M. Q. Jariwala, and R. A. Webb, Phys. Rev. Lett. **78**, 3366 (1997).

[80] S. Kasai, E. Saitoh, and H. Miyajima, J. Appl. Phys. **93**, 8427 (2003).

[81] S. Duhot and R. Mélin, Phys. Rev. B **77**, 014525 (2008).

[82] S. Frolov, Ph.D. Thesis, University of Illinois (2005).

Author's Biography

Madalina Colci O'Hara, born many, many years ago in a poor country, decided to study physics since it was just as likely to be profitable as engineering in the post-communist economy of Romania. Plus, she liked physics quite a lot, which helped toward receiving a B.S. from the University of Bucharest in 2000.

After working for a year at the Horia Hulubei National Institute of Physics and Nuclear Engineering, she heard that somewhere in the world it is possible to make a good living as a physicist, so she bought a plane ticket that landed her in Champaign-Urbana, in the "middle-of-nowhere" part of the United States. There, although she learned some more physics, she did not improve her knowledge of mathematics, so she started experimental research in her second year of graduate school. While at the University of Illinois she was given a Master's degree in 2003 for, basically, just being there, and the Renato Bobone Award in 2006 for the year's outstanding European graduate student, the latter making her quite happy.

While writing her dissertation Madalina found out that it is customary to write in the Author's Biography that one received the Ph.D. before the event actually transpires, so she here informs the reader that she received her Ph.D. in 2009.